Measured
Simulated

Strojniški vestnik – Journal of Mechanical Engineering (SV-JME)

Contents

Papers

Thermal Mechanical Coupling Analysis of a Flexible Spoke Non-pneumatic Tire

Hongxun Fu – Xuemeng Liang – Yan Wang – Laiyun Ku – Zhen Xiao

Shandong University of Technology, School of Transportation and Vehicle Engineering, China

A new type of non-pneumatic tire with a flexible spoke structure is proposed to solve traditional pneumatic tire defects, such as easy bursting, the requirement of real-time maintenance to keep tire pressure, and a complex manufacturing process. The thermal mechanical coupling characteristics of the flexible spoke non-pneumatic tire are studied in detail to obtain the steady-state temperature field distribution pattern under different operating conditions. A unit configuration method is proposed to build the 3D model of the flexible spoke non-pneumatic tire. Then, the thermal-mechanical sequential coupling method is used to analyse the deformation, energy loss and heat conduction of the flexible spoke non-pneumatic tire. Finally, the steady-state temperature field distribution pattern under thermal-mechanical coupling is obtained. The results show that the high temperature region of the non-pneumatic tire is mainly distributed in the middle bending part of the flexible spoke unit, and the temperature gradually decreases from the centre of the flexible spoke to the surrounding parts. The influence of load on the temperature change of non-pneumatic tire is greater than that of the driving speed. This study provides a theoretical basis and method guidance for solving the failure problem of the non-pneumatic tires under the action of thermal-mechanical coupling.

Keywords: non-pneumatic tire, flexible spoke structure, unit configuration method, thermal mechanical coupling, temperature field

Highlights
- *A unit configuration method for the structural design of the non-pneumatic tire is proposed.*
- *The thermal-mechanical sequential coupling method is used to analyse the deformation, energy loss, and heat conduction of the flexible spoke non-pneumatic tire.*
- *The temperature field distribution pattern of the flexible spoke non-pneumatic tire under the influence of thermal mechanical coupling is obtained.*
- *The influence of load on the temperature change of the non-pneumatic tire is greater than that of driving speed.*

0 INTRODUCTION

A non-pneumatic tire does not rely on air to adjust the tire elasticity and support the weight of the vehicle. It solves the problems of the traditional pneumatic tire, such as easy bursting, the requirement of real-time maintenance to keep tire pressure, and a complex manufacturing process. Therefore, non-pneumatic tire technology has gradually become a research topic of great interest in the field of tire safety, and new types of non-pneumatic tire structures have been put forward [1] to [3]. Compared with pneumatic tires, non-pneumatic tires have the advantages of anti-puncture, explosion-proof, shock absorption and good adhesion performance. However, they have poor performance in reliability and durability as they are easily affected by stress concentrations, alternating stresses, high temperatures and other factors [4] and [5]. The above problems seriously restrict the further development and application of non-pneumatic tire technology. Based on the study of the basic mechanical properties of a non-pneumatic tire, thermal analysis of a non-pneumatic tire has also been conducted. Currently, the performance of a non-pneumatic tire under the action of thermo-mechanical couplings has been

analysed. This has a high theoretical significance and an application value for the development of tire safety technology [6] to [8].

Researchers have conducted studies on the basic mechanical properties, fatigue, failure of non-pneumatic tires. Gasmi et al. [9] and Kucewicz et al. [10] conducted vertical static deflection simulations with the Tweel™ and honeycomb tires, analysing the influence of the vertical displacement of the hub, tread deformation and grounding pressure on the geometry of the flexible spoke structure. Xu et al. [11] studied the influence of the ratio of the mechanical elastic wheel (MEW) hinge group length to the elastic wheel thickness on the radial stiffness of the wheel based on the finite element analysis, realizing the multi-objective optimization of the radial stiffness of the MEW based on the artificial fish swarm algorithm. Mazur et al. [12], Ju et al. [13] and Jackowski et al. [14] obtained the rolling resistance of a non-pneumatic tire based on the prototype test method; they studied the influence of tire structure and the polyurethane (PU) material on the rolling resistance of a non-pneumatic tire, and compared pneumatic and non-pneumatic tires in terms of the rolling resistance. Fu et al. [15] and [16] conducted a preliminary study on the lateral deflection

properties of a mechanical elastic wheel and its influencing factors and established a theoretical model of the lateral loading of the wheel. Zang et al. [17] and Du et al. [18] studied the influences of load and roll angle on the distribution of the contact pressure of a MEW and made a comparison with the pneumatic tire. Sriwijaya and Hamzah [19] studied the influence of the road inclination angle on the stress distribution of the flexible spoke structure of a non-pneumatic tire; their results show that a larger road inclination angle increases the equivalent stress value of a honeycomb flexible spoke structure, thus accelerating the failure of the flexible spoke structure. Zhang et al. [20] carried out a static grounding performance analysis of a staggered non-pneumatic tire, obtaining the S-N curve of the flexible spoke PU material by using the demosia fatigue test, and entering it into the FE-SAFE software to predict the tire fatigue life. The above studies have preliminarily explored the structural performance and fatigue failure of a non-pneumatic tire, but the influence of temperature has not been considered in the research process.

During the rolling motion, the non-pneumatic tire deforms under the action of external loads, which causes a temperature rise of the tire, resulting in a possible decline of physical and chemical properties of the tire materials, a loss of strength, and eventually tire failure [21] and [22]. Many studies have been carried out to evaluate both the performance and the durability of pneumatic tires with temperature, but there are few studies on the influence of temperature of non-pneumatic tires. In particular, Chen et al. [23] and Zhu et al. [24] analysed the effects of vehicle speed, loss factor, and thermal conductivity of the material and wheel section width on the maximum temperature of a MEW. The authors proposed a theoretical analysis method to predict the surface temperature of a MEW under different driving conditions.

In this paper, the three dimensional (3D) model and numerical analysis model of a 195/50N16 flexible spoke non-pneumatic tire were established based on the unit configuration method. The thermo-mechanical sequential coupling method was used to investigate the thermo-mechanical coupling characteristics of the flexible spoke non-pneumatic tire under different operating conditions, which provides a method guidance for the subsequent fatigue failure research and structural optimization design of non-pneumatic tires.

1 ESTABLISHMENT OF THE NUMERICAL ANALYSIS MODEL OF A FLEXIBLE SPOKE NON-PNEUMATIC TIRE

1.1 Establishment of the 3D Model of the Flexible Spoke Non-pneumatic Tire using the Unit Configuration Method

Our research group proposed a unit configuration method for modelling the structural design of the non-pneumatic tire. It creates the non-pneumatic tire model of different structures by combining the unit structure with an arbitrary shape according to a different array mode and array number.

In this paper, the flexible spoke support body of the flexible spoke non-pneumatic tire consists of a circular array of 45 groups of flexible spoke units. Every group occupies a construction angle of 8°. Each flexible spoke unit consists of an inner ring, a circumferential spoke, a side spoke, and an outer

Fig. 1. *3D model of the flexible spoke non-pneumatic tire*

Fu, H. – Liang, X. – Wang, Y. – Ku, L. – Xiao, Z.
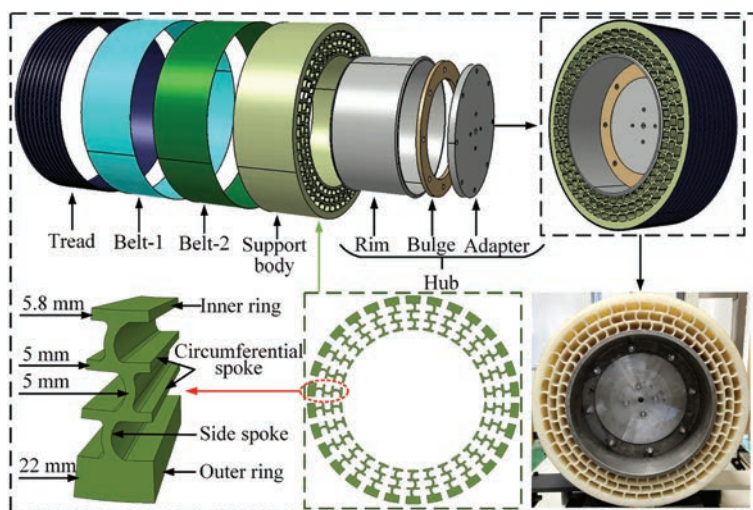
ring. The circumferential spokes of the flexible spokes are arranged in a layered structure along the radial direction of the tire, and the side spokes of the flexible spokes are combined as a wave line by "curved surface" treatment, with a curvature of 1/15. The flexible spoke non-pneumatic tire comprises a rigid hub, a flexible spoke support body made of PU material and a rubber tread. The flexible spoke support body connects the hub and the tread as a whole. In this case, the rigid hub is composed of the rim, the hub bulge and the hub adapter assembly, and the rubber tread contains two layers of wire belt. The flexible spoke non-pneumatic tire based on the unit configuration method is shown in Fig. 1, and the detailed structural parameters are shown in Table 1.

Table 1. *Detailed structural parameters of the tire*

Structure	Parameters
Tire model	195/50N16
Tread width [mm]	195
Outside diameter [mm]	602
Rim diameter [mm]	406.4
Spoke thickness [mm]	5
Curvature of spoke	1/15
Construction angle [°]	8
Number of unit groups	45

1.2 Construction of Numerical Analysis Model

The flexible spoke support body is the main structure of the flexible spoke non-pneumatic tire. The heat generation of the entire tire mainly comes from the flexible spoke support body. In the steady-state rolling process, the frictional heat generated by the contact between the tread and the ground is small and quickly carried away by the air, which has little influence on the overall temperature distribution of the flexible spoke non-pneumatic tire.

Therefore, the influence of the tread on the temperature distribution of the flexible spoke non-pneumatic tire can be ignored in the numerical analysis. To obtain the basic material properties of the PU material forming the flexible spoke support body, uniaxial tensile tests of the PU material were carried out by using an electronic universal testing machine to obtain the stress-strain relationship, as shown in Fig. 2.

For nonlinear materials, both the fitting accuracy and the stability are high by using Yeoh material constitutive model. The strain energy function of the hyper-elastic Yeoh model is as follows:

$$W = \sum_{i=1}^{3} C_{i0}(\bar{I}_1 - 3)^i$$
$$= C_{10}(\bar{I}_1 - 3) + C_{20}(\bar{I}_1 - 3)^2 + C_{30}(\bar{I}_1 - 3)^3, \quad (1)$$

where W is strain energy density; $\bar{I}_1$ is the first invariant of principal elongation ratio; C_{10}, C_{20}, C_{30} are material constants. In the first step of our study, the PU material is modelled as nonlinear elastic for simplification. Based on this approach, the mechanical loadings in the spokes of the non-pneumatic tire can be estimated.
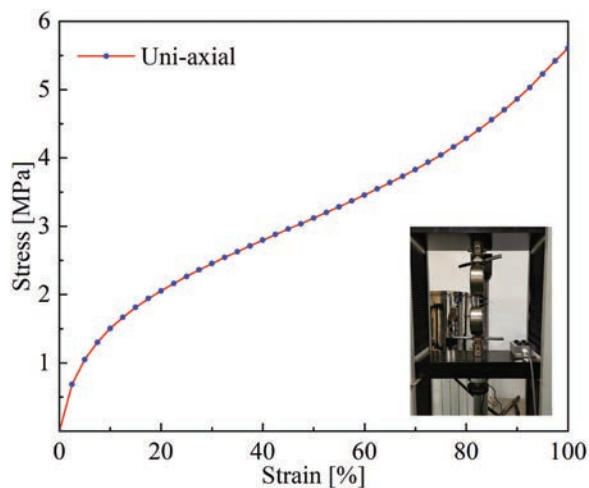
Fig. 2. *Stress-strain relationship of PU material*

The mesh of the flexible spoke non-pneumatic tire was divided. Since the hexahedral element has a higher accuracy in the calculations and is convenient for extracting the stress and the strain of the flexible spoke unit, the mesh of the flexible spoke unit consists of C3D8RH elements. The element number of a flexible spoke unit was 6,909, and that of the entire flexible spoke non-pneumatic tire was 193,050. The analysis steps and interaction settings of the flexible spoke non-pneumatic tire were carried out, and the friction coefficient was set to 0.5.

1.3 Verification of the Effectiveness of the Numerical Analysis Model

The static analysis of the flexible spoke non-pneumatic tire was carried out in ABAQUS, and the vertical load was evenly increased to the maximum level of 5000 N with intervals of 500 N. The loading test of the flexible spoke non-pneumatic tire under the same working condition was carried out based on the tire testing machine. After the completion of the test, the axial sinking under different vertical loads was

extracted, and the simulated and measured data were presented as vertical stiffness curves. The comparison of vertical stiffness curves of the flexible spoke non-pneumatic tire simulation and the test is shown in Fig. 3. RP represents the centre of the flexible spoke non-pneumatic tire.

It can be seen from Fig. 3 that the vertical stiffness of the flexible spoke non-pneumatic tire in the simulation and test tended to be consistent. After calculation, the relative error between the simulation and the test verification was only 4.7 %, which demonstrates the accuracy of the numerical analysis model.
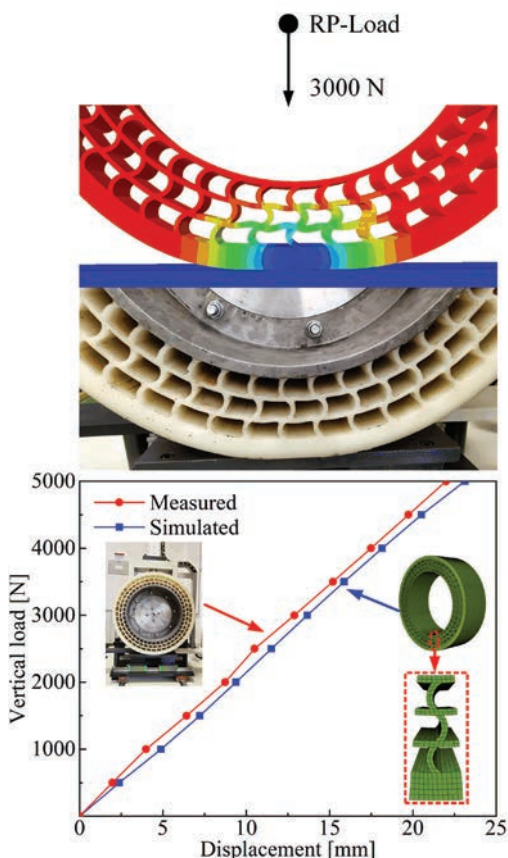
Fig. 3. *Comparison of vertical stiffness curves of simulation and test*

2 THERMAL-MECHANICAL COUPLING ANALYSIS OF THE FLEXIBLE SPOKE NON-PNEUMATIC TIRE

2.1 Thermal-mechanical Sequential Coupling Method

In this study, the thermo-mechanical sequential coupling method was used to analyse the mechanical fields of the flexible spoke non-pneumatic tire firstly,

and then the analysis results of mechanical fields were used as input conditions for the thermal field analysis. Finally, the thermo-mechanical coupling characteristics of the flexible spoke non-pneumatic tire were obtained. Fig. 4 shows the flow chart of the thermo-mechanical coupling analysis of the flexible spoke non-pneumatic tire, which mainly consists of deformation analysis, energy loss analysis and heat conduction analysis. In the deformation analysis, the static and dynamic mechanical characteristics were analysed using ABAQUS software. The accuracy of the numerical analysis model was verified in the static analysis. The stress and strain of each mesh element during the steady-state rolling process of a flexible spoke unit were extracted in the dynamic analysis. In the energy loss analysis, a Fourier transformation of the equivalent stress and equivalent strain was carried out using MATLAB software, and the lagging energy loss and heat generation rate were calculated. In the heat conduction analysis, a user subroutine was written to define the internal heat source, to endow the material with thermal properties and to set the thermal boundary conditions. Finally, the steady-state temperature field distribution pattern of the flexible spoke non-pneumatic tire under thermal-mechanical coupling was obtained.

2.2 Deformation Analysis

In the deformation analysis, the steady-state rolling of the flexible spoke non-pneumatic tire was carried out under a vertical load of 5000 N and driving speeds of 45 km/h, 65 km/h and 85 km/h, respectively. When the driving speed was 85 km/h, vertical loads of 3000 N, 4000 N, and 5000 N were applied to the non-pneumatic tire. The stress and strain of each mesh element in the flexible spoke unit under a rolling period (one cycle) were extracted. The data contained a total of 90 stress and strain data sets in one rolling period. Each set contains six components: S11 (LE11), S22 (LE22), S33 (LE33), S12 (LE12), S13 (LE13) and S23 (LE23). It was extracted once per mesh element at an interval of 4°. The stress and strain curves of a mesh element under a load of 5000 N and a driving speed of 85 km/h are shown in Fig. 5. This work provides a source of data for subsequent calculations of equivalent stress and equivalent strain.

2.3 Energy Loss Analysis

Fig. 6 shows the stress-strain phase diagram of the viscoelastic PU material. It can be seen that the stress and the strain of PU are not synchronized during
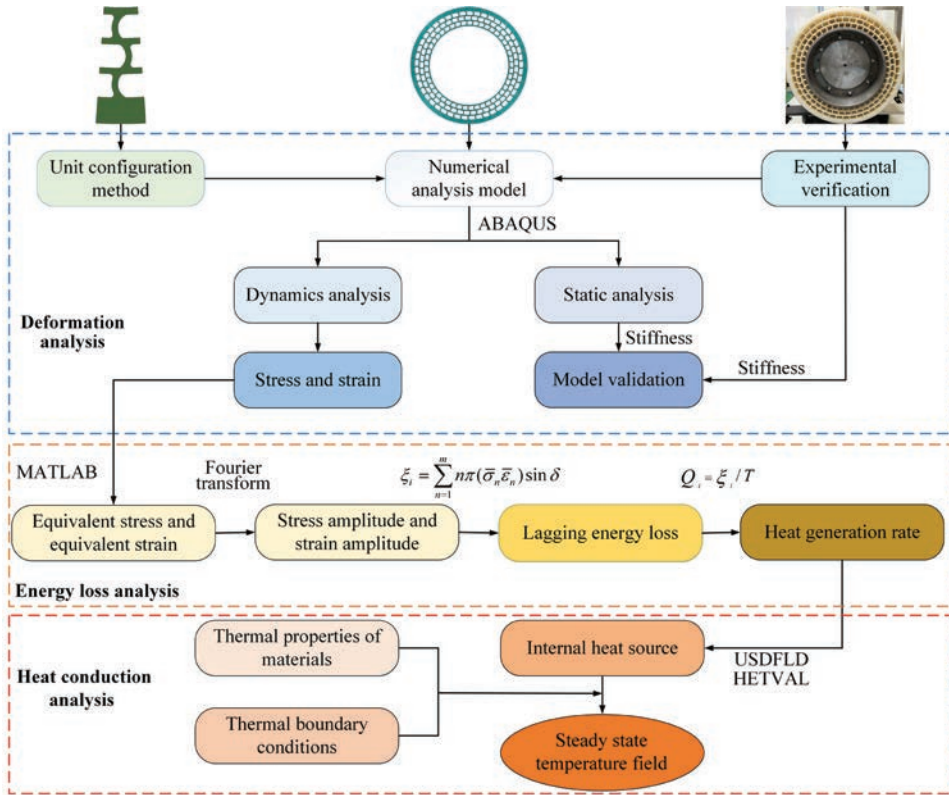
Fig. 4. *Flow chart of thermal mechanical coupling characteristics analysis*
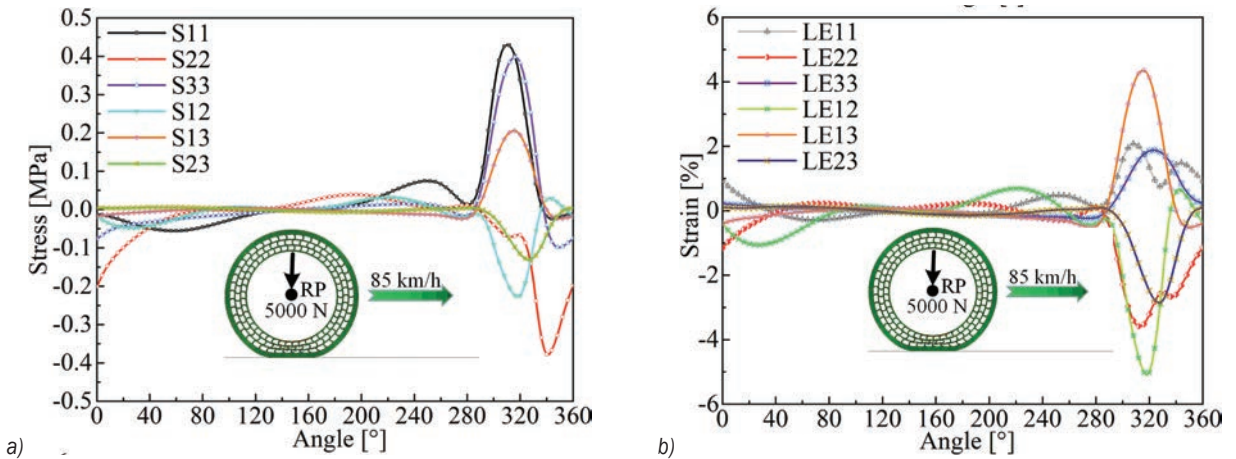
Fig. 5. *a) Stress and b) strain curve of a mesh element*

deformation, and the lagging phase angle δ appeared, as shown in Fig. 6a. Under the action of a cyclic load, the non-synchronization of stress and strain caused a hysteresis loop in the stress-strain curve of the material. The hysteresis area is basically the energy loss of the viscoelastic material, as shown in Fig. 6b. Assuming that the PU material is subjected to sinusoidal stress and strain, both variables can be expressed as:

$$\begin{cases} \sigma = \sigma_0 \sin(\omega t + \delta) \\ \varepsilon = \varepsilon_0 \sin\omega t \end{cases}, \qquad (2)$$

where σ is the stress; ε is the strain; σ_0 is the stress amplitude; ε_0 is the strain amplitude; ω is the angular frequency; δ is the lagging phase angle; t is the time.

According to the stress-strain relationship, the energy loss of the non-pneumatic tire in a rolling period T can be expressed as:

$$\xi = \int_0^T \sigma d\varepsilon. \tag{3}$$

Substituting Eq. (2) into Eq. (3) yields:

$$\xi = \pi\sigma_0\varepsilon_0\sin\delta, \tag{4}$$

where, $\sin\delta$ is the energy loss coefficient.

a)

b)
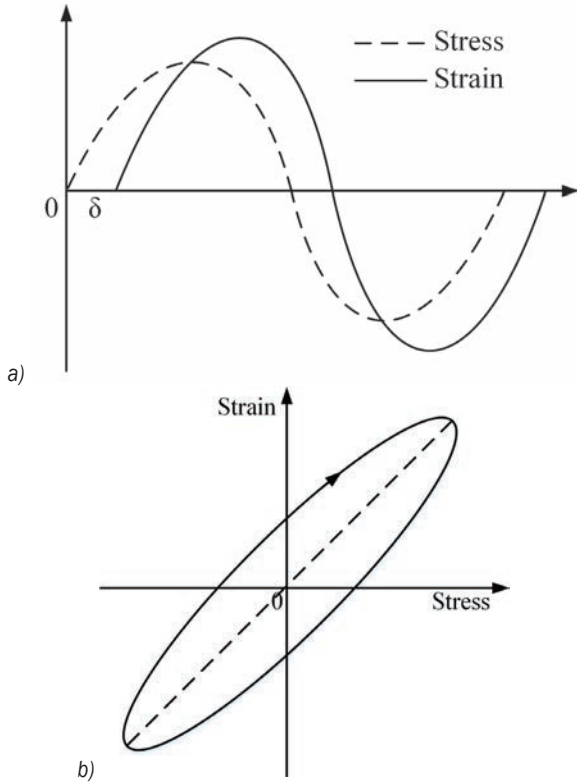
Fig. 6. *Stress-strain phase diagram;*
a) stress-strain phase relationship, and b) lagging loop

The energy loss of nonlinear viscoelastic PU materials mainly comes from the deformation of the materials. According to the strength theory of materials, the state of nonlinear materials can be expressed by an equivalent stress and an equivalent strain, which can be expressed as follows:

$$\begin{cases} \bar{\sigma} = \dfrac{3}{2\sqrt{2}}[(\sigma_x - \sigma_y)^2 + (\sigma_y - \sigma_z)^2 \\ \quad +(\sigma_z - \sigma_x)^2 + 6(\sigma_{xy}^2 + \sigma_{yz}^2 + \sigma_{zx}^2)]^{1/2} \\ \bar{\varepsilon} = \dfrac{3}{2\sqrt{2}}[(\varepsilon_x - \varepsilon_y)^2 + (\varepsilon_y - \varepsilon_z)^2 \\ \quad +(\varepsilon_z - \varepsilon_x)^2 + 6(\varepsilon_{xy}^2 + \varepsilon_{yz}^2 + \varepsilon_{zx}^2)]^{1/2} \end{cases} \tag{5}$$

According to Eq. (5), the equivalent stress $\bar{\sigma}$ and the equivalent strain $\bar{\varepsilon}$ of each mesh element were calculated in MATLAB, and fitted by the Fourier

series fitting method based on the least square method. The related equation is as follows:

$$\begin{cases} \sigma = \sigma_0 + \sum_{n=1}^{m}[\sigma_{1n}\cos(n\omega t) + \sigma_{2n}\sin(n\omega t)] \\ \quad = \sigma_0 + \sum_{n=1}^{m}\sqrt{\sigma_{1n}^2 + \sigma_{2n}^2}\sin(n\omega t + \theta_{\sigma n}) \\ \varepsilon = \varepsilon_0 + \sum_{n=1}^{m}[\varepsilon_{1n}\cos(n\omega t) + \varepsilon_{2n}\sin(n\omega t)] \\ \quad = \varepsilon_0 + \sum_{n=1}^{m}\sqrt{\varepsilon_{1n}^2 + \varepsilon_{2n}^2}\sin(n\omega t + \theta_{\varepsilon n}) \end{cases} \tag{6}$$

The constant m represents the fitting order. For most of the data, when $m = 8$, a better fitting value can be obtained, but a small part of the data loses its meaning. Therefore, we set five different orders of fitting from $m = 8$ to $m = 4$; when $m = 8$, the data lose its meaning, $m = 7$ will be used for fitting, and so on.

a)

b)
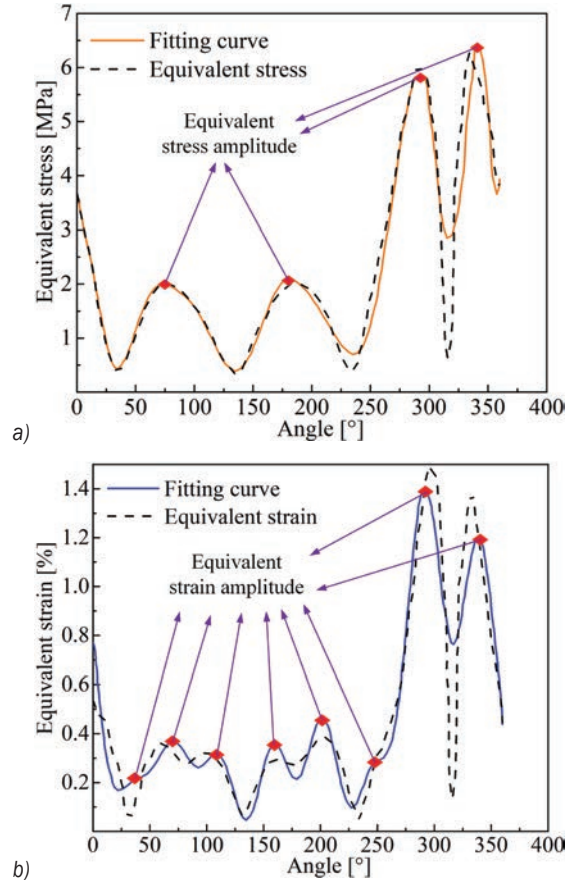
Fig. 7. *Fitting curve of equivalent stress and strain of a mesh element; a) equivalent stress; b) equivalent strain*

Fig. 7 shows the fitting curves of the equivalent stress and the equivalent strain of a randomly selected mesh element. It is clear that the equivalent stress and

equivalent strain cycle are anharmonic under steady-state rolling conditions. For the equivalent stress and equivalent strain cycle of anharmonic variation, it is necessary to express them as the superposition of a group of harmonics by the Fourier transformation, so as to obtain the equivalent stress amplitude and equivalent strain amplitude of each harmonic component at its corresponding frequency.

According to Eq. (6), the corresponding equivalent stress amplitude $\bar{\sigma}_n$ and equivalent strain amplitude $\bar{\varepsilon}_n$ can be calculated as follows:

$$\begin{cases} \bar{\sigma}_n = \sqrt{\sigma_{1n}^2 + \sigma_{2n}^2} \\ \bar{\varepsilon}_n = \sqrt{\varepsilon_{1n}^2 + \varepsilon_{2n}^2} \end{cases}. \qquad (7)$$

According to Eqs. (4) and (7), the energy loss ξ_i of each mesh element of the flexible spoke non-pneumatic tire in one rolling period T can be calculated according to Eq. (8):

$$\xi_i = \sum_{n=1}^{m} n\pi(\bar{\sigma}_n \bar{\varepsilon}_n)\sin\delta. \qquad (8)$$

The constant $\bar{\sigma}_n$ represents the equivalent stress amplitude; $\bar{\varepsilon}_n$ represents the equivalent strain amplitude; $\sin\delta$ represents the energy loss coefficient; m is the fitting order; i represents the element number (1 to 4170).

The ratio of the energy loss of each mesh element to the rolling period T is equal to the heat generation rate Q_i of each element, which can be expressed as follows:

$$Q_i = \xi_i / T, \qquad (9)$$

here, ξ_i is the energy loss of each mesh element, T is the rolling period, $T = \pi d / v$ in [s], d is the outer diameter of the tire [m], and v is the tire rolling speed [m/s].

2.4 Heat Conduction Analysis

In the heat conduction analysis, the heat generation rate calculated by ABAQUS is assigned to each mesh element as the heat load to complete the definition of the internal heat source. In this paper, two subroutines were used to define the internal heat sources: the subroutines USDFLD was used to redefine the field variables, and the subroutine HETVAL was used to define the internal heat source.

For the numerical simulation of the temperature field of the non-pneumatic tire, the following four assumptions are generally considered:

(1) The material properties of each part of the non-pneumatic tire are not influenced by temperature, and the entire energy loss in the rolling process is converted into heat, without heat loss.

(2) The temperature distribution is steady, and there is no temperature gradient in the circumferential direction of the non-pneumatic tire, meaning that the temperature distribution of each flexible spoke unit is exactly the same.

(3) The material of each part of the tire is isotropic.

(4) The non-pneumatic tire will be in thermal equilibrium after rolling at a constant speed for some time.

According to the above assumptions, the material is endowed with thermal properties and thermal boundary conditions are set. The thermal properties of the PU material mainly include thermal conductivity, thermal expansion coefficient, specific heat and convective thermal transfer coefficient, as shown in Table 2.

Table 2. *Thermal properties of PU material*

Thermal properties	Parameter
Thermal conductivity k [W/(m·K)]	0.3
Thermal expansion coefficient a [°C⁻¹]	0.0002
Specific heat c [J/(kg·K)]	2×10^9

The thermal boundary conditions of the flexible spoke non-pneumatic tire include the tread boundary in contact with the ground, body surface boundary in contact with air and inner circle boundary in contact with the rigid hub. In the actual rolling process, the heat exchange between the tread and the road, as well as that between the flexible spoke inner ring and the rigid hub, can be calculated in the form of thermal conduction. The heat exchange between the flexible spoke support body and the air can be calculated in the form of convective thermal transfer. The convective heat transfer coefficient is approximately described according to the following equation:

$$h = 2.2v^{0.84}, \qquad (10)$$

here, h is the convective heat transfer coefficient of the surface boundary of the body [W/(m²·K)], and v is the tire rolling speed in [m/s].

3 RESULT ANALYSIS

3.1 Analysis of Overall Distribution Trend of Steady-state Temperature Field

Fig. 8 shows the comparison diagram of steady-state temperature field distribution and the stress distribution under a vertical load of 5000 N and a driving speed of 85 km/h. The vertical load led to greater deformation in the middle part of the flexible spoke unit, causing greater stress and strain and increased energy loss, resulting in more heat generation. Therefore, the high-temperature region is mainly distributed in the middle bending part of the flexible spoke unit, which is consistent with the main stress deformation part. The overall temperature gradually decreases from the centre of the flexible spoke unit to the surrounding area, and the central temperature reached 71.9 °C. The problem of local high temperatures can be solved by improving the structure of the flexible spoke unit and reducing the stress concentration.

3.2 Influence of Driving Speed on Steady-state Temperature Field Distribution

Fig. 9 shows the steady-state temperature field distribution trend of the flexible spoke non-pneumatic tire under a vertical load of 5000 N at different driving speeds. Figs. 9a, b, and c show the temperature distributions of a flexible spoke unit for different driving speeds; Figs. 9d and e show the temperature distribution trend maps of each node on the vertical axis and lateral axis of flexible spoke unit. According to Figs. 9a, b, and c, with the increase in the driving speed, the temperature distribution of the flexible spoke non-pneumatic tire was almost unchanged. This indicates that the driving speed did not influence the temperature distribution patterns and characteristics of the non-pneumatic tire, but both the overall temperature and the maximum temperature slightly increase with the increase of the driving speed; in fact, the maximum temperature increased from 58.3 °C to 71.9 °C. According to the energy loss analysis, with the increase of driving speed, the rolling period of the non-pneumatic tire became gradually shorter. The heat generation rate of each mesh element increased as well, which implies the overall temperature of the non-pneumatic tire increased. It can be seen from Figs. 9d and e that under different driving speeds, the node temperature on the vertical axis and lateral axis of the flexible spoke unit showed a tendency of first increasing and then decreasing, and the temperature at the centre of the flexible spoke was higher than that at the edge of it. With the increase of driving speed, the temperature rise in the centre of the flexible spoke is greater than that at the edge of it. When the driving speed increased from 45 km/h to 65 km/h, the maximum temperature of the node was increased by 4.19 °C; when the driving speed increased from 65 km/h to 85 km/h, the maximum temperature of the node was increased by 8.44 °C, indicating that the influence of the driving speed on the temperature change of the non-pneumatic tire is greater under high speed than under the low speed condition.
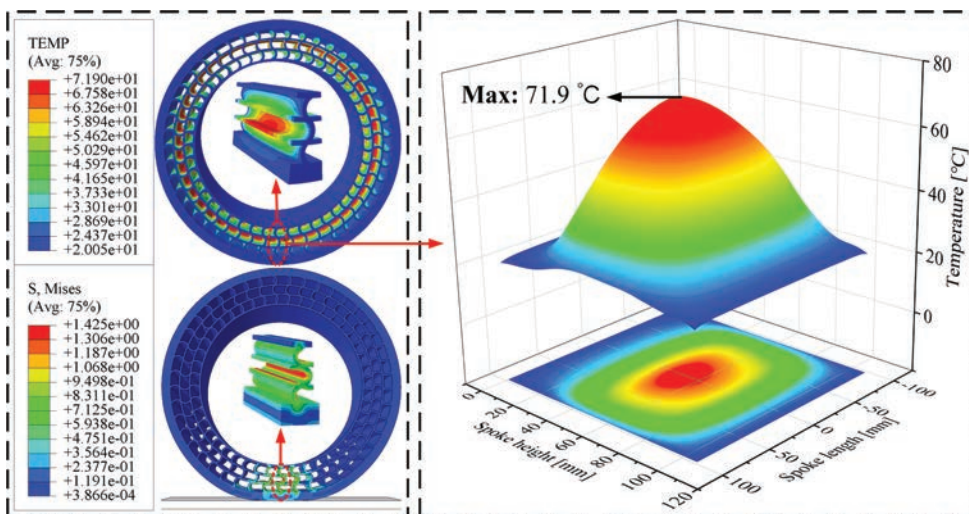
Fig. 8. *Comparison diagram of steady-state temperature field distribution and stress distribution*
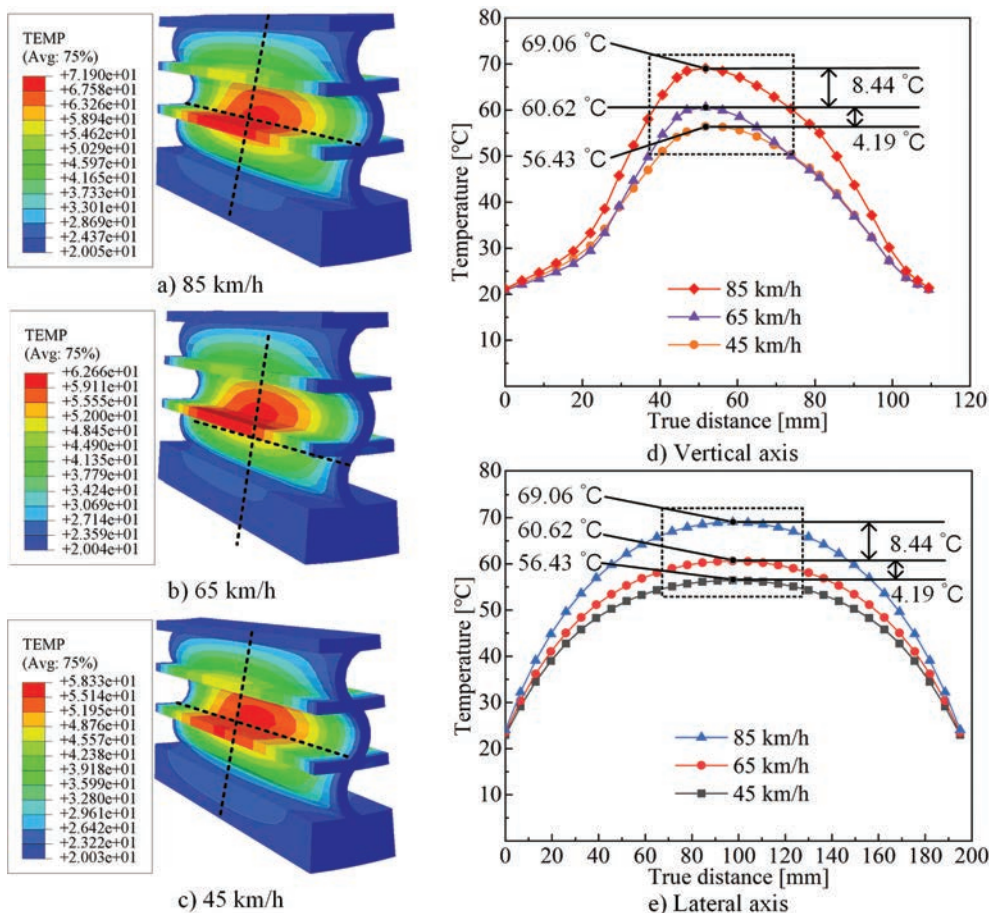
Fig. 9. *Steady-state temperature field distribution under different driving speeds*

3.3 Influence of Load on Steady-state Temperature Field Distribution

Fig. 10 shows the steady-state temperature field distribution trend of the flexible spoke non-pneumatic tire under different loads at the driving speed of 85 km/h. Figs. 10a, b, and c show the temperature field distribution maps of the flexible spoke unit under different loads, and Figs. 10d and e show the temperature distribution trend maps of each node on the vertical axis and lateral axis of the flexible spoke unit.

According to Figs. 10 a, b, and c, the change of load has little influence on the temperature distribution of the flexible spoke non-pneumatic tire, and the high-temperature region always existed in the central part of the flexible spoke unit. However, the overall and maximum temperature of the non-pneumatic tire increased significantly with the increase of the load, and, in fact, the maximum temperature increases

from 31.9 °C to 71.9 °C. According to the energy loss analysis, with the increase of the load, the sinking amount of non-pneumatic tire gradually increased, and the deformation amplitude of each part of the tire increased as well, which increased the stress amplitude, strain amplitude, and the energy loss of each mesh element, resulting in an increase of the heat generation rate. It can be seen from Figs. 10 d and e that under different loads, the node temperature on the vertical axis and lateral axis of the flexible spoke unit showed a tendency of first increasing and then decreasing, and the temperature at the centre of the flexible spoke was higher than that at the edge of the flexible spoke. With the increase of the load, the temperature rise at the centre of the flexible spoke was significantly greater than that at the edge of the flexible spoke. In addition, the temperature rise amplitude caused by the load increasing from 3000 N to 4000 N was almost the same as that caused by the load increasing from 4000 N to 5000 N. This
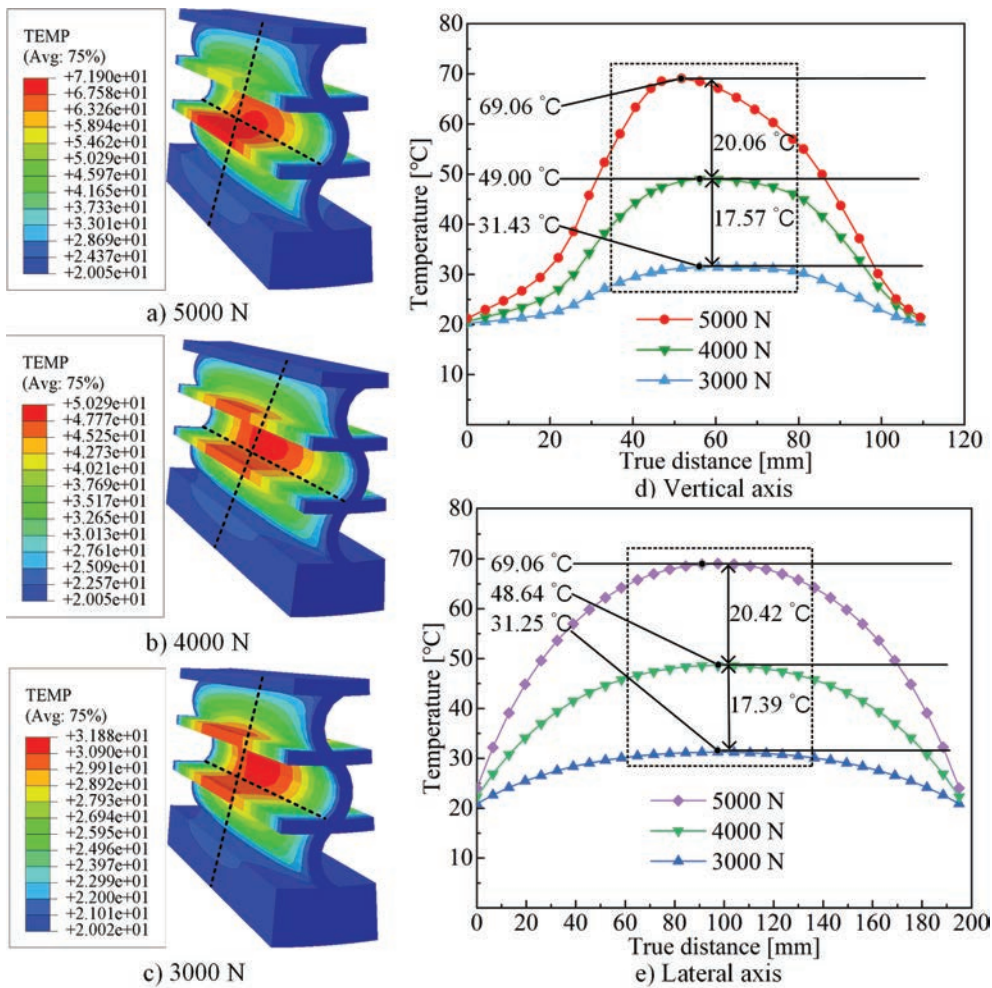
Fig. 10. *Steady-state temperature field distribution under different loads*

indicates that the influence of the load change on the temperature of the flexible spoke non-pneumatic tire has nothing to do with the loading conditions of the tire.

4 CONCLUSIONS

The 3D model and numerical analysis model of the 195/50N16 flexible spoke non-pneumatic tire were established based on the unit configuration method. The thermo-mechanical sequential coupling method was used to carry out a deformation analysis, an energy loss analysis, and a heat conduction analysis on the flexible-spoke non-pneumatic tire. The temperature distribution of the flexible spoke non-pneumatic tire under the influence of thermo-mechanical coupling was obtained. After comparative analysis, the conclusions are as follows:

1. The high temperature region of the flexible spoke non-pneumatic tire is mainly concentrated in the middle bending part of the flexible spoke unit, which is consistent with the main stress deformation part. The overall temperature gradually decreases from the centre of the flexible spoke to the surrounding parts.

2. Under the condition of constant vertical load, the overall temperature and the maximum temperature of the non-pneumatic tire increase slightly with the increase of the driving speed. The centre temperature of the flexible spoke unit is higher than the edge temperature of the flexible spoke unit, and with the increase of the driving speed, the temperature rise of the centre of the flexible spoke unit is greater than that of the edge of the flexible spoke unit. The influence of the driving speed on the temperature change of

the non-pneumatic tire is greater at higher speeds than that at lower speeds.

3. Under the condition of constant driving speed, the overall temperature and the maximum temperature of the non-pneumatic tire increase significantly with the increase of the load. The centre temperature of the flexible spoke unit is higher than the edge temperature of the flexible spoke unit. With the increase of the vertical load, the temperature rise of the centre of the flexible spoke unit is significantly greater than that of the edge of the flexible spoke unit, and the overall temperature rise is larger. The influence of load change on the temperature of the flexible spoke non-pneumatic tire has nothing to do the loading conditions of the tire.

4. Both the driving speed and the vertical load affect the overall temperature and the maximum temperature of the flexible spoke non-pneumatic tire. However, the load has a significantly larger influence on the temperature change than the driving speed. Therefore, it is possible to increase the driving speed appropriately under the condition of reducing the load, and thus solve the problem of high temperature failure caused by high-speed operation for current non-pneumatic tires.

5 ACKNOWLEDGEMENTS

6 REFERENCES

[1] Zhang, Z.F., Fu, H.X., Liang, X. M., Chen, X. X., Tan, D. (2020). Comparative analysis of static and dynamic performance of non-pneumatic tire with flexible spoke structure. *Strojniški vestnik - Journal of Mechanical Engineering*, vol. 66, no. 7-8, p. 458-466, DOI:10.5545/sv-jme.2020.6676.

[2] Zhang, Z.Z., Lv, J.G., Song, B., Guo, S.Y., Gao, F. (2013). Development of Non-Pneumatic Tire Technology. *Applied Mechanics and Materials*, vol. 427-429, p. 191-194, DOI:10.4028/www.scientific.net/AMM.427-429.191.

[3] Mathew, N.J., Sahoo, D.K., Chakravarthy, E.M. (2017). Design and static analysis of airlesstyre to reduce deformation. *Materials Science and Engineering Conference Series*, vol. 197, DOI:10.1088/1757-899X/197/1/012042.

[4] Veeramurthy, M. (2011). *Modeling, Finite Element Analysis, and Optimization of Non-Pneumatic Tire (NPT) for the Minimization of Rolling Resistance*. BSc Thesis, Clemson University, Clemson.

[5] Narasimhan, A., Ziegert, J., Thompson, J. (2011). Effects of material properties on static load-deflection and vibration of a non-pneumatic tire during high-speed rolling. *SAE International Journal of Passenger Cars-Mechanical Systems*, vol. 4, no. 1, p. 59-72, DOI:10.4271/2011-01-0101.

[6] Ju, J., Kim, D.-K., Kim, K. (2012). Flexible cellular solid spokes of a non-pneumatic tire. *Composite Structures*, vol. 94, no. 8, p. 2285-2295, DOI:10.1016/j.compstruct.2011.12.022.

[7] Zhao, Y.Q., Zhu, M.M., Lin, F., Xiao, Z., Li, H.Q., Deng, Y.J. (2018). Thermal modal analysis of novel non-pneumatic mechanical elastic wheel based on FEM and EMA. *AIP Advances*, vol. 8, art. ID 015229, DOI:10.1063/1.5018488.

[8] Wang, Z.P. (2010). Finite element analysis of mechanical and temperature field for a rolling tire. *International Conference on Measuring Technology and Mechatronics Automation*, p. 278-283, DOI:10.1109/icmtma.2010.42.

[9] Gasmi, A., Joseph, P.F., Rhyne, T.B., Cron, S.M. (2012). Development of a two-dimensional model of a compliant non-pneumatic tire. *International Journal of Solids & Structures*, vol. 49, no. 13, p. 1723-1740, DOI:10.1016/j.ijsolstr.2012.03.007.

[10] Kucewicz, M., Baranowski, P., Maachowski, J. (2016). Airless tire conceptions modeling and simulations. *1st Renewable Energy Sources-Research and Business*, p. 293-301, DOI:10.1007/978-3-319-50938-9_30.

[11] Xu, H., Zhao, Y.Q., Ye, C., Lin, F. (2019). Integrated optimization for mechanical elastic wheel and suspension based on an improved artificial fish swarm algorithm. *Advances in Engineering Software*, vol. 137, art. ID 102722, DOI:10.1016/j.advengsoft.2019.102722.

[12] Mazur, V.V. (2020). Experiments to find the rolling resistance of non-pneumatic tires car wheels. *Proceedings of the 5th International Conference on Industrial Engineering*, p. 641-648, DOI:10.1007/978-3-030-22041-9_69.

[13] Ju, J., Veeramurthy, M., Summers, J.D., Thompson, L.L. (2013). Rolling resistance of a non-pneumatic tire having a porous elastomer composite shear band. *Tire Science & Technology*, vol. 41, no. 3, p. 154-173, DOI:10.2346/tire.13.410303.

[14] Jackowski, J., Wieczorek, M., Żmuda, M. (2018). Energy consumption estimation of non-pneumatic tire and pneumatic tire during rolling. *Journal of KONES Powertrain and Transport*, vol. 25, no. 1, p. 159-168, DOI:10.5604/01.3001.0012.2463.

[15] Fu, H.X., Zhao, Y.Q., Du, X.B., Wang, Q., Xiao, Z. (2017). Analysis on influencing factors of lateral stiffness of mechanical elastic wheel. *Journal of Shanghai Jiaotong University*, vol. 51, no. 7, p. 863-869, DOI:10.16183/j.cnki.jsjtu.2017.07.014. (in Chinese)

[16] Fu, H.X., Zhao, Y.Q., Lin, F., Du, X.B., Zhu, M.M. (2017). Steady-state cornering properties of a non-pneumatic tire with mechanical elastic structure. *Transactions of Nanjing University of Aeronautics and Astronautics*, vol. 34, no. 5, p. 586-592, DOI:10.16356/j.1005-1120.2017.05.586. (in Chinese)

[17] Zang, L.G., Zhao, Y.Q., Li, B., Wang, J., Fu, H.X. (2016). An experimental study on the ground contact characteristics of non-pneumatic mechanical elastic wheel. *Automotive*

Engineering, vol. 38, no. 3, p. 350-355, **DOI:10.19562/j. chinasae.qcgc.2016.03.014.** (in Chinese)

[18] Du, X.B., Zhao, Y.Q., Wang, Q., Fu, H.X., Lin, F. (2019). Grounding characteristics of a non-pneumatic mechanical elastic tire in a rolling state with a camber angle. *Strojniški vestnik-Journal of Mechanical Engineering*, vol. 65, no. 5, p. 287-296, **DOI:10.5545/ sv-jme.2018.5845**.

[19] Sriwijaya, R., Hamzah, R. (2019). The effect of surface contact on the pressure distribution and deflection of airless tires. *AIP Conference Proceedings*, vol. 2187, art ID. 050021, **DOI:10.1063/1.5138351**.

[20] Zhang, T.H., Xu, Z., Wang, W. (2018). Finite element analysis and prediction on static grounding performance and fatigue life of staggered non-pneumatic tire. *China Rubber Industry*, vol. 65, no. 12, p. 1383-1386. (in Chinese)

[21] Li, Q.L., Fan, L.C., Li, T. (2011). Determination of thermo-physical properties of rubber and its effect on curing temperature field of tire. *Advanced Materials Research*, vol. 221, p. 533-539, **DOI:10.4028/www.scientific.net/ AMR.221.533.**

[22] Yan, X.Q. (2007). A numerical modeling of dynamic curing process of tire by finite element. *Polymer Journal*, vol. 39, p. 1001-1010, **DOI:10.1295/polymj.pj2006182**.

[23] Chen, Y.Q., Zhao, Y.Q., Ruan, M.Q., Li, B., Zang, L.G. (2016). Finite element analysis on steady-state temperature field of a rolling mechanical elastic wheel. *Mechanical Science & Technology for Aerospace Engineering*, vol. 35, no. 3, p. 364-369, **DOI:10.13433/j.cnki.1003-8728.2016.0307.** (in Chinese)

[24] Zhu, M.M., Zhao, Y.Q., Xiao, Z., Deng, Y.J. (2018). Surface temperature prediction of novel non-pneumatic mechanical elastic wheel based on theory analysis and experimental verification. *Numerical Heat Transfer Part B: Fundamentals*, vol. 73, no. 6, p. 399-414, **DOI:10.1080/10407790.2018.149 1721.**

Investigation and Optimization of MQL System Parameters in the Roller-Burnishing Process of Hardened Steel

An-Le Van[1] – Trung-Thanh Nguyen[2,*]

[1]Nguyen Tat Thanh University, Faculty of Engineering and Technology, Vietnam
[2]Le Quy Don Technical University, Faculty of Mechanical Engineering, Vietnam

In the current study, the internal burnishing process under the minimum quantity lubrication (MQL) condition has been optimized to decrease the cylindricity (CYL) and circularity (CIC) of the burnished hole, while the surface roughness (SR) is predefined as a constraint. The optimizing inputs are the diameter of the spray nozzle (D), the spray elevation angle (A), the lubricant quantity (Q), and the pressure value of the compressed air (P). The artificial neural network (ANN) models of burnishing performances are proposed to optimise inputs. The grey relational analysis (GRA) is utilized to compute the weight value of each response. Optimal values of MQL system parameters and technological objectives are selected with the aid of an evolution algorithm (vibration and communication particle swarm optimization (VCPSO) algorithm). The results indicated that the optimal outcomes of the D, A, Q, and P are 1.5 mm, 50 deg, 140 ml/h, and 0.6 MPa, respectively. Furthermore, the CYL, CIC, and SR were decreased by 53.14 %, 57.83 %, and 72.97 %, respectively, at the optimal solution. Finally, the obtained results are expected to be a significant solution to support the machine operator in selecting the optimal MQL system parameters to improve the hole quality in the MQL-assisted burnishing process.
Keywords: internal burnishing; cylindricity; circularity; roughness; ANN; VCPSO

Highlights
- *Optimization of MQL system parameters, including the diameter of the spray nozzle, spray elevation angle, lubricant quantity, and pressure value of the compressed air.*
- *Consideration of the cylindricity, circularity, and surface roughness.*
- *Development of ANN models for burnishing responses.*
- *Selection of optimal MQL parameters using VCPSO.*

0 INTRODUCTION

The coolant was widely applied to decrease the temperature and friction for different machining operations. However, the massive application of the lubricant increases its cost far higher than the cost of cutting tools, endangers human health, and creates environmental pollution [1]. Manufacturing costs, health, and environmental issues motivate manufacturing enterprises to reduce and eliminate lubricants. Dry machining is the manufacturing operation without the use of any lubricant, which is becoming popular due to environmental safety and worker health [2]. Unfortunately, this method is restricted to the machining of low-strength material with moderate cutting conditions [3] and [4]. An alternative solution is minimum quantity lubrication (MQL), in which a very low amount of fluid (5 ml/h to 200 ml/h) is used in conjunction with compressed air. For different machining of hardened steels and titanium alloys, MQL is a feasible, efficient, and eco-friendly alternative, compared to dry and flood-cooling methods [5].

The MQL method was widely utilized to boost the technical performances of different machining processes. The optimal values of the lubricant quantity (Q), cutting speed (V), and feed rate (f) were selected to decrease the cutting force (CF) of the milling AISI 4140 steel [6]. The specific cutting energy (SCE) model was developed in terms of the V, f, Q, and depth of cut (d) for the MQL end milling process [7]. Moreover, the MQL resulted in 33 % less power consumption (PW) in comparison with the wet approach [8]. Rajan et al. [9] emphasized that the MQL exhibited 157.3 % and 40 % less tool wear (TW) for the turning operation in dry and flood conditions, respectively. Sivaiah et al. [10] revealed that the SR and TW were decreased by 54 % and 7 %, respectively, while the material removal rate (MRR) was improved by 27 % for the MQL turning AISI 304. Moreover, the MQL mode could help increase the feed rate by 40 % in the turning EN31 steel [11]. Zhang et al. [12] indicated that the specific grinding energy was significantly decreased using nanoparticle-based MQL. The combination of the MQL and cooled air could be applied to decrease 10.5 % grinding force and 36.3 % roundness errors [13]. A hybrid approach comprising the MQL and water could provide higher cooling-lubrication efficiency [14]. Faverjon et al. [15] stated that the MQL was effectively applied

to decrease the thermal distortion and enhance the machined accuracy of the drilled aluminium part. The *SR* and burr height (*BH*) of the drilled hole were significantly reduced under the MQL condition [16]. MQL could be employed to improve the surface morphologies for the drilled composites [17].

The employment of the MQL system in burnishing operations has been rarely addressed in published investigations. The MQL-based diamond-burnishing process was developed and optimized, in which the optimal process parameters, including the spindle speed (S), burnishing force (F_b), and f, were selected to decrease the *SR* and improve the surface hardness (*SH*) [18]. Similarly, the surface integrity of the burnished titanium alloy was significantly improved using optimal MQL conditions [19]. As a result, missing gaps of the previous publications can be expressed as follows.

The influences of MQL operating parameters, including the nozzle diameter, spray angle, lubricant quantity, and air pressure on geometric errors, have not been analysed in the published investigations. Moreover, predictive models of the cylindricity and circularity regarding the MQL operating parameters for the burnishing operation have not been proposed.

Fig. 1. *Burnishing experiment*

The selection of optimal MQL operating parameters for decreasing geometrical deviations (cylindricity and circularity) and surface roughness for the burnishing operation has not been addressed. The diameter and number of droplets were primarily affected by the lubricant quantity, air pressure, and nozzle diameter, while the machining zone wettability was mainly influenced by the nozzle distance and lubricant quantity [20] and [21]. The spraying angle was related to the workpiece to be machined [22]. Therefore, the optimum setting of MQL system

parameters may provide better penetration of the lubricant at the rollers-workpiece interfaces.

1 MATERIAL METHOD

Hardened specimens labelled 5145 are drilled and turned using a computer numerical control (CNC) lathe machine (CTX 400E). The drill tool with a diameter of 16 mm is used to produce the rough hole, in which a feed rate of 0.5 mm/rev, a depth of cut of 8 mm, and a spindle speed of 400 RPM are used as the drilling parameters. Multiple turning paths using polycrystalline cubic boron nitride (CBN) inserts are adopted to turn the internal holes, in which a feed rate of 0.25 mm/rev, a depth of cut of 1 mm, and a spindle speed of 800 RPM are turning factors. The length, internal diameter, and external diameter of each workpiece are 60 mm, 28 mm, and 40 mm, respectively. The cylindricity, circularity, and surface roughness of the pre-machined hole are 70.62 µm, 18.48 µm, and 3.84 µm, respectively.

The burnishing trials are done with the aid of a milling machine, in which the workpiece is positioned and tightly clamped using a jaw-centring chuck (Fig. 1). Soybean oil has been selected as the lubricant and mixed with the compressed air to form the mixture (air-oil mist), which is delivered into the machining region through MQL nozzles. The Mitutoyo Surftest-301 and ZEISS CONTURA G2 are employed to capture the surface roughness, cylindricity, and circularity values.

2 OPTIMIZING FRAMEWORK

The schematic illustration of the internal roller burnishing operation under the MQL condition is depicted in Fig. 2. The MQL system parameters, including the diameter of the spray nozzle, the spray elevation angle, the lubricant quantity, and the pressure value of the compressed air, are presented in Table 1. The ranges of each factor are determined with the aid of the MQL system's characteristics and the manufacturer's recommendations.

Table 1. *MQL system parameters*

Symbol	Parameters	1	2	3
D	Nozzle diameter [mm]	0.5	1.0	1.5
A	Spray angle [deg]	25	45	65
Q	Lubricant quantity [ml/h]	40	90	140
P	Air pressure [MPa]	0.2	0.4	0.6
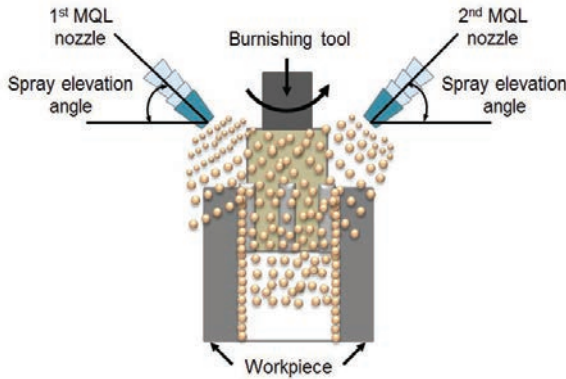
Fig. 2. *The schematic illustration of the internal burnishing operation*
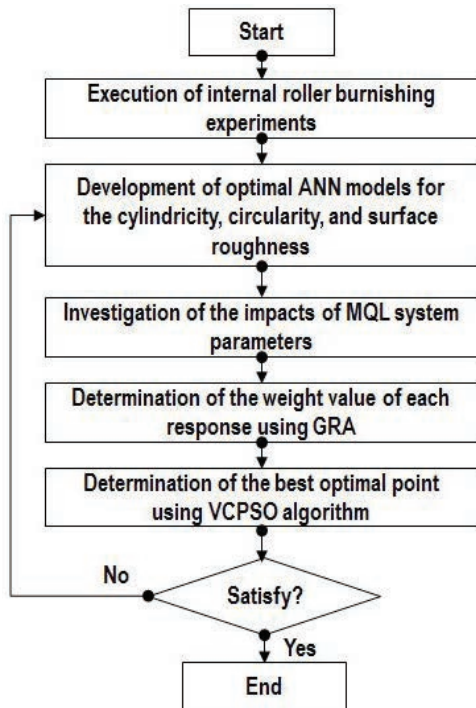
Fig. 3. *The optimization approach fo r the internal burnishing operation*

The optimization procedure is presented in Fig. 3, which is shown as bellows:

Step 1: The burnishing experiments are executed based on the Box-Behnken design to save the experimental cost [23] and [24].

Step 2: The *CYL*, *CIC*, and *SR* models are developed in terms of the MQL system parameters using the ANN approach [25]. The output of the neuron is a function of all inputs and their weights and expressed as [26]:

$$I_j = \sum input_i \times w_{ij}, \quad (1)$$

$$Output_j = f_n(I_j + t_j), \quad (2)$$

where I_j, w_{ij}, t_i, and f_n present the internal value, weight, threshold value, and transfer function, respectively.

The numerical simulations of the ANN model are conducted to calculate the percentage error (PE):

$$PD = \left(\frac{y_a - y_p}{y_a} \right) \times 100, \quad (3)$$

where y_a and y_p are actual and predicted data, respectively. The best architecture of the ANN model with the PE value less than 10 %.

The R^2 value and root mean square error (*RMSE*) are named as important indicators to investigate the adequacy of the developed models and computed as:

$$R^2 = 1 - \left(\frac{\sum_{i=1}^{n}(y_{pi} - y_{ai})^2}{\sum_{i=1}^{n}(y_{ai})^2} \right), \quad (4)$$

$$RMSE(\%) = \sqrt{\frac{1}{n} \sum_{i=1}^{n} \left(y_{pi} - y_{ai} \right)^2}. \quad (5)$$

Step 3: The weight value of each response is determined using the grey relation analysis (GRA).

The correlation coefficient is calculated as:

$$S_{jl} = \left[\frac{Cov(I_i(j), I_i(l))}{\sigma_{Ii}(j) \times \sigma_{Ii}(l)} \right], \quad (6)$$

where $Cov(I_i(j))$ and $I_i(l)$ presents the covariance of sequences $I_i(j)$ and $I_i(l)$, respectively.

The eigenvalues and consequent eigenvectors are calculated as:

$$(S - \lambda_k J_m)V_{ik} = 0, \quad (7)$$

where λ_k, V_{ik}, and J_m presents the eigenvalues, eigenvectors, and the identity matrix, respectively.

The major principal coefficient is calculated as:

$$PC_m = \sum_{i=1}^{n} I_m(i) \times V_{ik}, \quad (8)$$

Step 4: The optimal outcomes of the MQL system factors and technical responses are selected using the VCPSO algorithm. Practically, the results produced by the PSO are easily failed into the local optimizing outcomes due to the lack of communication among entire particles. To obtain the global solution, communication with three operations (i.e., the mutation, crossover, and selection) is performed.

The mutation is conducted to exchange information between old and new particles. The mutation operator is expressed as:

$$x_i^{son} = x_{ra} + F(x_{rb} - x_{rc}), \qquad (9)$$

where ra, rb, and rc are random integers in the range $(0, N)$. The F is the scaling factor.

In the crossover stage, the trial vector u_i^{son} is produced to increase the diversity of the population on the basis of the mutation operator. The crossover operation is expressed as:

$$u_{i,d}^{son} = \begin{cases} x_{i,d}^{son} & if\ (rand < CR) \\ x_{i,d}^{son} & otherwise \end{cases}, \qquad (10)$$

where CR is the crossover rate with the range of $(0, 1)$, d_{rand} is a random number from $(1, 2, \ldots, D)$.

The selection operator is enabled to choose better particle between u_i^{son} and x_i using the fitness function, which is expressed as:

$$u_{i,d}^{son} = \begin{cases} x_{i,d}^{son} & if\ (f(u_i^{son}) < f(x_i)) \\ x_{i,d}^{son} & otherwise \end{cases}, \qquad (11)$$

The equations of the VCPSO algorithm are expressed as follows:

$$v_{id}^{n+1} = \omega v_{id}^n + c_1 r_1 (P_{id}^n - x_{id}^n) + c_2 r_2 (P_{gd}^n - x_{id}^n)$$
$$+ c_3 r_3 (P_{cd}^n - x_{id}^n), \qquad (12)$$

$$x_{id}^{n+1} = x_{id}^n + v_{id}^{n+1}, \qquad (13)$$

where c_3 is the accelerated coefficient, while the r_1, r_2 and r_3 are random numbers in range $(0, 1)$, respectively.

3 RESULTS AND DISCUSSIONS

3.1 Development of the Optimal ANN Models

The experimental data of the internal burnishing operation are presented in Table 2, in which the obtained data from experiments No. 1 to 26 are applied to construct the ANN models. The obtained data from experiments No. 27 to 38 are employed to test the accuracy of the developed models. The representative values of the experiments are shown in Fig. 4.

The working parameters of the ANN model are the NT, NN, TF, PM, TS, NL, and LF and their levels are shown in Table 3.

As a result, the training function and the number of hidden neurons have the highest level (14) and the learning function has the minimum level (2). Consequently, the orthogonal array matrix with 256 trials is employed to perform computational trials. The obtained results with the PE values less than 10 % for the ANN model are presented in Table 4. As a result, the optimal outcomes of the NT, NN, TF, PM, TS, NL,

and LF are FFNN, TrainLM, 25, MSE, Logsig, 3, and Learn GDM, respectively (the trial No. 146). The PE values of the *CYL*, *CIC*, and *SR* are 3.46 %, 4.21 %, and 3.74 %, respectively. The network with a (4-25-25-25-3) topology has been used for predicting the input-output parameters. The schematic view of the developed ANN model is shown in Fig. 5.
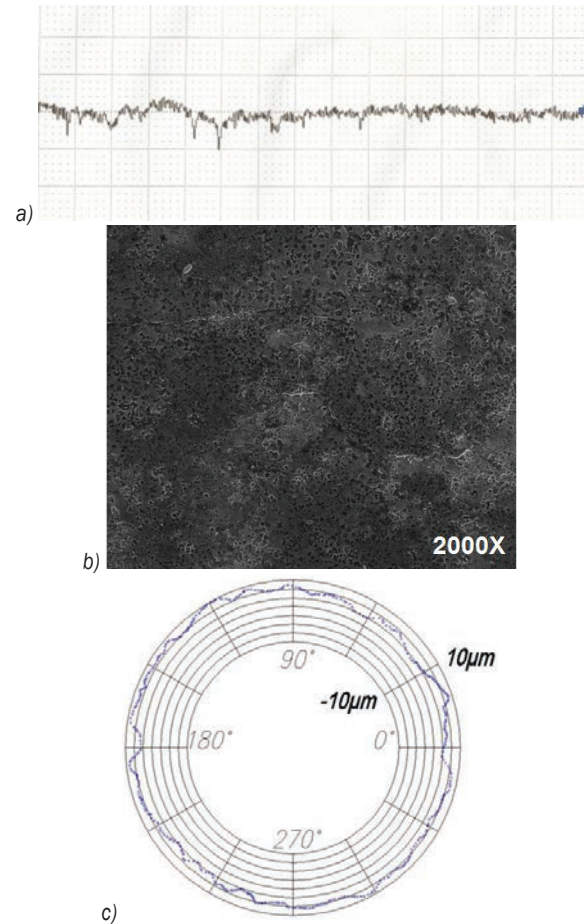
Fig. 4. *Representative results;*
a) the roughness profile at the No. 21, b) the SEM image of the burnished surface, c) the circularity at the No. 21

The R^2 value and RMSE of the *CYL* model are 0.9652 and 0.0532, respectively. The R^2 value and RMSE of the *CIC* model are 0.9608 and 0.0621, respectively. The R^2 value and RMSE of the *SR* model are 0.9648 and 0.0469, respectively. Therefore, it can be stated that the developed ANN models are adequate and significant.

To investigate the accuracy of the developed ANN model, a set of experiments is performed at random points. The comparisons between the predicted and experimental results are presented in Table 5. The errors of the *CYL*, *CIC*, and *SR* lie within the range

Table 2. *Experimental data for the internal burnishing process*

	No.	D [mm]	A [deg]	Q [ml/h]	P [MPa]	CYL [μm]	CIC [μm]	SR [μm]
	1	1.0	65	90	0.2	35.24	14.35	0.42
	2	1.5	65	90	0.4	22.37	10.97	0.34
	3	0.5	25	90	0.4	33.99	17.18	0.52
	4	1.0	25	90	0.2	36.88	15.98	0.48
	5	1.0	65	90	0.6	25.15	9.22	0.27
	6	1.0	25	140	0.4	21.92	11.96	0.29
	7	1.5	45	40	0.4	23.33	12.92	0.41
	8	1.5	45	140	0.4	12.28	6.92	0.21
	9	1.0	25	40	0.4	35.43	18.58	0.51
	10	1.0	25	90	0.6	28.67	12.78	0.32
	11	1.0	45	90	0.4	21.42	9.49	0.38
Experimental data	12	1.0	45	40	0.2	32.88	14.92	0.53
for developing	13	0.5	65	90	0.4	31.69	14.52	0.44
ANN models	14	0.5	45	90	0.6	21.36	10.22	0.35
	15	1.0	65	140	0.4	20.63	9.96	0.23
	16	1.0	45	140	0.2	21.28	9.26	0.28
	17	0.5	45	90	0.2	33.71	13.35	0.51
	18	1.5	25	90	0.4	24.82	12.96	0.38
	19	0.5	45	40	0.4	32.65	16.97	0.54
	20	1.0	65	40	0.4	32.38	16.18	0.45
	21	1.0	45	140	0.6	12.29	5.98	0.14
	22	1.5	45	90	0.6	15.27	5.69	0.16
	23	1.0	45	40	0.6	23.86	12.92	0.36
	24	1.0	45	90	0.4	21.49	9.58	0.37
	25	1.5	45	90	0.2	23.15	10.78	0.39
	26	0.5	45	140	0.4	19.86	9.26	0.38
	27	0.5	40	50	0.5	29.36	15.83	0.53
	28	0.5	40	70	0.4	29.29	14.27	0.51
	29	0.5	30	90	0.3	34.12	15.51	0.54
	30	0.5	45	90	0.6	22.31	10.66	0.36
Experimental data	31	1.0	45	70	0.4	23.82	11.18	0.41
for testing the	32	1.0	40	90	0.5	20.45	9.22	0.33
accuracy	33	1.0	45	100	0.6	17.66	6.99	0.23
of developed	34	1.0	50	100	0.4	20.43	8.93	0.34
ANN models	35	1.5	40	90	0.5	16.84	7.85	0.27
	36	1.5	50	110	0.3	17.59	8.78	0.31
	37	1.5	30	90	0.6	21.11	9.24	0.21
	38	1.5	60	70	0.2	28.52	13.46	0.44

of -2.05 % to 2.38 %, -2.17 % to 2.91 %, and -4.76 % to 3.70 %, respectively. The accepted deviations (less than 5.0 %) indicated that the proposed models could be applied to forecast the burnishing performances with good accuracy.

3.2 ANOVA Results for Technological Responses

Table 6 presents ANOVA results for the *CYL* model with significant factors. The computed participations of the *D, A, Q*, and *P* are 15.23 %, 4.12 %, 21.23 %, and 16.52 %, respectively. The computed participations of the *DQ, DP, AQ*, and *AP* are 1.49 %, 3.85 %, 1.57 %, and 1.66 %, respectively. The computed participations of the *D²*, *A²*, and *Q²* are 24.66 %, 1.76 %, and 7.38 %, respectively.

Table 7 presents ANOVA results for the *CIC* model with significant factors. The computed participations of the *D, A, Q*, and *P* are 11.37 %, 7.64 %, 20.97 %, and 11.69 %, respectively. The computed participations of the *DA, DQ, DP, AP*, and *QP* are 1.11 %, 2.76 %, 3.15 %, 3.11 %, and 2.06 %, respectively.

Table 3. *Operating parameters of the ANN models*

Level	Network type (*NT*)	Number of hidden neurons (*NN*)	Training function (*TF*)	Performance function (*PM*)	Transfer function (*TS*)	Number of hidden layers (*NL*)	Learning function (*LF*)
1	CFNN	15	TrainBFG	MSE	Logsig	1	LearnGDM
2	ELNN	16	TrainBR	MSEREG	Purelin	2	LearnGD
3	FFNN	17	TrainCGB	SSE	Tansig	3	-
4	LRNN	18	TrainCGF	-	-		-
5		19	TrainCGP	-	-		-
6		20	TrainGD	-	-		-
7		21	TrainGDM	-	-		-
8		22	TrainGDA	-	-		-
9		23	TrainGDX	-	-		-
10		24	TrainLM	-	-		-
11		25	TrainOSS	-	-		-
12		26	TrainR	-	-		-
13		27	TrainRP	-	-		-
14		28	TrainSCG	-	-		-

Table 4. *Training results for the developed ANN models*

No.	*NT*	*NN*	*TF*	*PM*	*TS*	*NL*	*LF*	*CYL* [%]	*CIC* [%]	*SR* [%]
1	CFNN	TrainBFG	16	MSE	Logsig	1	LearnGDM	9.81	8.43	9.46
14	ELNN	TrainOSS	20	MSEREG	Tansig	2	LearnGDM	8.64	7.93	8.78
84	CFNN	TrainLM	26	MSEREG	Tansig	2	LearnGDM	5.71	6.35	5.92
98	CFNN	TrainGDM	28	MSE	Purelin	3	LearnGD	5.43	7.32	5.66
124	LRNN	TrainSCG	18	SSE	Tansig	2	LearnGDM	6.81	7.32	5.81
149	FFNN	TrainLM	25	MSE	Logsig	3	LearnGDM	3.46	4.21	3.74
168	LRNN	TrainGDX	20	MSEREG	Tansig	2	LearnGD	6.38	9.56	6.58
182	ELNN	TrainSCG	22	MSE	Purelin	3	LearnGD	4.44	6.72	4.94
226	ELNN	TrainCGF	28	MSE	Tansig	1	LearnGD	6.74	6.89	6.42

Table 5. *Comparative errors for the burnishing responses*

No.	*CYL* [μm]			*CIC* [μm]			*SR* [μm]		
	Exp.	*ANN*	*Err.* [%]	*Exp.*	*ANN*	*Err.* [%]	*Exp.*	*ANN*	*Err.* [%]
27	29.36	29.69	-1.12	15.83	15.45	2.40	0.53	0.54	-1.89
28	29.29	28.98	1.06	14.27	14.58	-2.17	0.51	0.52	-1.96
29	34.12	34.53	-1.20	15.51	15.16	2.26	0.54	0.53	1.85
30	22.31	22.68	-1.66	10.66	10.35	2.91	0.36	0.37	-2.78
31	23.82	23.46	1.51	11.18	11.35	-1.52	0.41	0.42	-2.44
32	20.45	20.87	-2.05	9.22	9.39	-1.84	0.33	0.32	3.03
33	17.66	17.24	2.38	6.99	6.88	1.57	0.23	0.22	4.35
34	20.43	20.18	1.22	8.93	8.87	0.67	0.34	0.35	-2.94
35	16.84	16.59	1.48	7.85	7.97	-1.53	0.27	0.26	3.70
36	17.59	17.93	-1.93	8.78	8.61	1.94	0.31	0.32	-3.23
37	21.11	21.54	-2.04	9.24	9.17	0.76	0.21	0.22	-4.76
38	28.52	28.28	0.84	13.46	13.63	-1.26	0.44	0.43	2.27

Exp.: Experimental value; Err.: Error

The computed participations of the D^2, A^2, and Q^2 are 4.38 %, 22.78 %, and 7.69 %, respectively.

Table 8 presents ANOVA results for the *SR* model with significant factors. The computed participations of the *D, A, Q,* and *P* are 16.35 %, 6.73 %, 24.81 %, and 19.81 %, respectively. The computed participations of the D^2, A^2, Q^2, and P^2 are 5.38 %, 5.96 %, 3.84 %, and 7.31 %, respectively.
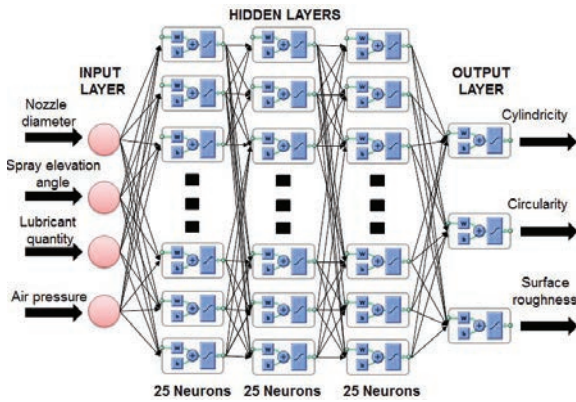
Fig. 5. *The architecture for the ANN models*

Table 6. *ANOVA results for CYL model*

So.	SS	MS	F value	P value
Mo.	1240.283	88.592	21.302	< 0.0001
D	188.895	188.895	45.420	< 0.0001
A	51.100	51.100	12.287	0.0013
Q	262.072	262.072	63.015	< 0.0001
P	204.895	204.895	49.267	< 0.0001
DQ	18.480	18.480	4.444	0.0069
DP	47.751	47.751	11.482	0.0006
AQ	19.472	19.472	4.682	0.0038
AP	20.589	20.589	4.951	0.0024
A2	305.854	305.854	73.542	< 0.0001
Q2	21.829	21.829	5.249	0.0021
P2	91.533	91.533	22.009	0.0003
Res.	49.907	4.159		
Cor.	1288.606			

$R^2 = 0.9652$

Mo.: Model; So.: Source; Res.: Residual; Cor.: Core total

Table 7. *ANOVA results for the CIC model*

So.	SS	MS	F value	P value
Mo.	302.390	21.599	20.952	< 0.0001
D	34.382	34.382	33.351	< 0.0001
A	23.103	23.103	22.410	< 0.0001
Q	63.411	63.411	61.511	< 0.0001
P	35.349	35.349	34.290	< 0.0001
DA	3.357	3.357	3.256	0.0084
DQ	8.346	8.346	8.096	0.0053
DP	9.525	9.525	9.240	0.0045
AP	9.404	9.404	9.122	0.0046
QP	6.229	6.229	6.043	0.0057
D2	13.245	13.245	12.848	0.0034
A2	68.884	68.884	66.820	< 0.0001
Q2	23.254	23.254	22.557	< 0.0001
Res.	12.337	1.031		
Cor.	314.727			

$R^2 = 0.9608$

Table 8. *ANOVA results for the SR model*

So.	SS	MS	F value	P value
Mo.	0.313	0.022	22.573	< 0.0001
D	0.051	0.051	51.671	< 0.0001
A	0.021	0.021	21.269	0.0003
Q	0.078	0.078	78.407	< 0.0001
P	0.062	0.062	62.605	< 0.0001
D2	0.017	0.017	17.002	0.0214
A2	0.019	0.019	18.835	0.0127
Q2	0.012	0.012	12.135	0.0833
P2	0.023	0.023	23.102	0.0037
Res.	0.012	0.001		
Cor.	0.324			

$R^2 = 0.9648$

3.3 Parametric Influences

Fig. 6 indicates that the burnishing responses decrease with increasing nozzle diameter. As the nozzle diameter increases, more droplets can penetrate the burnishing region. The friction at the interfaces decreases, and the cooling-lubrication efficiency increases; hence, low *CYL* and *CIC* values are obtained. Moreover, the burnished surface is efficiently wetted and protected with a higher amount of oil mist; hence, the *SR* decreases.

Fig. 7 presents the impact of the spray elevation angle on the *CYL*, *CIC*, and *SR*, respectively. For the *CYL* and *CIC* values, it can be stated that an increased spray elevation angle has a positive effect, but it turns negative at a certain amount (48 deg), while the turning point of 55 deg is applied for the *SR*. For low spray elevation angle, the penetration of the oil mist is ineffective, resulting in a lack of proper cooling-lubrication efficiency at the interfaces. An uneven deformation is produced along the axial and radial directions; hence, higher values of the *CYL* and *CIC* are obtained. In addition, high friction at the interfaces causes a higher surface roughness. At a higher spray elevation angle, the mist flow is accurately delivered into the machining region, which results in decreased friction; hence, the *CYL* and *CIC* decreases. Higher cooling-lubrication efficiency causes a reduction in surface roughness.

Fig. 8 presents the impact of the *Q* on the *CYL*, *CIC*, and *SR*, respectively. A higher lubricant quantity increases the number of oil droplets entering the contact zone between the roller-workpiece. The cooling-lubrication efficiency will be improved due to friction reduction, which causes uniform deformation; hence, the *CYL* and *CIC* significantly decrease. The burnished surface is wetted and protected due to the

penetration of a higher amount of the oil mist; hence, the *SR* decreases.

Figs. 9 indicates that the reductions in the burnishing responses are found with increased air pressure. Higher pressure causes a reduction in the droplet size of the oil mist, while the number of droplets and spraying velocity increase. The small diameter increases the penetration ability into the burnishing region; hence, the cooling-lubrication efficiency is enhanced. The friction between the
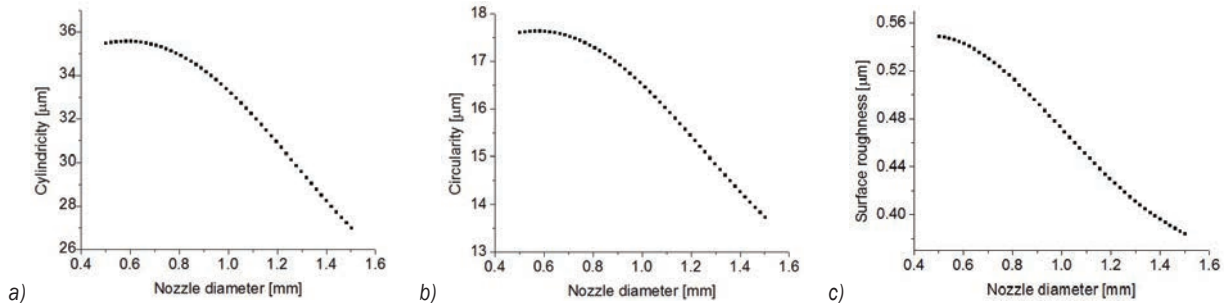
Fig. 6. *The impacts of the nozzle diameter on the burnishing responses; a) CYL and D, b) CIC and D, c) SR and D*
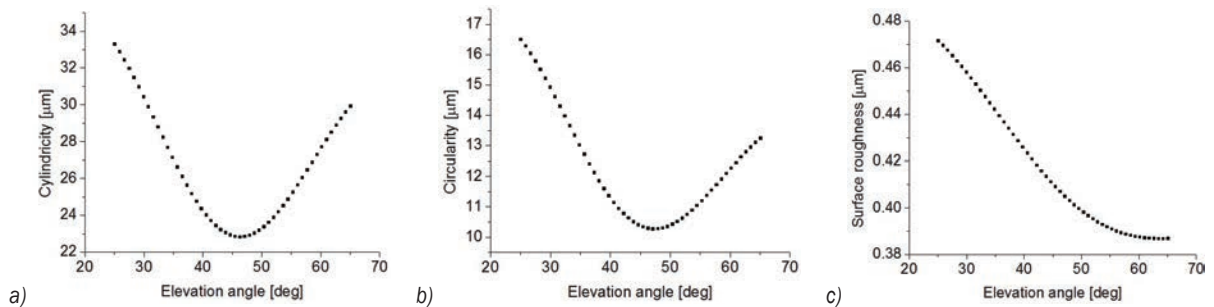
Fig. 7. *The impacts of the spray elevation angle on the burnishing responses; a) CIC and A, b) CIC and A, c) SR and A*
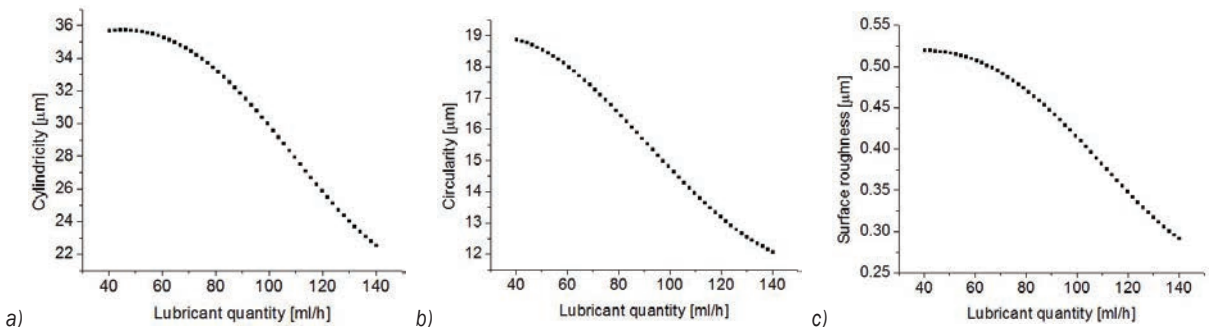
Fig. 8. *The impacts of the spray elevation angle on the burnishing responses; a) CYL and Q, b) CIC and Q, c) SR and Q*
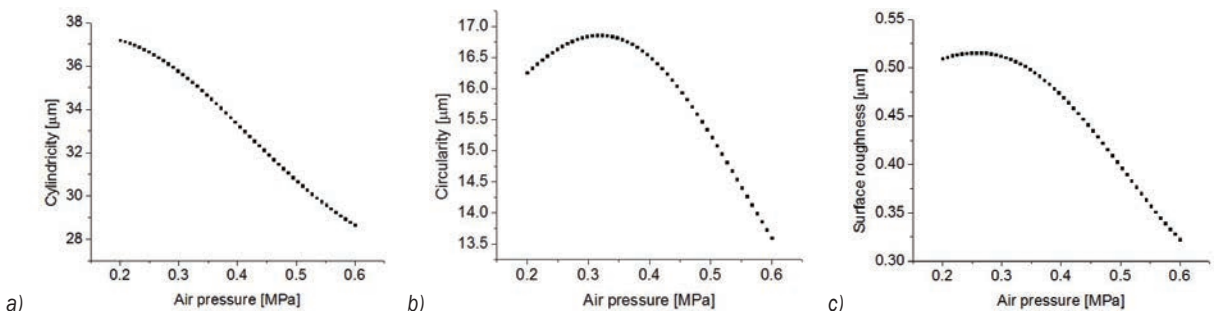
Fig. 9. *The impacts of the air pressure on the burnishing responses; a) CYL and P, b) CIC and P, c) SR and P*

Table 9. *Optimization results produced by the VCPSO*

Method	D [mm]	A [deg]	Q [ml/h]	P [MPa]	CYL [μm]	CIC [μm]	SR [μm]
Initial values	1.0	45	90	0.4	21.49	9.58	0.37
Optimal values	1.5	50	140	0.6	10.07	4.04	0.10
Improvements [%]					53.14	57.83	72.97

burnishing tool and workpiece decreases; hence, the burnishing responses reduce.

3.4 Optimization Results

The proportions of the first principal component is 92.7 %, followed by the second component (4.7 %) and the third component (2.6 %), respectively. The weight values are calculated using the squares of subsequent eigenvectors of the three components. The weight values of the *CYL*, *CIC*, and *SR* are 0.48, 0.34, and 0.18, respectively.

For the high-pressure bushing components, the predefined surface roughness of 0.1 μm is selected. The 3D plot produced with the aid of the VCPSO is shown in Fig. 10. As a result, the optimal values of the *D, A, Q,* and *P* are 1.5 mm, 50 deg, 140 ml/h, and 0.6 MPa, respectively, while the corresponding outcomes of the *CYL*, *CIC*, and *SR* are 10.07 μm, 4.04 μm, and 0.10 μm, respectively (Table 9). The improvements in the *CYL*, *CIC*, and *SR* are 53.14 %, 57.83 %, and 9.64 %, respectively, as compared to the initial values. The *CYL*, *CIC*, and *SR* are decreased by 85.74 %, 78.14 %, and 97.40 %, respectively, as compared to the pre-machined state.
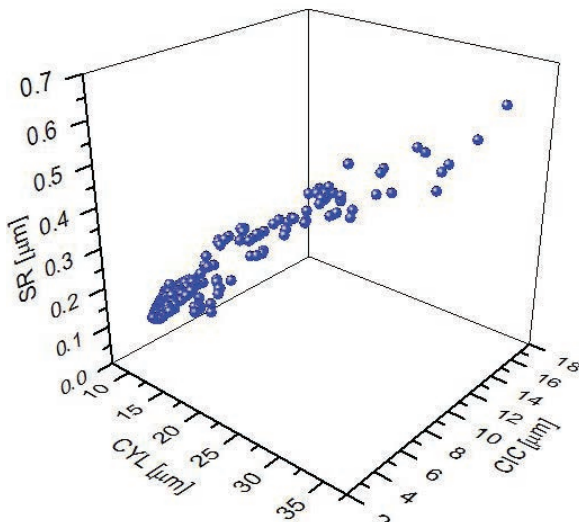
Fig. 10. *3D plots produced by the VCPSO*

4 CONCLUSIONS

In this study, a new MQL-based burnishing process has been proposed and optimized. Instead of traditional process parameters, the inputs considered were MQL operating parameters, including the nozzle diameter, the spray elevation angle, the lubricant quantity, and the pressure value of the compressed air. The quality indicators of the burnished hole, including the cylindricity and circularity, were then addressed and enhanced. The ANN approach was employed to develop the performance models instead of conventional regression models. A new evolutional algorithm entitled VCPSO algorithm was applied to find the optimal solution.

The academic contributions can be expressed as follows:

The proposed optimization technique comprising ANN, GRA, and VCPSO used in this study effectively solves the complex optimizing problems and determines optimal outcomes. The developed approach possesses various advantages, including low experimental costs, decreased human efforts, and easy application by means of Matlab software. The optimizing method can be extensively employed to solve the optimization issues for not only burnishing operations but also other machining processes.

The impacts of the MQL operating parameters (the nozzle diameter, the spray elevation angle, the lubricant quantity, and the pressure value of the compressed air) on the geometric deviations (cylindricity and circularity) and the surface roughness have been thoroughly analysed. The obtained knowledge can help machine operators deeply understand the physical insights in the developed burnishing operation.

The optimized findings can be applied in the burnishing operation to enhance the machining performances. Moreover, the obtained results revealed that the MQL system could be employed to enhance the machining quality of internal holes in various components.

The optimization issues addressing the cylindricity and circularity with a predefined constraint of the surface roughness are realistic and

reliable compared to the simultaneous optimizing three objectives.

The analysed outcomes of the current study can be effectively and efficiently utilized as significant references for future investigations and developing expert systems regarding MQL-assisted internal burnishing processes.

The industrial contributions can be expressed as follows.

In this work, an efficient burnishing operation under the MQL condition has been developed to enhance the machining quality of the internal surface. The successful implementation in the hardened steel is utilized to prove the effectiveness and potential application of the proposed burnishing process. The developed finishing operation can be effectively and efficiently applied to fabricate internal holes.

The constructed ANN models of the CYL, CIC, and SR were significant and accurate. The proposed correlations could be effectively applied to forecast the burnishing responses in industrial applications. The experimental costs and efforts can be saved with the aid of the proposed ANN models.

The 3D plots showing global relationships among machining performances can support machine operators in selecting the optimal values of the MQL operating factors, circularity, and cylindricity under various constraints of the surface roughness for different purposes.

The influences of the MQL system parameters on energy consumption and production costs have not been presented. A comprehensive optimization considering more objectives will be explored in future works.

5 ACKNOWLEDGEMENTS

6 REFERENCES

[1] Khan, M.M.A., Mithu, M.A.H., Dhar, N.R. (2009). Effects of minimum quantity lubrication on turning AISI 9310 alloy steel using vegetable oil-based cutting fluid. *Journal of Materials Processing Technology*, vol. 209, no. 15-16, p. 5573-5583, **DOI:10.1016/j.jmatprotec.2009.05.014**.

[2] Kývak, T., Şeker, U. (2015). Effect of cryogenic treatment applied to M42 HSS drills on the machinability of Ti-6Al-4V alloy. *Materials and Technology*, vol. 49, no. 6, p. 949-956, **DOI:10.17222 /mit.2014.283**.

[3] Goindi, G.S., Sarkar, P. (2017). Dry machining: a step towards sustainable machining-challenges and future directions. *Journal of Cleaner Production*, vol. 165, p. 1557-1571, **DOI:10.1016/j.jclep ro.2017.07.235**.

[4] Maruda, R.W., Krolczyk, G.M., Wojciechowski, S., Powalka, B. Klos, S., Szczotkarz, N. Matuszak, M. Khanna, M. (2020). Evaluation of turning with different cooling-lubricating techniques in terms of surface integrity and tribologic properties. *Tribology International*, vol. 148, art. ID, 106334, **DOI:10.1016/j.triboint.2020.10633**.

[5] Szczotkarz, N., Mrugalski, R., Maruda, R.W., Królczyk, G.M., Legutko, S., Leksycki, K. Dębowski, D., Pruncu, C.I. (2021). Cutting tool wear in turning 316L stainless steel in the conditions of minimized lubrication. *Tribology International*, vol. 156, art. ID 106813, **DOI:10.1016/j.triboint.2020.10681**.

[6] Mia, M., Bashir, M.A., Khan, M.A., Dhar, N.R. (2017). Optimization of MQL flow rate for minimum cutting force and surface roughness in end milling of hardened steel (HRC 40). *The International Journal of Advanced Manufacturing Technology*, vol. 89, p. 675-690, **DOI:10.1007/s00170-016-9080-8**.

[7] Jang, D., Jung, J., Seok, J. (2016). Modeling and parameter optimization for cutting energy reduction in MQL milling process. *International Journal of Precision Engineering and Manufacturing - Green Technology*, vol. 3, p. 5-12, **DOI:10.1007/s40684-016-0001-y**.

[8] Bayat, M., Abootorabi, M.M. (2021). Comparison of minimum quantity lubrication and wet milling based on energy consumption modeling. *Proceedings of the Institution of Mechanical Engineers, Part E: Journal of Process Mechanical Engineering*, vol. 235, no. 5, p. 1665-1675, **DOI:10.1177/09544089211014407**.

[9] Rajan, K.M., Kumar Sahoo, A., Chandra Routara, B., Kumar, R. (2021). Investigation on surface roughness, tool wear and cutting power in MQL turning of bio-medical Ti-6Al-4V ELI alloy with sustainability. *Proceedings of the Institution of Mechanical Engineers, Part E: Journal of Process Mechanical Engineering*, **DOI:10.1177/09544089211063712**.

[10] Sivaiah, P., Venkata Ajay kumar, G,, Lakshmi Narasimhamu, Balaji, N.S. (2021). Performance improvement of turning operation during processing of AISI 304 with novel textured tools under minimum quantity lubrication using hybrid optimization technique. *Materials and Manufacturing Processes*, **DOI:10.1080/10426914.2021.1967977**.

[11] Bhadoria, N.S., Bartarya, G. (2021). On the improvement in process performance of ceramic inserts during hard turning in MQL environment. *Materials and Manufacturing Processes*, vol. 37, no. 3, p. 283-293, **DOI:10.1080/10426914.2021.196 7978**.

[12] Zhang, D., Li, C., Zhang, Y., Jia, D, Zhang, X. (2015). Experimental research on the energy ratio coefficient and specific grinding energy in nanoparticle jet MQL grinding. *The International Journal of Advanced Manufacturing Technology*, vol. 78, p. 1275-1288, **DOI:10.1007/s00170-014-6722-6**.

[13] Ribeiro, F.S.F., Lopes, J.C., Garcia, M.V., de Moraes, D.L., da Silva, A.E., de Angelo Sanchez, L.E., de Aguiar, P.R., Bianchi, E.C. (2020). New knowledge about grinding using MQL simultaneous to cooled air and MQL combined to wheel cleaning jet technique. *The International Journal of*

Advanced Manufacturing Technology, vol. 109, p. 905-917, **DOI:10.1007/s00170-020-05721-z**.

[14] De Moraes, D.L., Garcia, M.V., Lopes, J.C., Fonteque Ribeiro, F.S., de Angelo Sanchez, L.E., Foschini, C.R., de Mello, H.J., Aguiar, P.R., Bianchi; E.C. (2019). Performance of SAE 52100 steel grinding using MQL technique with pure and diluted oil. *The International Journal of Advanced Manufacturing Technology*, vol. 105, p. 4211-4223, **DOI:10.1007/s00170-019-04582-5**.

[15] Faverjon, P., Rech, J., Valiorgue, F., Orset, M. (2015). Optimization of a drilling sequence under MQL to minimize the thermal distortion of a complex aluminum part. *Production Engineering*, vol. 9, p. 505-515, **DOI:10.1007/s11740-015-0614-y**.

[16] Chakravarthy, V.V.K., Rajmohan, T., Vijayan, D., Palanikumar, K. (2021). Sustainable drilling of Nano sic reinforced al matrix composites using MQL and cryogenic cooling for achieving the better surface integrity. *Silicon*, vol. 14, p. 1787-1805, **DOI:10.1007/s12633-021-00977-w**.

[17] Xu, J., Ji, M., Chen, M., Ren, F. (2019). Investigation of minimum quantity lubrication effects in drilling CFRP/Ti6Al4V stacks. *Materials and Manufacturing Processes*, vol. 34, p. 1401-1410, **DOI:10.1080/10426914.2019.1661431**.

[18] Sachin, B., Narendranath, S., Chakradhar, D. (2019). Selection of optimal process parameters in sustainable diamond burnishing of 17-4 PH stainless steel. *Journal of the Brazilian Society of Mechanical Sciences and Engineering*, vol. 41, p. 219, **DOI:10.1007/s40430-019-1726-7**.

[19] Sachin, B., Narendranath, S., Chakradhar, D. (2019). Effect of working parameters on the surface integrity in cryogenic diamond burnishing of 17-4 PH stainless steel with a novel diamond burnishing tool. *Journal of Manufacturing Processes*, vol. 38, p. 564-571, **DOI:10.1016/j.jmapro.2019.01.051**.

[20] Maruda, R.W., Krolczyk, G.M., Feldshtein, E., Pusavec, F., Szydlowski, M., Legutko, S., Sobczak-Kupiec, A. (2016). A study on droplets sizes, their distribution and heat exchange for minimum quantity cooling lubrication (MQCL). *International Journal of Machine Tools and Manufacture*, vol. 100, p. 81-92, **DOI:10.1016/j.ijmachtools.2015.10**.

[21] Maruda, R.W., Feldshtein, E., Legutko, S., Krolczyk, G.M. (2016). Analysis of contact phenomena and heat exchange in the cutting zone under minimum quantity cooling lubrication conditions. *Arabian Journal for Science and Engineering*, vol. 41, p. 661-668, **DOI:10.1007/s13369-015-1726-6**.

[22] Maruda, R.W., Feldshtein, E., Legutko, S., Krolczyk, G.M. (2015). Research on emulsion mist generation in the conditions of minimum quantity cooling lubrication (MQCL). *Technical Gazette - Tehnicki Vjesnik*, vol. 22, no. 5, p. 213-1218, **DOI:10.17559/TV-20140423221850**.

[23] Sampath, B., Myilsamy, S. (2021). Experimental investigation of a cryogenically cooled oxygenmist near-dry wire-cut electrical discharge machining process. *Strojniški vestnik - Journal of Mechanical Engineering*, vol. 67, no. 6, p. 322-330, **DOI:10.5545/sv-jme.2021.7161**.

[24] Nguyen, T.T., Le, T.M. (2021). Optimization of the internal roller burnishing process for energy reduction and surface properties. *Strojniški vestnik - Journal of Mechanical Engineering*, vol. 67, no. 4, p. 167-179, **DOI:10.5545/sv-jme.2021.7106**.

[25] Milčić, D., Alsammarraie, A., Madić, M., Krstić, V., Milčić, M. (2021). Predictions of friction coefficient in hydrodynamic journal bearing using artificial neural networks. *Strojniški vestnik - Journal of Mechanical Engineering*, vol. 67, no. 9, p. 411-420, **DOI:10.5545/sv-jme.2021.7230**.

[26] Rosel Solís, M., Dávalos Ramírez, J., Molina Salazar, J., Ruiz Ochoa, J., Gómez Roa, A. (2021). Optimization of running blade prosthetics utilizing crow search algorithm assisted by artificial neural networks. *Strojniški vestnik - Journal of Mechanical Engineering*, vol. 67, no. 3, p. 88-100, **DOI:10.5545/sv-jme.2020.6990**.

Optimization of FSW Processing Factors on Hardness for Dissimilar AA6061-T6 and AZ31B O Alloys

Karutha Pandian Vasantha Kumar* – Muthusamy Balasubramanian

Anna University, University College of Engineering Ramanathapuram, India

In modern industries, such as aerospace, automotive, marine and others, aluminium and magnesium alloys are the most frequently used non-ferrous materials. This paper discusses optimising processing factors to produce a high hardness of dissimilar Al/Mg alloys. The experiment was designed and conducted by varying input factors according to response surface methodology-central composite design. The regression model has been developed between the processing factor and hardness based on the results of the experiment. ANOVA is used to validate the regression model and to assess the percentage of each hardness factor's contribution. Finally, the desirability approach is used to optimise the processing factor for high hardness.
Keywords: dissimilar friction stir welding, aluminium alloy AA6061, magnesium alloys AZ31B, FSW, RSM, ANOVA

Highlights
- *Tool rotation and traverse speeds were important factors in determining the Vicker's hardness of the FSW welded Al/Mg alloy.*
- *High rotational speed and low transverse speed resulted in high hardness at the weld area.*
- *Rotational speed, traverse speed, and tilt angle have 28.24 %, 42.72 %, and 19.70 % influence on hardness, respectively.*
- *Traverse speed has a higher influence than other factors, such as rotational speed and tilt angle.*
- *The maximum Vicker's hardness value at the weld zone achieved by the experiment is 92 HV.*
- *The optimal setting for achieving high hardness (i.e., 92 HV) is at S = 1000 rpm, T = 30 mm/min and A = 2 deg at a desirability value of 0.98.*
- *The results of the confirmatory test show that hardness of FSWed Al/Mg Alloys is 92.5 HV and tensile strength is 182 MPa.*
- *The hardness of dissimilar FSWAl/Mg alloy is 92 HV, which is 85 % of the hardness of Al alloy and 110 % of hardness of Mg alloy.*

0 INTRODUCTION

Friction stir welding is advantageous for non-ferrous alloys, such as Al and Mg. Aluminium alloy 6061 offers various advantages, such as a high strength-mass ratio, excellent welding, and excellent corrosive endurance. Due to its high specific solidity and lower density, the use of magnesium AZ31B alloys in different industries has increased. However, existing methods for welding Al and Mg alloys have several disadvantages. Joining aluminium and magnesium alloys with FSW eliminates the majority of the difficulties associated with the current procedures.

Fig.1a shows FSW, a solid-state welding procedure that uses frictional heat generated by a rotating tool to weld materials. Weld quality in FSW is determined by process factors, tool design, and material properties of both the welding material and the tool [1] to [3]. Compared to the leaving side, high hardness in the weld zone is on the progressing side. Furthermore, in the welding of aluminium alloys, the traverse speed is the most important factor [4].

The profile of a tool probe and the ratio of a pin to shoulder diameter are the most crucial tool design factors in determining weld quality [5]. Malarvizhi

et al. [6] examined the impact of the diameter of the tool shoulder on the tensile, macrostructural, and microstructural characteristics of the Mg and Al alloys. Welding circumstances that lead to an adequate intermingling among different materials and the intermediary thermal input have been useful in attaining high-level weld attributes [7]. Verma et.al.[8] concluded that low rotational speed and high transverse speed resulted in poor hardness because there was insufficient time and frictional heat to form an atomic bond between the Al and Mg alloys.

Li et al. [9] investigated the effects of rotation and traverse speed on the mechanical and microstructure characteristics of the AZ31B-Magnesium alloy, concluding that high weld quality can be achieved with moderate heat input. A fine microstructure is observed in the weld zone, according to Singh et al. [10], indicating an increase in hardness in a welded joint. According to Devaiah et al. [11], tool rotation speed and traverse speeds were important factors in determining the mechanical properties of the FSW-welded Al alloy. Increased rotational speed or decreased traverse speed on FSW joints resulted in high hardness in the stir zone [10] and [13]. A suitable tool offset can improve joint quality by preventing defects, such as voids and tunnels,

*Corr. Author's Address: Department of Mechanical Engineering, Anna University, University College of Engineering Ramanathapuram Campus, Ramanathapuram, Tamilnadu, India, kpvasanthkumar@gmail.com
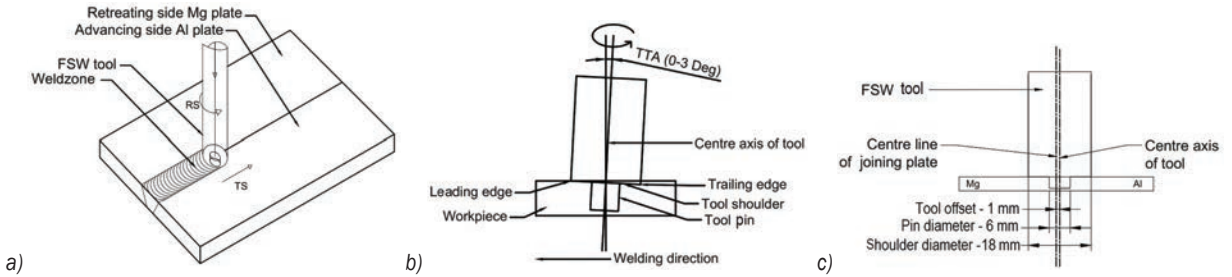
Fig. 1. *a) FSW process, b) tool tilt angle, and c) tool offset*

and reducing intermetallic compounds thickness to improve the interface bonding strength of the dissimilar weld during the friction stir welding (FSW) processes [14]. The response surface methodology (RSM) is a statistical technique for optimising multi-parameter and response optimization. RSM is widely used because of its simplicity and flexibility, as well as the ease with which individual factors and responses can be identified [15] and [16]. Most researchers concentrate solely on the tensile strength of welded material. The microstructures of welded aluminium and magnesium alloys have been analysed by various researchers [17] to [19].

In this paper, the effect of processing factors on the hardness of dissimilar FSW of Al/Mg alloys is analysed in depth. The Al alloy (AA6061-T6) and Mg alloy (AZ31B) are friction stir-welded in this research to evaluate the change in hardness at various process factors. The experiment architecture is developed using the RSM-central composite designed (CCD) technique by changing the process factor. The impact of each factor on the hardness of the FSW Al-Mg alloy has been investigated, and the desirability approach was used to optimise the process factor to achieve a high hardness of welded joints.

1 EXPERIMENTAL DETAILS

The FSW experiments were performed with the AA6061 aluminium alloy and the AZ31B magnesium alloy. The chemical components of welding plates are shown in Table 1. The surface of the aluminium and magnesium plate was cleaned with acetone, and the oxide on the surface was removed with a steel wire brush. The plate's dimensions are 75 mm × 50 mm × 4 mm. The tool pin profile and the ratio of shoulder and pin diameter are important design parameters in determining weld quality in the FSW procedure [5]. The FSW welding of Al and Mg plates were performed with a cylindrical pin profiled WC tool. Fig. 1c illustrates the FSW tool specification. *Ds/Dp*

= 3 (shoulder to pin diameter ratio) are constant. On the advancing side, the rotational tool was inserted at a 1 mm offset from the joining baseline, as shown in Fig. 1c. The diameter of the shoulder and pin of the tool are 18 mm and 6 mm, respectively, and the length of the probe is 3.8 mm. By varying processing factors, the experiments are designed using RSM – CCD techniques.

Table 1. *Chemical composition of workpieces*

Workpieces	AA6061-T6	AZ31B-O
Al	Balance	2.06
Mn	0.5	0.31
Zn	0.006	0.84
Fe	0.4	0.018
Cu	0.24	0.002
Cr	0.209	-
Si	0.67	<0.001
Ni	00.2	-
Mg	0.97	Balance
	Vicker's Hardness	
Vickers hardness	107 HV	83 HV

1.1 Identification of Processing Parameter

The primary processing factors are the tilt angle, traverse speed, axial force, and rotation speed. The processing factors and their range are shown in Table 2. The hardness of the weld is entirely determined by the amount of heat applied via various factors. Thermal input has a direct relationship with axial force and rotation speed. If the traverse speed is low, the friction between tool and workpiece is high, which increases the temperature at the nugget zone and vice versa. Eq. (1) expresses the relationship between the processing factor and the heat input.

$$Q_{Input} = \frac{2\pi}{3T} \times \mu \times F \times S \times R_s \times \eta, \qquad (1)$$

whereas T is traverse speed, S is rotation speed, F is an axial force, R_s is a radius of the shoulder, η is efficiency, and μ is coefficient of friction.

Table 2. *Processing factor and their range*

S. No.	Processing factor	Ranges
1	Rotation speed (S)	600 rpm to 1000 rpm
2	Traverse speed (T)	30 mm/min to 60 mm/min
3	Tool tilt angle (A)	0 deg to 2 deg

RSM-CCD techniques are used in this experiment to examine the impact of processing variable that influences the hardness at the welded zone. The RSM with desirability approach is employed to predict the best processing factors to achieve high hardness in welded areas. Tool tilt angle, traverse speed, and rotation speed all directly impact the hardness of FSW joints, which can be expressed in Eq. (2).

$$Y = f(S, T, A). \qquad (2)$$

This equation provides a mathematical model that shows how the joint hardness is related to the processing factor. In the select processing factor ranges given in Table 3, this model is developed to analyse the hardness of the welded joints.

Table 3. *Variation level of processing factor*

Processing factor	Levels		
	-1	0	1
S [rpm]	600	800	1000
T [mm/min]	30	45	60
A [deg]	0	1	2

2 RESULTS AND DISCUSSION

2.1 Results of Hardness Test

The fracture or crack occurs at the welded zone in the low hardness regions. In this present study, hardness evaluation near welded areas and processing factor optimization achieve better results. FSW experiments with multiple combinations of processing factors are performed. The specimen is prepared according to standards for the Vicker's hardness test are shown in Fig. 2. The hardness test carried out using Vicker's hardness tester in the weld area is shown in Fig. 3. Table 4 shows the hardness of the joints using Vicker's hardness testing under load.

The mathematical relationship is generated on the basis of the results to detect the effect of each factor

and their interaction on the hardness of the welded joint. Eq. (3) expresses the regression equation for the hardness of welded joint.

$$\begin{aligned}
HV = {} & 118.5 - 0.1011 \times S - 0.34 \times T + 7.24 \times A \\
& + 0.000068 \times S \times S - 0.00101 \times T \times T \\
& - 1.177 \times A \times A + 0.000221 \times S \times T \\
& + 0.00294 \times S \times A - 0.0842 \times T \times A.
\end{aligned} \qquad (3)$$

Table 4. *Experimental Results of hardness test*

S. No.	S [rpm]	T [mm/min]	A [deg]	Hardness [HV]
1	600	30	2	83
2	600	60	0	66
3	600	30	0	75.6
4	600	60	2	70.3
5	600	45	1	74.4
6	800	30	1	81.5
7	800	45	1	76.2
8	800	45	1	77
9	800	45	1	75.9
10	800	45	1	78.3
11	800	45	1	74.6
12	800	45	0	71.6
13	800	60	1	70
14	800	45	2	78
15	800	45	1	78
16	1000	45	1	83
17	1000	30	0	80.3
18	1000	60	2	80
19	1000	30	2	92
20	1000	60	0	75.3

Fig. 2. *Specimen after hardness test*
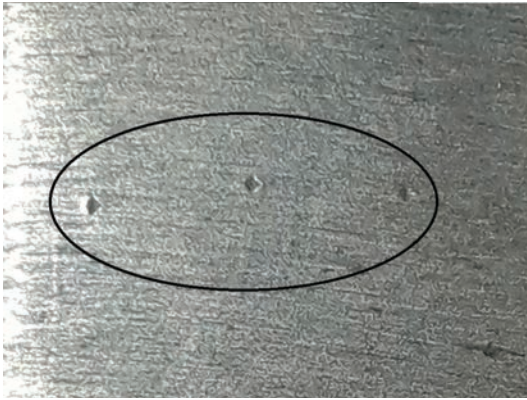
Fig. 3. *Hardness test carried out in the weld zone*

2.2 ANOVA Analysis

The effectiveness of the mathematical model is tested with ANOVA. The impact of each factor (rotational speed (RS), traverse speed (TS) and tool tilt angle (TTA)) on the response (hardness) is also determined [15] and [20]. The ANOVA table generated based on the experiment result with the help of Minitab software is represented in Table 5. To identify the contributions of each factor on response was evaluated using Eq. (4).

$$\% C = \frac{\sum SS_{Individual}}{\sum SS_{Total}} \times 100, \tag{4}$$

where C is the percentage contributed by the individual factor, $SS_{Individual}$ the sum of square contributed by the individual factor, and SS_{Total} the total of "sum of square" contributed by all factors. The F-value model of 45.32 implies that the model is meaningful. Very few chances of error in the f value due to noise. P-value lesser than 0.05 indicates that the terms in the model are significant. The F-value and P-values model, therefore, prove that the model is adequate and effective.

The model's fitness is based on the R^2 determination coefficient. Table 6 shows the corresponding statistical values for the developed model. The signal-to-noise ratio is sufficiently accurate. It is desirable to have a ratio above 4. The ANOVA results indicate that its result is valid. The percentages contribution from rotational speed, traverse speed and tilt angle are 28.24 %, 42.72 % and 19.70 %, respectively.

The residual analysis was performed to check the model's accuracy. The graphical method of checking that errors commonly occur in distribution is the normal probability plots [21]. Fig. 4 shows the normal probability plot. The residuals almost follow a straight line, which shows that the error follows the normal distribution.

The residual vs fitted chart is a scatter plot of residues on the *y*-axis and an estimated response is to detect the random distribution of residues on the *x*-axis and the constant variation of residues [22]. Fig. 5 shows the residual vs fitted value plot, the residues on both sides of the middle line are equally distributed.

Table 5. *ANOVA table*

Source	DF	SeqSS	AdjMS	%C	F-value	P-value
Model	9	589.60	65.51	97.61%	45.32	<0.001
Linear	3	547.66	182.55	90.66%	126.30	<0.001
S	1	170.57	170.57	28.24%	118.01	<0.001
T	1	258.06	258.06	42.72%	178.55	<0.001
A	1	119.03	119.03	19.70%	82.35	<0.001
Square	3	22.92	7.64	3.79%	5.28	0.02
$S \times S$	1	17.67	20.39	2.93%	14.10	0.00
$T \times T$	1	1.43	0.14	0.24%	0.10	0.76
$A \times A$	1	3.81	3.81	0.63%	2.64	0.14
2-Way Interaction	3	19.02	6.34	3.15%	4.39	0.03
$S \times T$	1	3.51	3.51	0.58%	2.43	0.15
$S \times A$	1	2.76	2.76	0.46%	1.91	0.20
$T \times A$	1	12.75	12.75	2.11%	8.82	0.01
Error	10	14.45	1.45	2.39%		
Lack-of-Fit	5	4.82	0.96	0.80%	0.50	0.77
Pure-Error	5	9.63	1.93	1.59%		
Total	19	604.05		100.00%		

From the residual analysis, the generated mathematical models are accurate, and they can be utilized to forecast the hardness of a welded joint within a given range of processing factors.
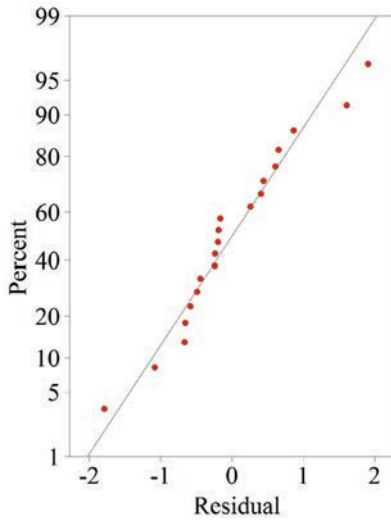
Fig. 4. *Normal probability plot*

Table 6. *Fit statistics*

R^2	R^2(adj)	R^2 (pred)
97.61 %	95.45 %	87.77 %
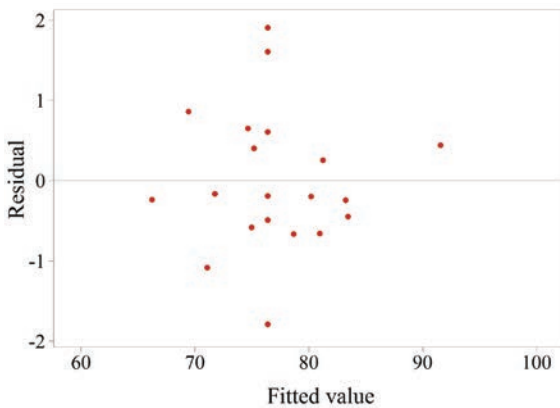
Fig. 5. *Residual vs. fitted value plot*

3 EFFECT OF FSW PARAMETER ON HARDNESS:

3.1 Effect of the Individual Parameter

The mean effect plots show that joint hardness is increased at a high tilt angle, high rotation, and low traversing speed at the welded region. When rotating speed and tilt angles are increased, the hardness at the welded zone improves. When the traverse speed is reduced, the joint hardness in the welded zone is increased. The primary cause of the hardness changes is the heat input. The mean effect plot has been created using Minitab software, which shows the change of hardness for input factors such as *RS*, *TS* and *TTA* is shown in Fig. 7. According to the ANOVA results, rotation speed, traverse speed, and tilt angle all contribute 28.24 %, 42.72 %, and 19.70%, respectively. Fig. 6. shows a pie chart that was created based on the ANOVA results. It shows that the traverse speed has a greater influence on the tool tilt angle than the rotation speed.
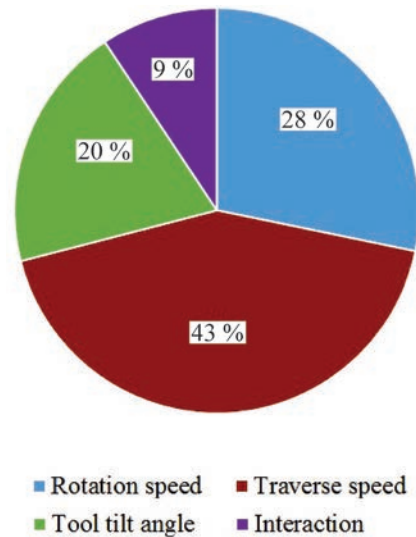
Fig. 6. *Influence of each factor on the hardness*

3.2 Effect of the Interaction Parameter

The traverse speed and tool tilt angle have high influences in a two-way interaction, as shown by interaction plots (Fig. 8). An interaction plot is created using Minitab software that shows the hardness variation in the interaction between processing factors. Compared to individual processing factors, the contribution of squared and interaction of processing factors is less in the ANOVA table. On hardness, the combined percentage contribution of squared and interaction processing factors is 9 %. The pareto chart depicts the graphical representation of each factor's influence and interaction. Processing factors, such as traverse speed, rotation speed and tool tilt angle, are denoted in this Pareto chart as factors *A*, *B* and *C*, respectively. Fig. 9 shows the pareto chart, which shows that factor *B* (traverse speed) has a more significant impact than the other factors and their interactions.
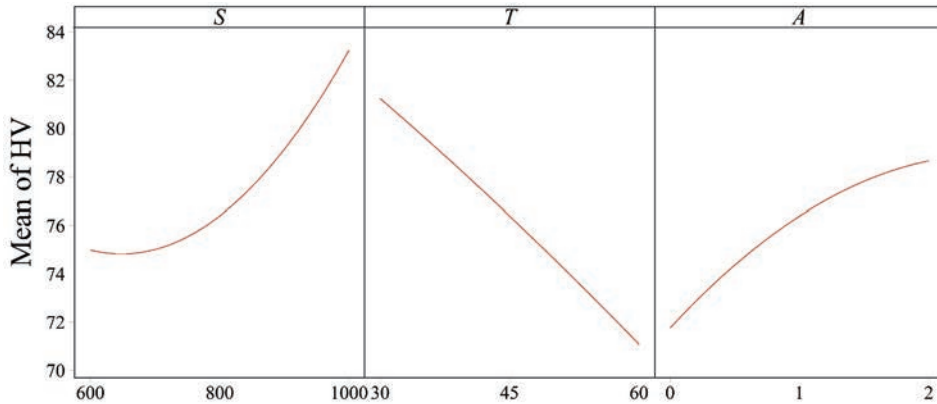
Fig. 7. *Mean effects of individual processing factors on hardness*
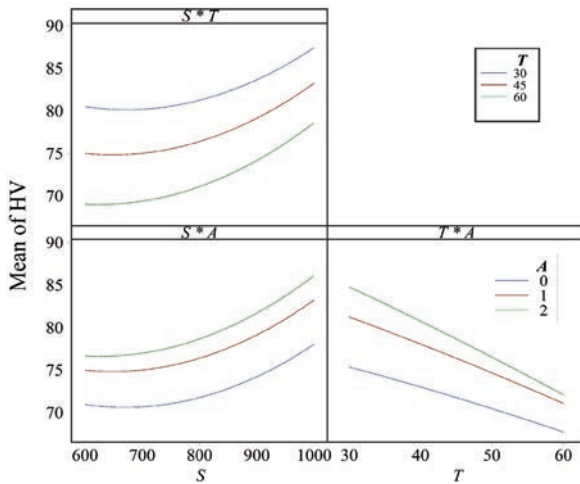
Fig. 8. *Interaction plot for Hardness vs. RS, TS, TTA*

Fig. 9. *Pareto chart*

desirability diagram is shown in Fig. 10, which shows the maximum hardness is 92 HV with a desirability of 0.98.
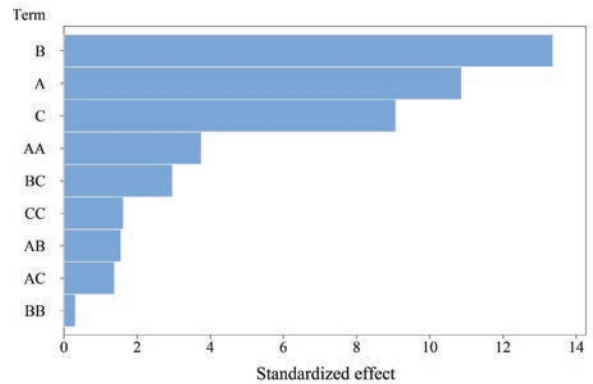
4 OPTIMISATION

The statistical techniques used to optimise processes are widespread overlaying contour plot method, constrained optimisation and desirability approach. The desirability approach is an optimization method that is simple and flexible [15]. The desirability approach is widely used to solve problems with several optimization responses. Desirability is a technique that converts the multiple outputs to measure performance in a set of dimensional quantities. The methodology used in this paper is desirability for optimisation of the factor of the FSW process. The FSW processing factor is set in range the rotational speed from 600 rpm to 1000 rpm, traverse speed (30 mm/min to 60 mm/min) and tool tilt angle (0 deg to 2 deg), and maximize output is set for hardness. From the results, it is observed that the optimum processing factor is *TTA*2 deg, *RS*1000 rpm and *TS*30 mm/min. The

5 VALIDATION OF RESULTS

The confirmatory test was performed with the optimum processing factors. The confirmatory test revealed that FSW Al/Mg Alloys have a hardness of 92.5 HV. The tensile strength of welded joint is tested with a universal testing machine (UTM), and the specimen is prepared according ASTM E8. The tensile strength of the welded joint is 182 MPa. The Vicker's hardness of aluminium alloy 6061 is 107 HV and magnesium alloy AZ31B is 83HV. The hardness of FSW is 92 HV, which is 85 % Al alloy and 110 % Mg alloy) is shown in the graph (Fig. 11).

Masoudian et al. [23] have analysed the effect of process parameters in dissimilarly welded aluminium AA6061 and magnesium AZ31B alloys without tool offset and predicted possible high hardness is around 89 HV. In this research paper, the highest hardness value achieved by tool offset is 92 HV, which is
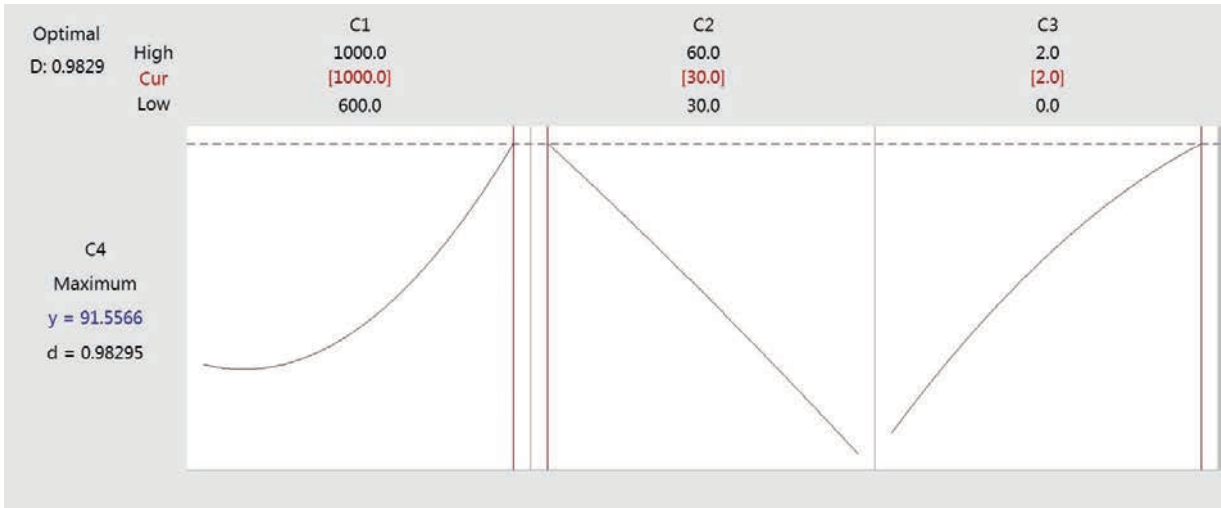
Fig. 10. *Desirability diagram*
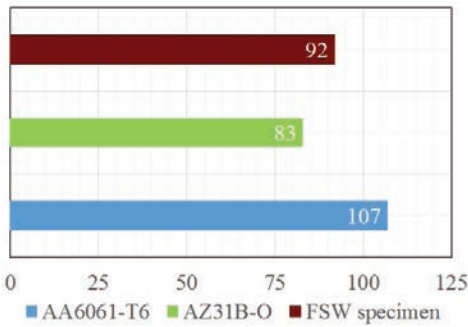
Fig. 11. *Vicker's hardness value of base metal and welded specimen*
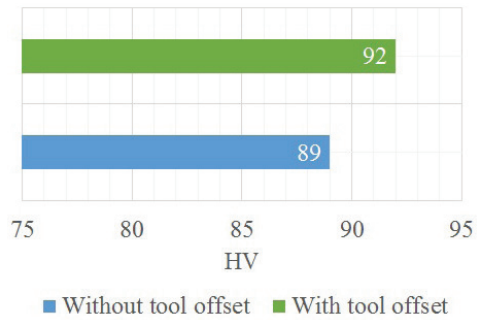
Fig. 12. *Vicker's hardness value of with and without tool offset*

slightly higher than the experiment done without tool offset as shown in Fig. 12.

Fig. 13 shows the image of an AA 6061-Mg AZ31B joint obtained at 1000 rpm and a 30 mm/min feed rate. Fig. 14 shows the multiple positions used for microstructural investigation after friction stir welding. This investigation provides for a better understanding of friction stir welding behaviour. We selected this condition because the heat generated at the spindle speed of 1000 rpm was sufficient to properly weld and produce the material flush. The aluminium-magnesium weld with a weld-line offset toward aluminium is the subject of this microstructure analysis.

Fig. 14 shows the microstructures generated for the points highlighted. A digital microscope is used to examine the defect-free weld connection. The microstructure of AA6061 and AZ31B's base materials comprises grains of different sizes and distributions.

Recrystallization occurs in Region A, which is referred as to as the nugget zone, as shown in Fig. 14a. Due to the high temperature caused by friction between the tool pin and workpieces, recrystallized Aluminium and Magnesium crystals can be visible in this region. Here the figure shows the aluminium and magnesium crystal distributed evenly.
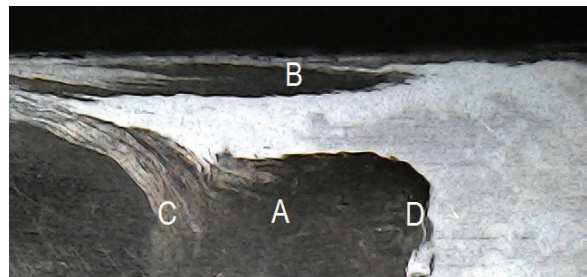
Fig. 13. *Friction stir welded AA6061-Mg AZ31B joint and positions of microstructure at the interfacial region*

A nugget zone at the shoulder is termed Region B is shown in Fig. 14b. Due to the high temperature
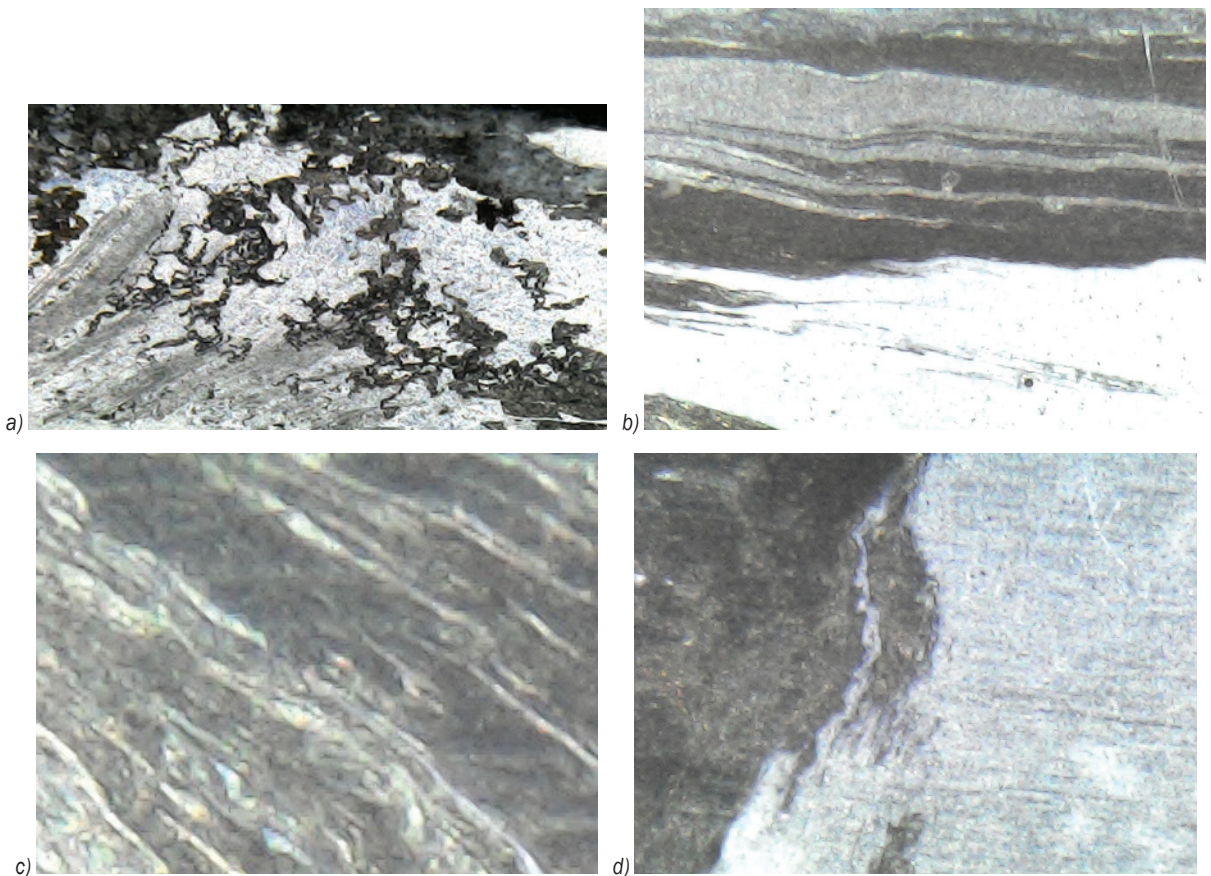
Fig. 14. *Microstructure at various zones of friction stir welded joint: a) nugget zone, b) nugget region near shoulder, c) thermo-mechanically affected zone in Al AA6061, and d) thermo-mechanically affected zone in Mg AZ31B*

caused by friction between the tool shoulder and the workpieces, recrystallized Al and Mg crystals may be visible in this region.

The thermomechanical affected zones of the AA6061 and AZ31B sides are Regions C and D shown in Fig. 14c and d. Due to limited strain deformation, this area exhibits elongated grains and a highly distorted structure. No recrystallization occurred in the region. Only plastic deformation occurs in this region.

6 CONCLUSION

The FSW experiment is performed by varying processing factors, and the hardness value of the welded zone was evaluated using the Vicker's hardness tester. The regression equation is established to examine the impact of each factor on the hardness. The adequacy of the regression equation is checked with the help of ANOVA analysis.

The generated model is adequate. The percentages contributed by each factor are $S = 28.24$ %, $T = 42.72$ % and $A = 19.70$ %, respectively. The traverse and rotational speed have a major impact on the hardness of dissimilar Al/Mg welded joints when compared to the tool tilt angle.

The hardness valve of welded joints increases when the RS and TTA increase. The reduction in traverse speed results in high hardness. The traverse speed has a greater effect on the hardness of dissimilarly welded Al/Mg joints than the rotational speed and tilt angle. The optimum processing factor is determined using the desirability approach.

The optimal setting for achieving high hardness (i.e., 92 HV) is at $S = 1000$ rpm, $T = 30$ mm/min and $A = 2$ deg at a desirability value of 0.98. The results of the confirmatory test show that the hardness of FSW Al/Mg alloys is 92.5 HV and tensile strength is 182 MPa.

The hardness of dissimilar FSW Al/Mg alloy is 92 HV, which is 85 % of the hardness of the Al alloy and 110 % of the hardness of the Mg alloy.

7 REFERENCE

[1] Thomas, W.M., Nicholas, E.D. (1997). Friction stir welding for the transportation industries. *Materials and Design*, vol. 18, no. 4-6, p. 269-273, **DOI:10.1016/S0261-3069(97)00062-9**.

[2] Mishra, R.S., Ma. Z.Y. (2005). Friction stir welding and processing. *Materials Science and Engineering: R: Reports*, vol. 50, no. 1-2, p. 1-78, **DOI:10.1016/j.mser.2005.07.001**.

[3] Nandan, R., DebRoy, T., Bhadeshia, H.K.D.H. (2008). Recent advances in friction-stir welding - Process, weldment structure and properties. *Progress in Materials Science*, vol. 53, no. 6, p. 980-1023, **DOI:10.1016/j.pmatsci.2008.05.001**.

[4] Rajakumar, S., Muralidharan, C., Balasubramanian, V. (2011). Predicting tensile strength, hardness and corrosion rate of friction stir welded AA6061-T6 aluminium alloy joints. *Materials and Design*, vol. 32, no. 5, p. 2878-2890, **DOI:10.1016/j.matdes.2010.12.025**.

[5] Elangovan, K., Balasubramanian, V. (2008). Influences of tool pin profile and tool shoulder diameter on the formation of friction stir processing zone in AA6061 aluminium alloy. *Materials and Design*, vol. 29 no. 2, p. 362-373, **DOI:10.1016/j.matdes.2007.01.030**.

[6] Malarvizhi, S., Balasubramanian, V. (2012). Influences of tool shoulder diameter to plate thickness ratio (D/T) on stir zone formation and tensile properties of friction stir welded dissimilar joints of AA6061 aluminum-AZ31B magnesium alloys. *Materials & Design*, vol. 40, p. 453-460, **DOI:10.1016/j.matdes.2012.04.008**.

[7] Sevvel, P., Jaiganesh, V. (2015). Effect of tool shoulder diameter to plate thickness ratio on mechanical properties and nugget zone characteristics during FSW of dissimilar Mg alloys. *Transactions of the Indian Institute of Metals*, vol. 68, no. 1, p. 41-46, **DOI:10.1007/s12666-015-0602-0**.

[8] Verma, J., Taiwade, R.V., Reddy, C., Khatirkar, R.K. (2018). Effect of friction stir welding process parameters on Mg-AZ31B/Al-AA6061 joints. *Materials and Manufacturing Processes*, vol. 33, no. 3, p. 308-314, **DOI:10.1080/10426914.2017.1291957**.

[9] Li, W.Y., Fu, T., Hütsch, L., Hilgert, J., Wang, F.F., dos Santos, J.F., Huber, N. (2014). Effects of tool rotational and welding speed on microstructure and mechanical properties of bobbin-tool friction-stir welded Mg AZ31. *Materials and Design*, vol. 64, p. 714-720, **DOI:10.1016/j.matdes.2014.07.023**.

[10] Singh. K., Singh. G, Singh. H. (2018). Investigation of microstructure and mechanical properties of friction stir welded AZ61 magnesium alloy joint. *Journal of Magnesium and Alloys*, vol. 6, no. 3, p. 292-298, **DOI:10.1016/j.jma.2018.05.004**.

[11] Devaiah, D., Kishore, K., Laxminarayana, P. (2018). Optimal FSW process parameters for dissimilar aluminium alloys (AA5083 and AA6061) using Taguchi Technique. *Materials Today: Proceedings*, vol. 5, no. 2, p. 4607-4614, **DOI:10.1016/j.matpr.2017.12.031**.

[12] Wang, W., Deng, D., Mao, Z., Tong, Y., Ran, Y. (2017). Influence of tool rotation rates on temperature profiles and mechanical properties of friction stir welded AZ31 magnesium alloy. *International Journal of Advanced Manufacturing Technology*, vol. 88, p. 2191-2200, **DOI:10.1007/ s00170-016-8918-4**.

[13] Barla, M., Jaidi, J. (2018). Influence of strain hardening behaviour in friction stir welded joints of aluminium-alloy plates. *Materials Today: Proceedings*, vol 5, no. 2, p. 3851-3860, **DOI:10.1016/j.matpr.2017.11.639**.

[14] Sahu; P.K., Pal, S., Pal, S.K., Jain, R. (2016). Influence of plate position, tool offset and tool rotational speed on mechanical properties and microstructures of dissimilar Al/Cu friction stir welding joints. *Journal of Materials Processing Technology*, vol. 235, p. 55-67, **DOI:10.1016/j.jmatprotec.2016.04.014**.

[15] Elatharasan, G., Senthil Kumar, V.S. (2012). Modelling and optimization of friction stir welding parameters for dissimilar aluminium alloys using RSM. P*rocedia Engineering*, vol. 38, p. 3477-3481, **DOI:10.1016/j.proeng.2012.06.401**.

[16] Elatharasan, G., Senthil Kumar, V.S. (2014). Corrosion analysis of friction stir-welded AA 7075 aluminium alloy. *Strojniški vestnik - Journal of Mechanical Engineering*, vol. 60, no. 1, p. 29-34, **DOI:10.5545/sv-jme.2012.711**.

[17] Bucki, T., Konieczny, M., Bolibruchova, D., Rzepa, S. (2021). Characterization of the AZ31/AW-6060 joint fabricated using compound casting with a zn interlayer at relatively low-temperature conditions. *Strojniški vestnik - Journal of Mechanical Engineering*, vol. 67, no. 7-8, p. 389-397, **DOI:10.5545/sv-jme.2021.7262**.

[18] Li, G., Jiang, W., Guan, F., Zhu, J., Zhang, Z., Fan, Z. (2020). Microstructure, mechanical properties and corrosion resistance of A356 aluminum/AZ91D magnesium bimetal prepared by a compound casting combined with a novel Ni-Cu composite interlayer. *Journal of Materials Processing Technology*, vol. 288, art. ID 116874, **DOI:10.1016/j.jmatprotec.2020.116874**.

[19] Li, G., Jiang, W., Yang, W., Jiang, Z., Guan, H., Jinaf, H., Fan, Z. (2019). New insights into the characterization and formation of the interface of A356/AZ91D bimetallic composites fabricated by compound casting. *Metallurgical and Materials Transactions A*, vol. 50, p. 1076-1090, **DOI:10.1007/s11661-018-5022-44**.

[20] Vasantha Kumar, K.P., Balasubramanian, M. (2020). Analyzing the effect of FSW process parameter on mechanical properties for a dissimilar aluminium AA6061 and magnesium AZ31B alloy. *Materials Today: Proceedings*, vol. 22, p. 2883-2889, **DOI:10.1016/j.matpr.2020.03.421**.

[21] Karthikeyan, R., Balasubramanian, V. (2010). Predictions of the optimized friction stir spot welding process parameters for joining AA2024 aluminum alloy using RSM. *International Journal of Advanced Manufacturing Technology*, vol. 51, p. 173-183, **DOI:10.1007/s00170-010-2618-2**.

[22] Palanivel. R, Koshy Mathews, P. (2012). Prediction and optimization of process parameter of friction stir welded AA5083-H111 aluminum alloy using response surface methodology. *Journal of Central South University*, vol. 19, p. 1-8, **DOI:10.1007/s11771-012-0964-y**.

[23] Masoudian. A., Tahaei, A., Shakiba A., Sharifianjazi, F., Mohandesi, J.A. (2014). Microstructure and mechanical properties of friction stir weld of dissimilar AZ31-O magnesium alloy to 6061-T6 aluminum alloy. *Transactions of Non-ferrous Metals Society of China*, vol. 24, no. 5, p. 1317-1322, **DOI:10.1016/S1003-6326(14)63194-0**.

Error Prediction for a Large Optical Mirror Processing Robot Based on Deep Learning

Zujin Jin[1] – Gang Cheng[1,2,*] – Shichang Xu[1] – Dunpeng Yuan[1]

[1] China University of Mining and Technology, School of Mechatronic Engineering, China
[2] Shangdong Zhongheng Optoelectronic Technology Co., China

Predicting the errors of a large optical mirror processing robot (LOMPR) is very important when studying a feedforward control error compensation strategy to improve the motion accuracy of the LOMPR. Therefore, an end trajectory error prediction model of a LOMPR based on a Bayesian optimized long short-term memory (BO-LSTM) was established. First, the batch size, number of hidden neurons and learning rate of LSTM were optimized using a Bayesian method. Then, the established prediction models were used to predict the errors in the X and Y directions of the spiral trajectory of the LOMPR, and the prediction results were compared with those of back-propagation (BP) neural network. The experimental results show that the training time of the BO-LSTM is reduced to 21.4 % and 15.2 %, respectively, in X and Y directions than that of the BP neural network. Moreover, the MSE, RMSE, and MAE of the prediction error in the X direction were reduced to 9.4 %, 30.5 %, and 31.8 %, respectively; the MSE, RMSE, and MAE of the prediction error in the Y direction were reduced to 9.6 %, 30.8 %, and 37.8 %, respectively. It is verified that the BO-LSTM prediction model could improve not only the accuracy of the end trajectory error prediction of the LOMPR but also the prediction efficiency, which provides a research basis for improving the surface accuracy of an optical mirror.
Keywords: Bayesian optimization, BO-LSTM, error prediction, optical mirror processing, hybrid manipulator, hyperparametrics

Highlights
- An end trajectory error prediction model based on a Bayesian optimized long short-term memory was established.
- The established prediction models were used to predict the spiral trajectory errors of the large optical mirror processing robot.
- The batch size, number of hidden neurons and learning rate of LSTM were optimized using a Bayesian method.
- The experimental results showed that the Bayesian optimized long short-term memory error prediction model could improve not only the accuracy of the end trajectory error prediction of the large optical mirror processing robot but also the prediction efficiency.

0 INTRODUCTION

With the development of the information age, modern optical systems are rapidly developing towards features including large aperture, high precision, high resolution, and high power. The requirements for LOMPS are also increasing. In order to realize the rapid development of modern optics and keep up with the development trends of advanced optical systems, LOMPS suitable for large-scale, aspherical, efficient and precise optical mirror processing have become a key technology to be solved urgently. Optical mirror processing includes four steps: rough grinding, milling forming, fine grinding, and polishing [1] and [2]. A fixed trajectory is used for the large optical mirror processing robot (LOMPR) in these four steps, with a grid trajectory, concentric circle trajectory, or spiral trajectory commonly used. The dynamic characteristics and control parameters of the LOMPR under a specific trajectory also show periodic changes [3] and [4]. Moreover, the processing of optical mirrors requires multiple iterations. The process of fabricating a large finished optical mirror from a blank can last from several days to several months [5] to [7]. Determining the long-term periodic movement

would aid in the mathematical statistical analysis of the non-linear error and predicting the direction and size of the error in the future, which will allow countermeasures to be taken in advance based on the predicted results [8] and [9]. Therefore, it is necessary to predict the trajectory error of the LOMPR based on the previous processing parameters to compensate for the uncertainty of the model and improve the surface accuracy and processing efficiency of the optical mirror [10] to [12].

Deep learning has rapidly developed in recent years, and many algorithms are suitable for non-linear fuzzy data processing. In fact, many scholars have applied deep learning and some intelligent analysis methods to the research field of traditional robots. Dai et al. applied a long short-term memory (LSTM) model to vehicle trajectory prediction [13]. Mici et al. [14] predicted the future instructions of a motor using a neural network structure to compensate for the delay error. To solve the trajectory tracking problem of a wheeled mobile robot under non-holonomic constraints and in the presence of model uncertainties, Mirzaeinejad et al. [15] derived and optimized a control law by minimizing a pointwise quadratic cost function for the predicted tracking errors of a wheeled mobile

robot. Wang et al. [16] proposed an adaptive Jacobian controller based on the prediction error to realize an adaptable kinematic and dynamic parameters driven by the prediction error. Las Casas et al. [17] established a fully connected feedforward artificial neural network with supervised learning to predict the error between the welding parameters of a welding robot. In order to predict the motion direction of a robot's end tool path in real time, Wang et al. [18] proposed that the robot's end tool path be guided by a human in off-line training of the LSTM to generate a trajectory predictor. Zhang et al. [19] predicted the torque of a six-degrees-of-freedom (6-DOF) cooperative robot based on a compensated cooperative robot dynamic model of an LSTM. Yang et al. [20] predicted the fault of a robot in a dynamic working state based on deep learning. Chebbi et al. [21] carried out a sensitivity analysis and positioning error limit prediction for a 3-DOF translational parallel robot. Zatout et al. [22] analysed the optimal output problem of a fuzzy logic controller for quadrotor attitude stabilisation through particle swarm optimization, bat algorithm and cuckoo search, and obtained the optimal performance of bat method. The above scholars applied deep learning to the fields of robot parameter optimization, trajectory prediction, fault diagnosis, and robot positioning, and achieved good results. However, few scholars have conducted relevant research on the error prediction of the end execution point of a hybrid robot with large load and coupling characteristics [23] to [25]. The trajectory error of the end execution point of a robot can be predicted using deep learning, which can provide feedforward compensation data for the servo control system.

However, not all deep learning models can be applied to different engineering fields. In order to cope with the characteristics of different engineering states and give deep learning algorithms a better fusion effect, many scholars have improved or optimized them. Li et al. [26] proposed an LSTM training method based on evolutionary attention and a competitive random search, which was applied to multivariate time series forecasting. Ahmad et al. [27] proposed a predictive control strategy for a four-degree-of-freedom half-car model in the presence of an active pneumatic surface to improve the attitude control ability of the vehicle. Ullah et al. [28] proposed model predictive control and H∞ control of a 6-DOF manipulator to improve the trajectory accuracy of the robot. Ali et al. [29] used a particle swarm optimization algorithm to optimize the gain of proportional-integral-derivative, the weighting matrices of linear quadratic regulator, and their ratio of contributions, so as to improve the

performance of the controller and obtain the accurate trajectory tracking ability of the controller. Bai et al. [30] analysed the performances of linear model predictive control, linear error model predictive control, non-linear model predictive control, and non-linear error model predictive control for mobile robot path tracking. To solve the time delay compensation problem for a non-linear teleoperation system, Shen et al. [31] proposed a motion prediction method based on a cascaded structure state observer. Tang et al. [32] predicted the wind speed range through particle swarm optimization of a deep learning network. Wang et al. [33] designed a high-performance detection model based on a superimposed LSTM to realize unmanned aerial vehicle real-time fault detection using a statistical threshold. Mei et al. [34] proposed a one-dimensional convolutional LSTM based on a vibration terrain classification method to learn both the spatial and temporal characteristics of dampened vibration signals. Wu et al. [35] predicted the health state of an aviation turbofan engine using a vanilla LSTM. Focusing on the unique attributes of the engineering field studied, the above scholars improved the existing deep learning algorithm, optimized the search algorithm, optimized the parameters, adjusted the deep learning framework to predict the data, and achieved ideal results. This background provides a reliable theoretical basis for predicting the error of the end execution point of a LOMPR using a Bayesian optimized long short-term memory (BO-LSTM).

Effectively predicting the end execution trajectory error of a LOMPR is very important when compensating for the robot's feedforward error and improving the surface accuracy of an optical mirror. This study established an end trajectory error prediction model for a LOMPR based on the Bayesian hyperparametric optimization of an LSTM. It can effectively predict the errors of the LOMPR in X and Y directions under different processing trajectories. Based on the above introduction, the structure of this paper is as follows. Section 1 introduces the structure of the LOMPR and the tool path of the robot when a computer controlled optical surfacing (CCOS) grinding system is used. Section 2 shows how the LSTM deep learning model was constructed based on Bayesian optimization. Section 3 shows how the effectiveness of the prediction model under the spiral trajectory was verified using an experimental analysis. Finally, Section 4 gives the conclusion of this paper.

1 LARGE OPTICAL MIRROR PROCESSING ROBOT

Based on the requirements of the optical mirror grinding process, the LOMPR needs at least five degrees of freedom (5-DOF). The LOMPR used in this study was a 5-DOF hybrid robot developed using a 3-DOF parallel (UPS+UP) manipulator combined with a 2-DOF serial manipulator. The topology of the LOMPR is shown in Fig. 1. Among them, the parallel part of the moving platform and fixed platform were connected by three UPS driven branches and one UP constrained branch. A world coordinate system (*O-XYZ*) was established, where *O* was the intersection of the horizontal axis of the fixed platform centre point and the vertical axis of the optical mirror. The *X*-axis pointed in the negative direction of point O_1, the *Z*-axis was vertically downward, and the *Y*-axis was determined according to the right-hand rule. The rotation axis of the primary rotary head was collinear with the UP branch chain, and the rotation axis of the secondary rotary head was perpendicular to the primary rotary head and parallel to the *Y*-axis. A reference coordinate system $O_{Ai}-x_{Ai}y_{Ai}z_{Ai}$ is established on the A$_i$, where O_{Ai} is the central hinge point of the Hooke hinge of the fixed platform, the z_{Ai}-axis is downward along the driving branch chain, the y_{Ai}-axis is perpendicular to the driving branch chain along the internal axis of Hooke hinge, and the x_{Ai}-axis follows the right-hand rule. The grinding tool used the CCOS grinding system. The CCOS grinding system consists of a rotating motor and a revolving motor. Among them, a pneumatic suspension device is designed above the rotation axis. When the LOMPR produces a position error in the *Z*-axis direction, it will push the suspension axis up and down to compensate for the error. Therefore, the error caused by the end trajectory of the LOMPR in the *Z*-axis direction will not affect the surface processing accuracy of the optical mirror.
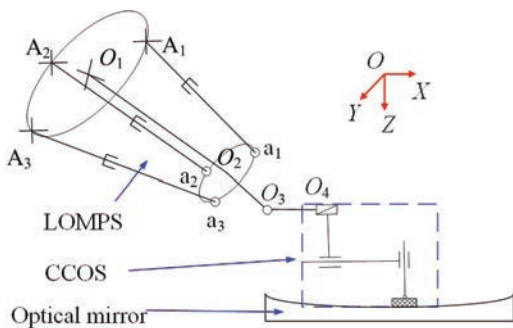
Fig. 1. *Topology of LOMPR*

The position error of the end execution point of the LOMPR is the result of the coupling of multiple influencing factors. The serial manipulator of the LOMPR has a relatively stable structural size, low motion speed and small stroke, so the error caused by the serial manipulator is very small. Here, the position error caused by the parallel module UPS branch chain is considered. The main factors affecting the error of a single UPS branch chain are the friction of moving pair, elastic deformation and servo system error, so the error of a single UPS branch chain can be expressed as:

$$\mathbf{e}_{li} = \mathbf{e}_{fi} + \mathbf{e}_{di} + \mathbf{e}_{ci} + \mathbf{e}_{oi} \quad i = 1, 2, 3, \qquad (1)$$

where $\mathbf{e}_{li}$ is the comprehensive error of UPS branch chain i, $\mathbf{e}_{fi}$ is the error caused by friction of moving pair, $\mathbf{e}_{di}$ is the error caused by force deformation of branch components, $\mathbf{e}_{ci}$ is the error of servo system, and $\mathbf{e}_{oi}$ is other errors.

The friction of the moving pair of the mechanism is mainly the friction generated during the movement of the Hooke hinge, composite ball hinge and ball screw of the UPS, resulting in insufficient driving force. Moreover, the posture of the mechanism in the motion space is different, the force state of each motion pair is also different, and the friction of the motion pair of the UPS is also related to its spatial posture. Therefore, the error caused by the friction of the moving pair can be expressed as:

$$\mathbf{e}_{fi} = F_{fi}(\mathbf{M}_{fi}, x, y, z), \qquad (2)$$

where F_{fi} is the conversion function between friction and position error of moving pair, $\mathbf{M}_{fi}$ is the friction of the moving pair, and (x, y, z) is the spatial coordinate of the LOMPR. The kinematic pair friction is analysed by introducing viscous friction based on the Coulomb friction model. So, the friction of the UPS can be obtained as:

$$\mathbf{M}_{fi} = \begin{bmatrix} M_{fix} \\ M_{fiy} \\ M_{fiz} \end{bmatrix} = \begin{bmatrix} M_{fix}^u + M_{fix}^s \\ + F_{fiz}^p \left(s\beta_i c\gamma_i + s\alpha_i c\beta_i s\gamma_i \right) \\ M_{fiy}^u + M_{fiy}^s \\ + F_{fiz}^p \left(s\beta_i s\gamma_i - s\alpha_i c\beta_i c\gamma_i \right) \\ M_{fiz}^p + M_{fiz}^s \end{bmatrix}, \qquad (3)$$

where M_{fix}, M_{fiy}, and M_{fiz} are the friction torque around x_{Ai}, y_{Ai} and z_{Ai} axis, respectively; M_{fix}^u, M_{fiy}^u, and M_{fiz}^u are the friction torque of Hooke hinge around x_{Ai}, y_{Ai}, and z_{Ai} axis, respectively; M_{fix}^s, M_{fiy}^s, and

M_{fiz}^s are the friction torque of composite ball hinge around x_{Ai}, y_{Ai}, and z_{Ai} axis, respectively; F_{fiz}^p is the friction force of the ball screw along the z_{Ai} axis; M_{fiz}^p is the friction torque of ball screw around z_{Ai} axis; α, β, and γ represents the RPY angle of the moving platform relative to the fixed platform.

The position error caused by the elastic deformation of UPS can be expressed by the kinematic constraints of a parallel mechanism under elastic deformation:

$$\mathbf{e}_{di} = \mathbf{J}_{di}\mathbf{q}_i, \tag{4}$$

where $\mathbf{J}_{di}$ is the kinematic constraint matrix, and $\mathbf{q}_i$ is the displacement and rotation of UPS under elastic deformation.

When the speed feedforward control model is adopted, the servo system error function of UPS can be expressed as:

$$e_{ci} = \lim_{s \to 0} \frac{\begin{bmatrix} Js^4 - \left[B + K_{pv}G_1K_T\left(1 - K_{sv}\right)\right]s^3 \\ + K_{pv2}G_1K_T\left(1 - K_{sv}\right)s^2 \end{bmatrix}}{b_1s^3 + b_2s^2 + b_3s + b_4} X_i(s), \tag{5}$$

where J is the load moment of inertia of the motor, B is viscous resistance, K_{pv} is the proportional coefficient of the speed loop, K_T is the torque coefficient, $K_{sv}s$ is the speed feedforward transfer function, $K_{pv2} = K_{pv}/\tau_v$, τ_v is the time constant of the velocity loop, X_i is the input signal, $b_1 = J$, $b_2 = B + K_{pv}G_iK_t$, $b_3 = K_{pv2}G_iK_t + K_pK_{pv}G_iK_t$, $b_4 = K_pK_{pv2}G_iK_t$.

2 BO-LSTM

2.1 LSTM Deep Neural Network

The LSTM was developed using recurrent neural networks (RNNs) and is mainly used to solve the problem of long-term data dependence in RNNs. An LSTM can remember the information and its correlation over a long period of time and can easily be recalled so that the information does not decay. An LSTM consists of three steps: a state forward calculation, error back propagation, and a weight update.

1) State forward calculation

The input value of an LSTM is network input value $\mathbf{X}_t$ at the current time and network state $\mathbf{S}_{t-1}$ at the previous time. These flow through forgetting gate $\mathbf{F}$, input gate $\mathbf{I}$, hiding unit $\mathbf{H}$, and output gate $\mathbf{O}$.

(1) Forgetting gate

$$\mathbf{F}_t = g\left(\mathbf{U}^F\mathbf{X}_t + \mathbf{W}^F\mathbf{S}_{t-1} + \mathbf{b}^F\right), \tag{6}$$

where $\mathbf{U}^F$, $\mathbf{W}^F$, and $\mathbf{b}^F$ represent the input connection matrix, feedback connection matrix, and offset term of the forgetting gate, respectively, g is the sigmoid function.

(2) Input gate

$$\mathbf{I}_t = g\left(\mathbf{U}^I\mathbf{X}_t + \mathbf{W}^I\mathbf{S}_{t-1} + \mathbf{b}^I\right), \tag{7}$$

where $\mathbf{U}^I$, $\mathbf{W}^I$, and $\mathbf{b}^I$ represent the input connection matrix, feedback connection matrix, and offset term of the input gate, respectively.

(3) Hiding unit

$$\mathbf{H}_t = \tanh\left(\mathbf{U}^H\mathbf{X}_t + \mathbf{W}^H\mathbf{S}_{t-1} + \mathbf{b}^H\right), \tag{8}$$

where $\mathbf{U}^H$, $\mathbf{W}^H$, and $\mathbf{b}^H$ represent the input connection matrix, feedback connection matrix, and offset term of the hiding gate, respectively.

(4) Storage element status update

$$\mathbf{C}_t = \mathbf{F}_t\mathbf{C}_{t-1} + \mathbf{I}_t\mathbf{H}_t. \tag{9}$$

(5) Output gate

$$\mathbf{O}_t = g\left(\mathbf{U}^O\mathbf{X}_t + \mathbf{W}^O\mathbf{S}_{t-1} + \mathbf{b}^O\right), \tag{10}$$

where $\mathbf{U}^O$, $\mathbf{W}^O$, and $\mathbf{b}^O$ represent the input connection matrix, feedback connection matrix, and offset term of the output gate, respectively.

(6) LSTM hidden layer output

The information, $\mathbf{C}_t$, of the storage element is multiplied by the result of the tanh transfer function and the output gate to obtain the LSTM hidden layer output.

$$\mathbf{S}_t = \mathbf{O}_t \tanh\left(\mathbf{C}_t\right). \tag{11}$$

(7) Network output

The hidden layer output of the LSTM is sent to the softmax output layer through connection matrix $\mathbf{V}$ to obtain the actual output of the network.

$$\widehat{\mathbf{Y}}_t = f\left(\mathbf{V}\mathbf{S}_t + \mathbf{b}\right). \tag{12}$$

2) Error back propagation

Based on the actual network output obtained by the forward calculation, the error function can be defined as follows:

$$\mathbf{E} = \sum_t \frac{1}{2}\left(\widehat{\mathbf{Y}}_t - \mathbf{Y}_t\right)^2, \tag{13}$$

where $\mathbf{Y}_t$ is the annotation signal from the data. For time step t, the corresponding error is found as follows:

$$e_t = \frac{\partial \mathbf{E}}{\partial \mathbf{S}_t} = \frac{\partial \mathbf{E}_{t+1}}{\partial \mathbf{S}_t} + \frac{\partial \mathbf{E}_t}{\partial \mathbf{S}_t}. \tag{14}$$

In other words, the downstream error at a certain time, t, can be divided into two parts: the error of the backflow in the later time step, $t+1$, and the error of the same time step, t. The errors of these two parts are expressed as follows:

$$\begin{cases} \dfrac{\partial \mathbf{E}_t}{\partial \mathbf{S}_t} = \left(\widehat{\mathbf{Y}}_t - \mathbf{Y}_t \right) \dot{\mathbf{f}} \left(\mathbf{VS}_t + \mathbf{b} \right) \mathbf{V} \\ \dfrac{\partial \mathbf{E}_{t+1}}{\partial \mathbf{S}_t} = \delta_{t+1}^O \mathbf{W}^O + \delta_{t+1}^F \mathbf{W}^F \\ \qquad\qquad + \delta_{t+1}^I \mathbf{W}^I + \delta_{t+1}^H \mathbf{W}^H \end{cases}, \tag{15}$$

where δ is the neural node error. The expressions of the transfer function sigmoid and hyperbolic tangent function are as follows:

$$\begin{cases} y = \dfrac{1}{1+e^{-z}} \\ y = \tanh(z) = \dfrac{e^z - e^{-z}}{e^z + e^{-z}} \end{cases}. \tag{16}$$

Further calculation shows that the errors are as follows:

$$\begin{cases} \delta_{t+1}^O = e_{t+1} \tanh(\mathbf{C}_{t+1}) \mathbf{O}_{t+1} (1 - \mathbf{O}_{t+1}) \\ \delta_{t+1}^F = e_{t+1} \mathbf{O}_{t+1} (1 - \tanh^2(\mathbf{C}_{t+1})) \mathbf{C}_t \mathbf{F}_{t+1} (1 - \mathbf{F}_{t+1}) \\ \delta_{t+1}^I = e_{t+1} \mathbf{O}_{t+1} (1 - \tanh^2(\mathbf{C}_{t+1})) \mathbf{H}_{t+1} \mathbf{I}_{t+1} (1 - \mathbf{I}_{t+1}) \\ \delta_{t+1}^H = e_{t+1} \mathbf{O}_{t+1} (1 - \tanh^2(\mathbf{C}_{t+1})) \mathbf{I}_{t+1} (1 - \mathbf{H}_{t+1}) \end{cases}. \tag{17}$$

3) Weight update

Based on the errors of the forgetting gate, input gate, and output gate in each time step, the connection weight parameters associated with these components can be updated and combined with the output values of each neuron obtained in the forward calculation.

The formula for updating the connection parameters of a forgetting gate is as follows:

$$\begin{cases} \mathbf{U}_{n+1}^F = \mathbf{U}_n^F - \beta \sum_t \delta_t^F \mathbf{X}_t \\ \mathbf{W}_{n+1}^F = \mathbf{W}_n^F - \beta \sum_t \delta_t^F \mathbf{S}_{t-1} \\ \mathbf{V}_{n+1}^F = \mathbf{V}_n^F - \beta \sum_t \delta_t^F \mathbf{S}_{t-1} \\ \mathbf{b}_{n+1}^F = \mathbf{b}_n^F - \beta \sum_t \delta_t^F \end{cases}, \tag{18}$$

where β is the learning rate, and n is the number of iterations.

The formula for updating the connection parameters of the input gate is as follows:

$$\begin{cases} \mathbf{U}_{n+1}^I = \mathbf{U}_n^I - \beta \sum_t \delta_t^I \mathbf{X}_t \\ \mathbf{W}_{n+1}^I = \mathbf{W}_n^I - \beta \sum_t \delta_t^I \mathbf{S}_{t-1} \\ \mathbf{V}_{n+1}^I = \mathbf{V}_n^I - \beta \sum_t \delta_t^I \mathbf{S}_{t-1} \\ \mathbf{b}_{n+1}^I = \mathbf{b}_n^I - \beta \sum_t \delta_t^I \end{cases}. \tag{19}$$

The formula for updating the connection parameters of the hidden layer is as follows:

$$\begin{cases} \mathbf{U}_{n+1}^H = \mathbf{U}_n^H - \beta \sum_t \delta_t^H \mathbf{X}_t \\ \mathbf{W}_{n+1}^H = \mathbf{W}_n^H - \beta \sum_t \delta_t^H \mathbf{S}_{t-1} \\ \mathbf{V}_{n+1}^H = \mathbf{V}_n^H - \beta \sum_t \delta_t^H \mathbf{S}_{t-1} \\ \mathbf{b}_{n+1}^H = \mathbf{b}_n^H - \beta \sum_t \delta_t^H \end{cases}. \tag{20}$$

The formula for updating the connection parameters of the output gate is as follows:

$$\begin{cases} \mathbf{U}_{n+1}^O = \mathbf{U}_n^O - \beta \sum_t \delta_t^O \mathbf{X}_t \\ \mathbf{W}_{n+1}^O = \mathbf{W}_n^O - \beta \sum_t \delta_t^O \mathbf{S}_{t-1} \\ \mathbf{V}_{n+1}^O = \mathbf{V}_n^O - \beta \sum_t \delta_t^O \mathbf{S}_{t-1} \\ \mathbf{b}_{n+1}^O = \mathbf{b}_n^O - \beta \sum_t \delta_t^O \end{cases}. \tag{21}$$

2.2 Bayesian Optimized Hyperparameters

During the training of the LSTM, there are many hyperparameters in the model, including the data length, number of iterations, learning rate, number of hidden neural units, and forgetting coefficient, which can be set at will. Appropriate super parameters are vital to improving the performance of the model. Bayesian optimization can not only set continuous hyperparameter values but also has a high search efficiency and accuracy.

Bayesian optimization uses the approximate global optimization algorithm to find the hyperparametric combination that minimizes the objective function:

$$p(f|D) = \frac{p(D|f)p(f)}{p(D)}, \tag{22}$$

where f represents the objective function; $D = \{(x_1, y_1), (x_1, y_1), \dots (x_n, y_n)\}$ is the data set; $p(f|D)$ and $p(f)$

are the a posteriori probability and a priori probability, respectively; $p(D|f)$ is the likelihood distribution of y; and $p(D)$ is the boundary likelihood distribution of f.

Assuming a set of super parameter combinations, $\mathbf{X} = (x_1, x_2, …, x_n)$, each super parameter is evaluated, and the evaluation result is $f(x_n)$. Then, the optimal hyperparameter is found as follows:

$$x^* = \arg \min_{x \in X} f(x). \qquad (23)$$

1) Probabilistic agent model

The probability agent model adopts a Gaussian process, and the Gaussian distribution can be expressed as follows:

$$f(x) \sim GP(\mu(x), k(x,x)), \qquad (24)$$

where $\mu(x)$ is the mean function, $k(x,x)$ is the positive definite covariance function, and $f(x)$ is the average absolute error.

According to the nature of the Gaussian process, f_t and f_{t+1} obey a joint Gaussian distribution:

$$\begin{bmatrix} f_{1:t} \\ f_{t+1} \end{bmatrix} \sim N\left(0, \begin{bmatrix} k & k \\ k^{\mathrm{T}} & k(x_{t+1}, x_t) \end{bmatrix} \right), \qquad (25)$$

where

$$\begin{cases} k = \left[k(x_{t+1}, x_1) \cdot k(x_{t+1}, x_2) \cdots k(x_{t+1}, x_t) \right] \\ P(f_{t+1}|D_{1:t}, x_{t+1}) = N(\mu_t(x_{t+1}), \sigma_t^2(x_{t+1})) \\ \mu_t(x_{t+1}) = k^{\mathrm{T}} K^{-1} f_{1:t} \\ \sigma_t^2(x_{t+1}) = k(x_{t+1}, x_{t+1}) - k^{\mathrm{T}} K^{-1} k \end{cases}, \quad (26)$$

where K is the covariance matrix,

$$K = \begin{bmatrix} k(x_1, x_1) & \cdots & k(x_1, x_t) \\ \vdots & \ddots & \vdots \\ k(x_t, x_1) & \cdots & k(x_t, x_t) \end{bmatrix}.$$

2) Acquisition function

The acquisition function can prevent the Bayesian optimization from falling into a local optimal solution. The excepted improvement (EI) acquisition function can find the next sample point with the greatest improvement expectation. The EI sampling function is as follows:

$$EI(x) = \begin{cases} \mu(x) - f(x^+)\Phi(Z) & \sigma(x) > 0 \\ +\sigma(x)\phi(Z) & \\ 0 & \sigma(x) \leq 0 \end{cases}, \quad (27)$$

where Φ is the probability density, φ is the standard normal distribution function, and $f(x^+)$ is the existing maximum. In addition, the following is true:

$$Z = \frac{\mu(x) - f(x^+)}{\sigma(x)}. \qquad (28)$$

Then, the flow of the BO-LSTM is shown in Fig. 2.
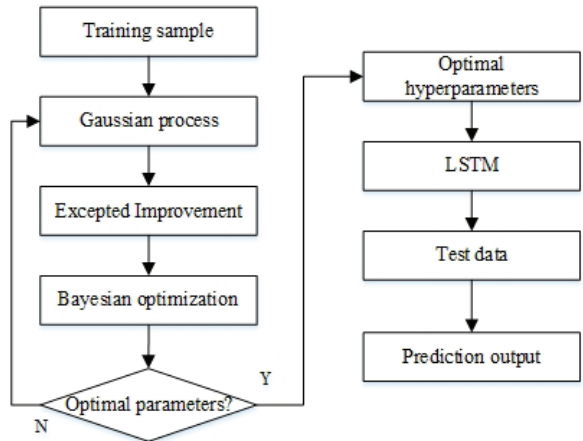
Fig. 2. *Flow of BO-LSTM*

3 EXPERIMENTAL ANALYSIS

The prototype of the LOMPR is shown in Fig. 3. In mirror processing, grid trajectory, concentric circle trajectory, and spiral trajectory are commonly used. The curvature of spiral trajectory constantly changes, which severely tests the dynamic characteristics of LOMPR, and the end trajectory error generated by the processing robot is also relatively large. Therefore, the spiral trajectory is used as a representative to predict the error in the X and Y directions of the end trajectory
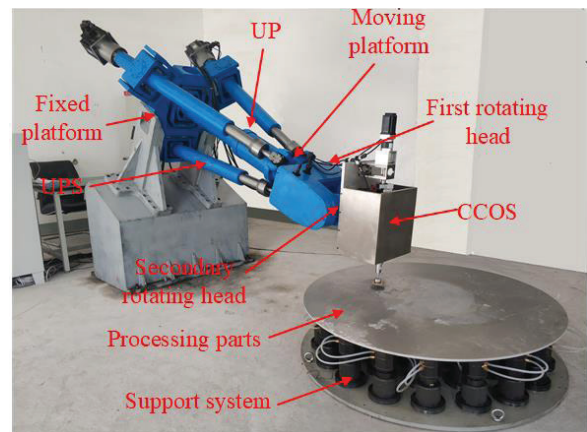
Fig. 3. *Prototype of LOMPR*
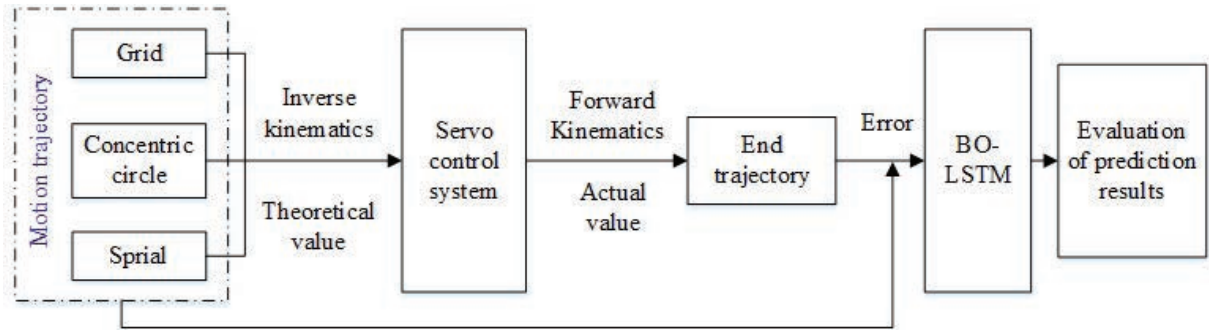
Fig. 4. *Technical route of error prediction*

of the LOMPR. Because the optical mirror needs to complete an iterative cycle before surface detection, it is impossible to collect the error of the mirror surface in real time for prediction. Therefore, the training data used are the end execution point position parameters calculated from the collected motion branch chain parameters into the forward kinematics model. Then the actual trajectory error collected from the experimental mirror is compared with the prediction results. On the one hand, it can verify the effectiveness of the BO-LSTM prediction model; on the other hand, it can verify the accuracy of the forward kinematics model. The technical route is shown in Fig. 4.

The experiment was based on the deep learning framework Keras library written in the Python language to complete the BO-LSTM model construction, data loading, training, and testing. Firstly, the data is pre-processed, including time stitching, missing data processing, abnormal data processing and data normalization. In the process of data prediction, the learning rate, batch capacity, and the number of hidden neurons directly affected the convergence speed and prediction accuracy of the model. Then, the above hyperparameters were optimized, and the appropriate parameters were input into the model for training. In order to compare the effectiveness of this hyperparametric optimization, a set of default values were used based on engineering experience, including a batch size of 1500, 35 hidden neurons, and a learning rate of 0.01. Considering the influence of the hyperparameters on the model performance and the interaction between hyperparameters, the value range of the batch size was set at (200, 600, 1000, 1500), the number of hidden neurons was (5, 15, 35, 50), the learning rate was (0.1, 0.01, 0.001), the optimizer was "Adam," and the activation function was "Relu".

Bayesian optimization was used to search the above hyperparameters, and the following optimal combination of hyperparameters was obtained: a batch size of 1000, 15 hidden neurons, and a learning rate of 0.001. The experimental data were imported into the established LSTM error prediction model using 90 % as training data samples and 10 % as test samples. The end execution point errors of the optical mirror machining robot under different trajectories were then predicted using the BO-LSTM. In order to verify the effectiveness of the BO-LSTM model in the prediction of optical mirror processing trajectory error, the BP neural network prediction model is used for prediction and analysis, and the prediction results are compared with those of BO-LSTM.

The trajectory equation of the robot during spiral processing is as follows:

$$\begin{cases} X = 20t_h \cos\left(\dfrac{\pi}{2}t_h + \dfrac{\pi}{2}\right) \\ Y = 20t_h \sin\left(\dfrac{\pi}{2}t_h + \dfrac{\pi}{2}\right) \quad t_h = 0:10. \\ Z = 0 \times t_h + 1097 \end{cases} \quad (29)$$

The LOMPR was controlled to process continuously, the motion period is 40 s and the sampling period is 40 ms. And the motion data of each rotating axis were collected, and the trajectory error of the end execution point was calculated. According to the collected data, the prediction results of BO-LSTM prediction model and BP neural network prediction model are shown in Fig. 5.

The data collected during the experiment and the trajectory error prediction results of the spiral trajectory in the X and Y directions are shown in Fig. 5. As the spiral trajectory is a trajectory with gradually increasing curvature, the errors of the LOMPR in the X and Y directions accumulates, resulting in the trajectory error in the X and Y directions gradually increasing amplitude and periodically changing in the form of a sinusoidal function curve. The prediction parameters of the BP neural network are shown in
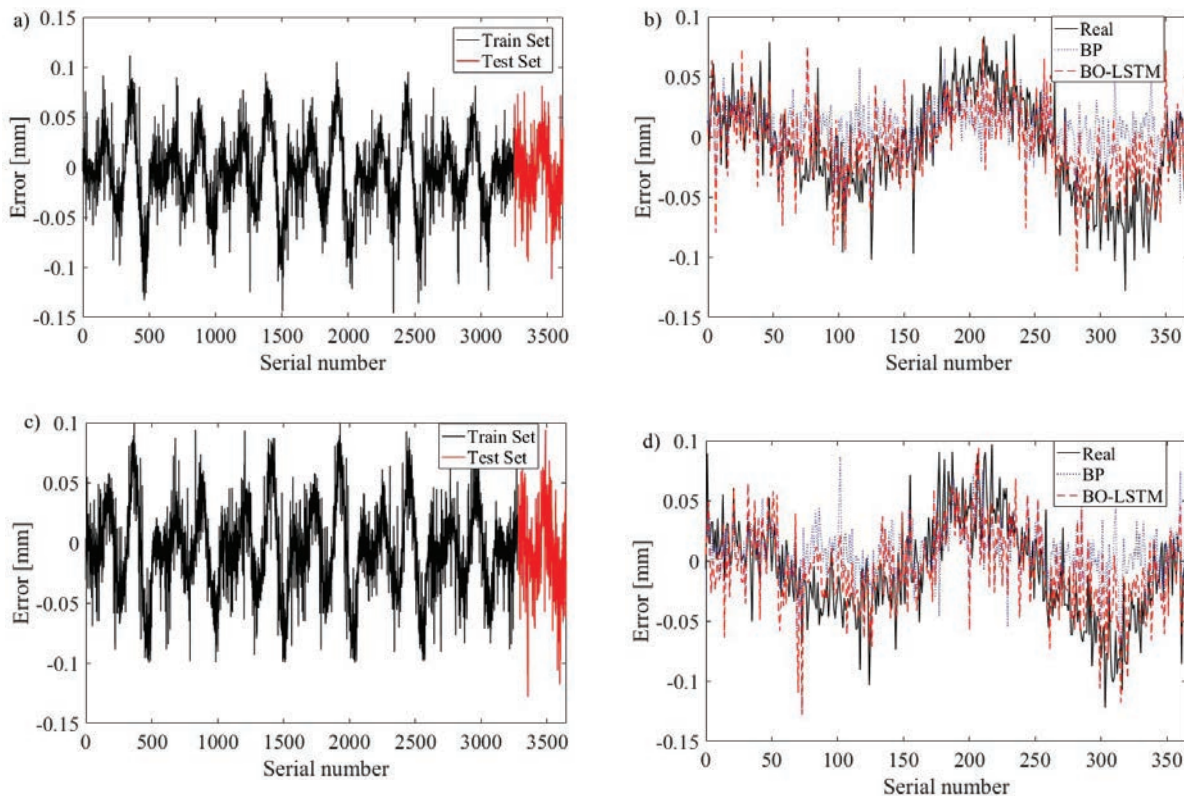
Fig. 5. *Spiral trajectory error prediction; a) data samples on X-axis; b) prediction results on X-axis; c) data samples on Y-axis; d) prediction results on Y-axis*

Table 1. The training time in the *X* and *Y* directions is 42 min and 46 min, respectively. The MSE, RMSE, and MAE of the prediction error in *X* direction are 0.96 %, 9.80 %, and 7.29 %, respectively; the MSE, RMSE and MAE of the prediction errors in *Y* direction are 1.04 %, 10.18 %, and 6.51 %, respectively. When using the BO-LSTM prediction model for trajectory error prediction, the training time in *X* and *Y* directions are reduced to 9 min and 7 min, respectively.

Further analysis of the prediction results shows that the MSE, RMSE, and MAE of the prediction error in the *X* direction were 0.09 %, 2.99 %, and 2.32 %, respectively; the MSE, RMSE, and MAE of the prediction error in the *Y* direction were 0.10 %, 3.14 %, and 2.46 %, respectively. Moreover, through the predicted trajectory error data of 14.6 s, the prediction results of

the two models are analysed through the error integration criterion. It can be seen that the IAE, ISE, ITAE, and ITSE of the prediction error of BO-LSTM in the *X* direction are reduced to 56.44 %, 33.33 %, 53.63 %, and 30.47 %, respectively compared with the prediction error of the BP neural network; the IAE, ISE, ITAE, and ITSE of the prediction error of BO-LSTM in the *Y* direction are reduced to 57.87 %, 37.84 %, 54.79 %, and 34.27 % respectively compared with the prediction error of BP neural network. In summary, the prediction accuracy of the established BO-LSTM end trajectory error prediction model is significantly higher than that of the traditional BP neural network, which further verifies the accuracy and effectiveness of the established model.

Table 1. *Analysis of spiral trajectory error prediction results*

Direction	Model	Training time [min]	MSE [%]	RMSE [%]	MAE [%]	IAE	ISE	ITAE	ITSE
X	BP	42	0.96	9.80	7.29	0.6176	0.0402	5.0697	0.3547
	LSTM	9	0.09	2.99	2.32	0.3486	0.0134	2.7187	0.1081
Y	BP	46	1.04	10.18	6.51	0.5920	0.0370	4.7360	0.3131
	LSTM	7	0.10	3.14	2.46	0.3426	0.0140	2.5754	0.1073

4 CONCLUSION

This study investigated a method for predicting the trajectory error of the end execution point of a LOMPR. The hyperparameters were optimized using a Bayesian method, and a BO-LSTM deep neural network was established to optimize the learning rate, batch capacity, and number of hidden neurons to improve the efficiency and accuracy of the model search. Considering the working characteristics of the CCOS grinding system as a tool, the collected kinematic data of the LOMPR were processed, including time stitching, missing data processing, abnormal data processing, and normalization processing, to improve the learning efficiency of the deep learning network. Finally, in end trajectory error prediction experiments using a spiral trajectory, the trajectories in X and Y directions were predicted. At the same time, BP neural network prediction model is used to predict the end trajectory error of LOMPR. The prediction results had high accuracy, and the training time of the model was greatly reduced. Compared with the prediction results of a BP neural network, the training time of BO-LSTM prediction model in X and Y directions are reduced to 21.4 % and 15.2 %, respectively; The MSE, RMSE, and MAE of the prediction error in the X direction are reduced to 9.4 %, 30.5 %, and 31.8 %, respectively; MSE, RMSE, and MAE of the prediction error in Y direction were reduced to 9.6 %, 30.8 %, and 37.8 %, respectively. The validity and accuracy of the model were verified, which provides a reliable theoretical basis and data support for the feedforward compensation of the end trajectory error of a future LOMPR. In addition, the BO-LSTM error prediction model proposed in this paper could be widely used in kinematic error prediction for other parallel and hybrid robots.

6 ACKNOWLEDGEMENT

7 REFERENCES

[1] Jiang, B.C., Zhao, D.W., Wang, B.Q., Zhao, H.J., Liu, Y.H., Lu, X.C. (2020). Flatness maintenance and roughness reduction of silicon mirror in chemical mechanical polishing process. *Science China-Technological Sciences*, vol. 63, no. 1, p. 166-172, **DOI:10.1007/s11431-018-9414-6**.

[2] Kong, Y.X., Cheng, G., Guo, F., Gu, W., Zhang, L.B. (2019). Inertia matching analysis of a 5-DOF hybrid optical machining manipulator. *Journal of Mechanical Science and Technology*, vol. 33, no. 10, p. 4991-5002, **DOI:10.1007/s12206-019-0938-1**.

[3] Erkaya, S. (2018). Effects of joint clearance on the motion accuracy of robotic manipulators. *Strojniški vestnik - Journal of Mechanical Engineering*, vol. 62, no. 2, p. 82-94, **DOI:10.5545/sv-jme.2017.4534**.

[4] Iqbal, J., Ullah, M.I., Khan, A.A., Irfan, M. (2015). Towards sophisticated control of robotic manipulators: an experimental study on a pseudo-industrial arm. *Strojniški vestnik-Journal of Mechanical Engineering*, vol. 61, no. 7, p. 465-470, **DOI:10.5545/sv-jme.2015.2511**.

[5] Jin, Z.J., Cheng, G., Chen, S.B., Guo F. (2021). Human-machine-environment information fusion and control compensation strategy for large optical mirror processing system. *Proceedings of the Institution of Mechanical Engineers, Part C: Journal of Mechanical Engineering Science*, vol. 235, no. 13, p. 2507-2523, **DOI:10.1177/0954406220959689**.

[6] Liao, W.L., Dai, Y.F., Xie, X.H., Zhou, L., Yuan Z. (2012). Corrective capability analysis and machining error control in ion beam figuring of high-precision optical mirrors. *Optical Engineering*, vol. 51, no. 3, **DOI:10.1117/1.0E.51.3.033402**.

[7] Zhong, X.Y., Fan, B., Wu, F. (2017). High-accuracy process based on the corrective calibration of removal function in the magnetorheological finishing. *Optical Engineering*, vol. 56, no. 8, **DOI:10.1117/1.0E.56.8.084109**.

[8] Pan, H.H., He, X.X., Tang, S., Meng, F.M. (2018). An improved bearing fault diagnosis method using one-dimensional CNN and LSTM. *Strojniški vestnik - Journal of Mechanical Engineering*, vol. 64, no. 7-8, p. 443-452, **DOI:10.5545/sv-jme.2018.5249**.

[9] Baizid, K. Cukovic, S. Iqbal, J. Yousnadj, A. Chellali, R. Meddahi, A. Devedzic, G., Ghionea, I. (2016). IRoSim: industrial robotics simulation design planning and optimization platform based on CAD and knowledgeware technologies. *Robotics and Computer-Integrated Manufacturing*, vol. 42, p. 121-134, **DOI:10.1016/j.rcim.2016.06.003**.

[10] Singh A., Pandey P., Nandi G.C. (2021). Effectiveness of multi-gated sequence model for the learning of kinematics and dynamics of an industrial robot. *Industrial Robot - the International Journal of Robotics Research and Application*, vol. 48, no. 1, p. 62-70, **DOI:10.1108/IR-01-2020-0010**.

[11] Wang, S.J., Shao, X.M., Yang, L.S., Liu, N. (2020). Deep learning aided dynamic parameter identification of 6-DOF robot manipulators. *IEEE Access*, vol. 8, p. 138102-138116, **DOI:10.1109/ACCESS.2020.3012196**.

[12] Wang, H.L., Xie, Y.C. (2019). Prediction error based adaptive Jacobian tracking of robots with uncertain kinematics and dynamics. *IEEE Transactions on Automatic Control*, vol. 52, no. 12, p. 2889-2894, **DOI:10.1109/TAC.2009.2033764**.

[13] Dai, S.Z., Li, L., Li, Z.H. (2019). Modeling vehicle interactions via modified LSTM models for trajectory prediction. *IEEE Access*, vol. 7, p. 38287-38296, **DOI:10.1109/ACCESS.2019.2907000**.

[14] Mici, L., Parisi, G.I., Wermter, S. (2018). An incremental self-organizing architecture for sensorimotor learning and prediction. *IEEE Transactions on Cognitive and Developmental*

Systems, vol. 10, no. 4, p. 918-928, **DOI:10.1109/TCDS.2018.2832844**.

[15] Mirzaeinejad, H., Shafei, A.M. (2018). Modeling and trajectory tracking control of a two-wheeled mobile robot: Gibbs-Appell and prediction-based approaches. *Robotica*, vol. 36, no. 10, p. 1551-1570, **DOI:10.1017/S0263574718000565**.

[16] Wang, H.L., Xie, Y.C. (2012). Prediction error based adaptive Jacobian tracking for free-floating space manipulators. *IEEE Transactions on Aerospace and Electronic Systems*, vol. 48, no. 4, p. 3207-3221, **DOI:10.1109/TAES.2012.6324694**.

[17] Las-Casas, M.S., Diniz de Avila, T.L.D., Bracarense, A.Q., Lima, E.J. (2018). Weld parameter prediction using artificial neural network: FN and geometric parameter prediction of austenitic stainless steel welds. *Journal of the Brazilian Society of Mechanical Sciences and Engineering*, vol. 40, no. 1, **DOI:10.1007/s40430-017-0928-0**.

[18] Wang, Y., Yang, Y.Y., Zhao, B.L., Qi, X.Z., Hu, Y., Li, B., Sun, L.N., Zhang, L.H., Meng, M.Q.H. (2021). Variable admittance control based on trajectory prediction of human hand motion for physical human-robot interaction. *Applied Sciences*, vol. 11, no. 12, **DOI:10.3390/app11125651**.

[19] Zhang, G., Xu, Z., Hou, Z.C., Yang, W.L., Liang, J.M., Yang, G., Wang, J., Wang, H.M., Han, C. (2020). A Systematic error compensation strategy based on an optimized recurrent neural network for collaborative robot dynamics. *Applied Sciences*, vol. 10, no. 19, **DOI:10.3390/app10196743**.

[20] Yang, Q.B., Li, X., Cai, H.S., Hsu, Y.M., Lee, J., Yang, C.H., Li, Z.L., Lin, M.Y. (2021). Fault prognosis of industrial robots in dynamic working regimes: Find degradation in variations. *Measurement*, vol. 173, **DOI:10.1016/j.measurement.2020.108545**.

[21] Chebbi, A.H., Chouaibi, Y., Affi, Z., Romdhane, L. (2018). Sensitivity analysis and prediction of the orientation error of a three translational parallel manipulator. *Proceedings of the Institution of Mechanical Engineers Part C-Journal of Mechanical Engineering Science*, vol. 232, no. 1, p. 140-161, **DOI:10.1177/0954406216675380**.

[22] Zatout, M.S., Rezoug, A., Rezoug, A., Baizid, K., Iqbal, J. (2022). Optimisation of fuzzy logic quadrotor attitude controller - particle swarm, cuckoo search and BAT algorithms. *International Journal of Systems Science*, vol. 53, no. 4., p. 883-908, **DOI:10.1080/00207721.2021.1978012**.

[23] Peng, G.L., Ji, M.Y., Xue, Y., Sun, Y. (2021). Development of a novel integrated automated assembly system for large volume components in outdoor environment. *Measurement*, vol. 168, **DOI:10.1016/j.measurement.2020.108294**.

[24] You, J.J., Xi, F.F., Shen, H.P., Wang, J.Y., Yang, X.L. (2021). A novel Stewart-type parallel mechanism with topological reconfiguration: Design, kinematics and stiffness evaluation.

Mechanism and Machine Theory, vol. 162, **DOI:10.1016/j.mechmachtheory.2021.104329**.

[25] He, J., Ding, Q.Y., Gao, F., Zhang, H.B. (2020). Kinematic calibration methodology of hybrid manipulator containing parallel topology with main limb. *Measurement*, vol. 152, **DOI:10.1016/j.measurement.2019.107334**.

[26] Li, Y., Zhu, Z.F., Kong, D.Q., Han, H., Zhao, Y. (2019). EA-LSTM: Evolutionary attention-based LSTM for time series prediction. *Knowledge-Based Systems*, vol. 181, **DOI:10.1016/j.knosys.2019.05.028**.

[27] Ahmad, E., Iqbal, J., Khan, M.A., Liang, W., Youn, I. (2020). Predictive control using active aerodynamic surfaces to improve ride quality of a vehicle. *Electronics*, vol. 16, no. 11, **DOI:10.3390/electronics9091463**.

[28] Ullah, M.I., Ajwad, S.A., Irfan, M., Iqbal, J. (2016). MPC and H-infinity based feedback control of non-linear robotic manipulator. *14th International Conference on Frontiers of Information Technology (FIT)*, p. 136-141, **DOI:10.1109/FIT.2016.033**.

[29] Ali, N., Ayaz Y., Iqbal, J. (2022). Collaborative position control of pantograph robot using particle swarm optimization. *International Journal of Control Automation and Systems*, vol. 20, no. 1, p. 198-207, **DOI:10.1007/s12555-019-0931-6**.

[30] Bai, G.X., Meng, Y., Liu, L., Luo, W.D., Gu, Q. (2019). Review and comparison of path tracking based on model predictive control. *Electronics*, vol. 8, no. 10, **DOI:10.3390/electronics8101077**.

[31] Shen, S.B., Song, A.G., Li, T., Li, H.J. (2019). Time delay compensation for non-linear bilateral teleoperation: A motion prediction approach. *Transactions of the Institute of Measurement and Control*, vol. 41, no. 16, p. 4488-4498, **DOI:10.1177/0142331219860928**.

[32] Tang, G., Wu, Y.F., Li, C.S., Wong, P.K., Xiao, Z.H., An, X.L. (2020). A novel wind speed interval prediction based on error prediction method. *IEEE Transactions on Industrial Informatics*, vol. 16, no. 11, p. 6806-6815, **DOI:10.1109/TII.2020.2973413**.

[33] Wang, B.K., Peng, X.Y., Jiang, M., Liu, D.T. (2020). Real-Time fault detection for UAV based on model acceleration engine. *IEEE Transactions on Instrumentation and Measurement*, vol. 69, no. 12, p. 9505-9516, **DOI:10.1109/TIM.2020.3001659**.

[34] Mei, M.L., Chang, J., Li, Y.L., Li, Z.R., Li, X.C., Lv, W.J. (2019). Comparative study of different methods in vibration-based terrain classification for wheeled robots with shock absorbers. *Sensors*, vol. 19, no. 5, **DOI:10.3390/s19051137**.

[35] Wu, Y.T., Yuan, M., Dong, S.P., Lin, L., Liu, Y.Q. (2018). Remaining useful life estimation of engineered systems using vanilla LSTM neural networks. *Neurocomputing*, vol. 275, p. 167-179, **DOI:10.1016/j.neucom.2017.05.063**.

Optimisation of PLA Filament Consumption for 3D Printing Using the Annealing Method in Home Environment

Milena Djukanović[1, *] – Milanko Damjanović[2] – Luka Radunović[2] – Mihailo Jovanović[3]

[1]University of Montenegro, Faculty of Electrical Engineering, Montenegro
[2]University of Montenegro, Faculty of Mechanical Engineering, Montenegro
[3]Adriatik University, Faculty of Management Herceg Novi, Montenegro

The idea for this paper came with the outbreak of the Covid-19 pandemic when almost all countries started experiencing shortages of different, previously abundant, materials. As with all other communities, these shortages prompted the 3D printing community to become more involved in the global fight against the Covid-19. This fight was further facilitated by a large number of world-famous companies which provided their 3D models of protective masks, visors, and other aids to medical staff free of charge together with the recommended parameters and open-source files used for their printing. The idea of these companies was to support their countries by providing protective equipment for everyone who sorely needed it, especially at the beginning of the pandemic, but this mass 3D printing led to a shortage of 3D printing filaments. One of the main ideas behind this paper is to show that this problem can be drastically reduced by optimising filament consumption when printing those models. One way of doing this is strengthening the printed element by annealing it, which is the topic of this paper. By strengthening it afterwards, one could reduce filament consumption by reducing the infill percentage in the G code creation procedure. For this research, we opted for a polylactide acid (PLA) filament, because it is the most widely used 3D printing material. By varying its annealing temperature and time, and testing it, the results gave us an optimal procedure for strengthening the PLA prints, as well as an optimal solution for consumption reduction that would be the most suitable during material shortages. These results could be of great significance if applied globally.

Keywords: Covid-19; 3D printing; consumption optimisation; annealing; PLA material; PLA strengthening

Highlights
- *Protective equipment 3D printing is one of the measures against the spread of Covid-19.*
- *The consumption 3D printing PLA filament is optimised by post-print filament baking.*
- *We have determined the optimal baking temperature for the PLA annealing procedure.*
- *Matching annealed model dimensions to the desired one by scaling it before printing.*

0 INTRODUCTION

Additive manufacturing, with its typical representative – three dimensional (3D) printer, has enabled every user to become a small scale manufacturer [1]. Those small-scale manufacturers may not be able to have a huge impact on society in terms of mass-produced items, but united they have the potential and power that exceeds the capacities of factory plants, at least for a short period, in terms of their ultra-rapid adaptation to the market. The typical mass-produced plastic items are produced through the following sequence: designing a product, iterative process between the designer and production engineer to make sure the product is producible, optimising the product, making production plans, moulds, post-production of the moulds etc. [2]. Compared to typical manufacturing, 3D printing is capable of using a trial and error method, where a designer can print a model and try it in real life without any loss (except filament loss). If that design is not capable of performing a wanted task, the designer can continue improving the model, if needed, until it fulfils all the defined goals. This approach came in handy at the start of the

Covid-19 pandemic when there was a significant lack of medical protective equipment. [3] and [4].

Soon after the outbreak of the Covid-19 pandemic in Montenegro, protective gear supply of medical equipment approached minimum, meaning there was an insufficient amount of equipment to cover all the hospitals and hospital units' needs. Also, the supply chain from other countries was severely disrupted due to stricter and time-consuming border control which delayed supplies for a long time, causing great problems for our country as well as for the whole world. By looking at the examples of other countries that faced this pandemic before its outbreak in Montenegro, enthusiastic 3D printing communities and hubs in the country started manufacturing everything that could be made on printers and that was desperately needed at that time [5]. Soon after that, at the initiative of the Faculty of Electrical Engineering of the University of Montenegro and the Science and Technology Park of Montenegro, with the support of the Montenegrin Ministry of Science, all 3D printers in the country were clustered (45 functional fused deposition modelling (FDM) printers in Montenegro) and we made a national cluster, which

*Corr. Author's Address: Faculty of Electrical Engineering, University of Montenegro, 81000 Podgorica, Montenegro; milenadj@ucg.ac.me

185

altogether resembles a mass production company since all printers printed the same models of protective equipment as per the standards provided by the Institute of Public Health of Montenegro [6]. The most printed equipment were protective visors, together with publicly available models of oxygen masks and tubes for respirators that were manufactured as spare parts for medical units if needed [7].

The exponential growth of infected people increased the demand for protective visors to such a high degree that the 3D printing cluster barely managed to produce sufficient quantities [8]. As mentioned, stricter border controls were hampering imports that soon enough reflected on the manufacturing of visors, as Montenegro does not have its filament production. This "Printing crisis", that hit 3D printing manufacturers in Montenegro after two weeks into the pandemics, could have been partially postponed by somehow optimising the consumption of filaments until the newly ordered filament crossed the border and became available [9].

This paper aims to precisely describe the process of strengthening the polylactide acid (PLA) 3D printing material, which is performed via the annealing process, which makes it possible to reduce the amount of material used in printing. Annealing of plastic drastically increases its firmness, tensile strength and temperature resistance, and is a well-known procedure in plastic injection moulding, but not so widespread in the post-production of 3D printed parts [10]. This process requires heating a printed element to a temperature between glass transition and melting and waiting for a certain amount of time to harden. By creating a perfect blend of the chosen annealing temperature and time, later tests of the specimens in our experimental equipment, yielded optimal numbers which may be used in optimising 3D models, so that the number of 3D printed elements can be greater for the same amount of the used material [11].

1 METHODOLOGY

1.1 Materials

The goal of this research is to analyse the annealing process of the PLA filament, most commonly used in 3D printing, make tensile strength graphs showing the relation between annealing temperature and time and choose the best annealing process that is suitable for small scale 3D manufacturers who do not have spacious workshops and who are not capable of super-precision "baking".

The filament used in this research is a standard PLA filament, commercially available in a mid-range quality, printed with standard PLA printing settings (205 °C head temperature, 60 °C bed temperature) on Craftbot FLOW IDEX XL 3D printer [12] and [13]. Since the PLA is a polymer, it has two types of molecular structures: chaotic and partially organised – amorphous and semicrystalline [14]. When the filament is melted, its molecular chains become disorganised (amorphous), flexible and elastic. Due to rapid cooling, its molecular structure remains the same, and its tensile strength, firmness and heat resistance are inferior to the organised chain structure, which is crystalline [15].

Hence, in order to arrange those polymer chains from amorphous to semi-crystalline structure, the temperature needs to be within a certain range for a certain amount of time. "Activation temperature" of organising the chains is called a glass transition temperature [16]. It ranges from the lower temperature point within the annealing process and for the PLA material it is 65 °C, up to the melting temperature, which is around 160 °C – the upper-temperature point. Choosing the right temperature is not that easy to achieve, but the closer the temperature is to the melting point (still in semi-crystalline transition state) the more uniform/merged will be the printed layers. Furthermore, by merging its layers, an object is less likely to "snap" on the printing plane, as shown in Fig. 1, but the printed element will be highly deformed, thus the decision to merge the layer or not depends on the purpose/use of the object [17].
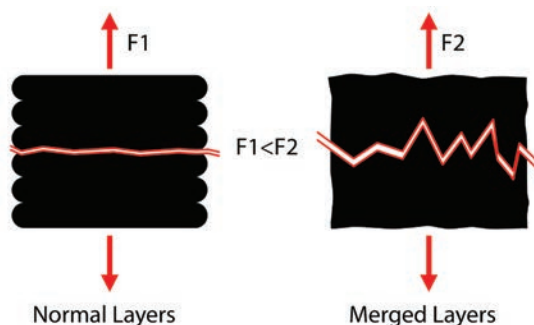
Fig. 1. *Normal and annealed 3D printed element difference – side view*

Tensile strength testing was performed on the testing setup shown in Fig. 2, with the calculated sensor precision of 1 %, using the specimens/samples (also see Fig. 2) divided into 5 batches with 5 different annealing temperatures for 3 different baking times [18].
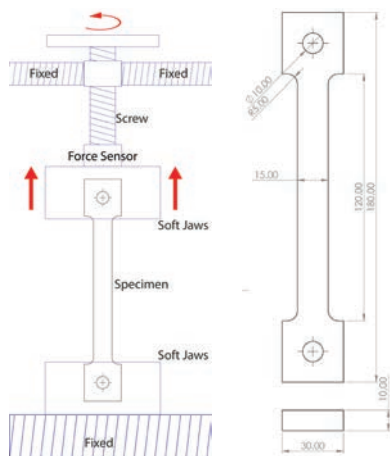
Fig. 2. *Tensile strength tester and specimen dimensions (units in mm)*

1.2 Process Parameters

Results obtained from the tensile strength tester at different baking temperatures and times were entered in "Force value" fields shown in Table 1, and then averaged for each of the columns in the Table and plotted in graphs for easier readability. Baking times were: (30, 60 and 90) minutes, and baking temperatures were: room temperature (i.e. no baking), (70, 90, 110 and 130) °C [17].

Table 1. *The table used for tensile strength test results*

Test num. 1	Baking time: 30 min / 60 min / 90 min			
	Annealing temperature			
Spec. num.	70	90	110	130
1	Force value	Force value	Force value	Force value
2	Force value	Force value	Force value	Force value
3	Force value	Force value	Force value	Force value
4	Force value	Force value	Force value	Force value
5	Force value	Force value	Force value	Force value
Avg. value	Force value	Force value	Force value	Force value

Specimens shown in Fig. 3 were printed on a Craftbot FLOW IDEX XL 3D printer, as mentioned before, with the following printing parameters – Head temperature 205 °C, bed temperature 60 °C, infill 100 % and Z movement 0.2 mm, as shown in Fig. 4. Computer aided manufacturing (CAM) slicing software used in this G code creation is CraftWare. For the best possible adhesion on the aforementioned 3D printer, we added a "raft" underneath the model, to ensure the specimen was completely parallel to the printing bed and without any warping or layer shifting.

Printing was done in sets, with three specimens on each set [19].
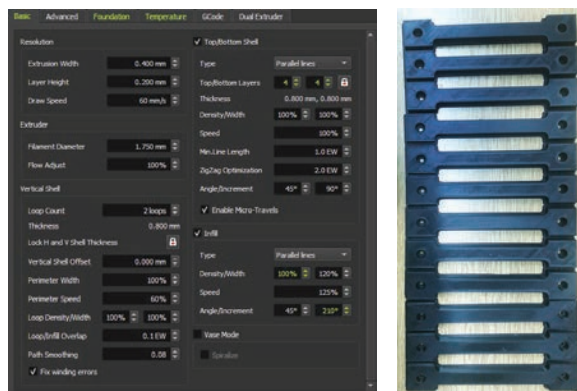
Fig. 3. *Printing parameters and the printed model, shown in CraftWare software*

After the printing of all sixty-five specimens, they were classified into two groups. One group of five was used for non-hardened testing and those results were put in a separate table, while the other sixty specimens were separated first into three groups (for different baking times), and then all the mentioned groups were further each divided into four smaller groups intended for different baking temperatures. Since this research is intended for small scale 3D printing manufacturers around the globe (using our data for optimising the filament use), it was not appropriate to "bake" the specimens in expensive laboratory ovens, but rather in a standard, cheap electric kitchen oven, that every house or a small-scale manufacturing facility should have or should be able to easily acquire. The baking was done by first heating the oven to the desired temperature, then letting the temperature settle for ten minutes, then putting five specimens inside the oven, until the selected time elapsed, then letting specimens cool to room temperature outside the oven. All specimens were firstly heat-treated/annealed and exposed to the same standard room temperature/ humidity conditions before testing on the tensile strength testing unit, so as to obtain the testing results which would be as objective as possible.

2 EXPERIMENTAL RESULTS

Small irregularities like PLA filament uneven moisture level, various degrees of purity of different filament segments, some external factors like room temperature and humidity may affect each print differently, so the more specimens used for the same test, the better. The results of tensile strength tests

are shown in Table 2 (in Newtons) and are visually presented in graphs shown in Fig. 4 [20].

Table 2. *Testing results for baking time, a) 30 min, b) 60 min, and c) 90 min*

a) Test num. 1	Baking time: 30 min			
Specimen num.	Annealing temperature			
	70 °C	90 °C	110 °C	130 °C
1	6509.81 N	6699.16 N	6403.13 N	6342.62 N
2	6505.92 N	6675.30 N	6393.00 N	6336.54 N
3	6565.43 N	6736.34 N	6451.49 N	6394.52 N
4	6525.43 N	6695.32 N	6412.18 N	6355.55 N
5	6606.44 N	6778.40 N	6491.80 N	6434.48 N
Avg. value	6542.61 N	6716.91 N	6430.32 N	6372.74 N

b) Test num. 2	Baking time: 60 min			
Specimen num.	Annealing temperature			
	70 °C	90 °C	110 °C	130 °C
1	6643.88 N	6815.51 N	6529.45 N	6472.24 N
2	6599.76 N	6770.26 N	6486.09 N	6429.25 N
3	6658.08 N	6830.08 N	6543.41 N	6486.07 N
4	6627.71 N	6798.94 N	6513.56 N	6456.49 N
5	6599.45 N	6769.95 N	6485.78 N	6428.95 N
Avg. value	6625.77 N	6796.95 N	6511.66 N	6454.60 N

c) Test num. 3	Baking time: 90 min			
Specimen num.	Annealing temperature			
	70 °C	90 °C	110 °C	130 °C
1	6600.04 N	6769.53 N	6487.05 N	6430.55 N
2	6621.25 N	6791.28 N	6507.89 N	6451.22 N
3	6631.96 N	6802.27 N	6518.42 N	6461.65 N
4	6697.77 N	6869.77 N	6583.11 N	6525.78 N
5	6632.54 N	6802.86 N	6518.99 N	6462.22 N
Avg. value	6636.71 N	6807.14 N	6523.09 N	6466.28 N

Compared to the non-hardened specimens, whose averaged deformation resistance was 5711 N, the annealed ones showed a significantly greater deformation resistance, which was around 20 % greater than before the annealing process. As the annealing temperature exceeds glass transition, the molecular structure of long polymer chains becomes more and more organised, resulting in a stiffer element, but as the temperature rises to the melting temperature, the cross-section area of the specimen shrinks as the elongation of the longitudinal axis increases, thus creating higher pressure on that area, resulting in a slightly lower deformation resistance. Temperatures higher than 130 °C were not taken into consideration both due to the aforementioned problem and the problem with material deformation that would present a big problem when trying to anneal some 3D printed elements intended for mechanical

manipulation, such as artistic design elements or something similar [17].
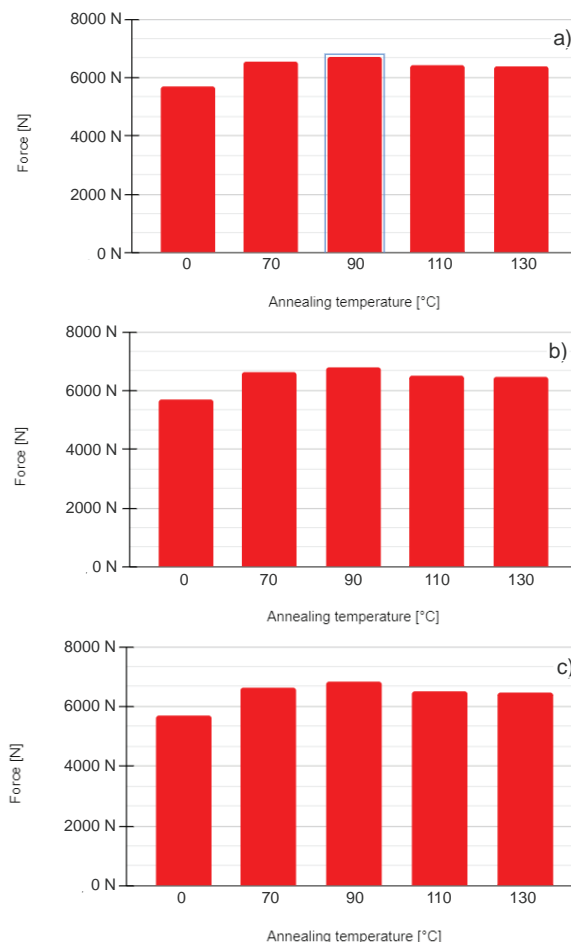
Fig. 4. *Tensile strength graph with annealing time; a) 30 min, b) 60 min, and c) 90 min*

Higher baking temperatures caused deformation of the tensile test material and elongation of around 10 % (x-axis shown in Table 3). Shrinking of the cross-section (y, z-axis in Table 3) is a bit lower than elongation – around 9 % at the mentioned higher baking temperatures, up to the melting point of the specimen when horizontal elongation increases rapidly.

Table 3. *Deformation of the specimens*

Deformation [%]	Baking temperature [°C]				
	0	70	90	110	130
x	0	2	4	6	10
y	0	1	3	5	9
z	0	2	3	4	9

By arranging averaged data in one table and creating a baking temperature-time matrix as shown in Table 4, one can decide if it is prudent to invest more time in annealing the printed elements if the result is only a small difference in tensile strength.
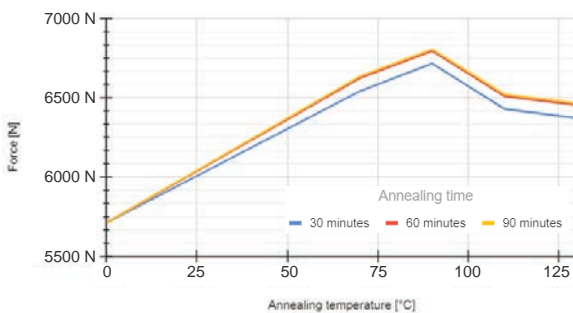
Table 4. *Baking temperature-time matrix*

Baking time [min]	Baking temperature [°C]				
	0	70	90	110	130
30	5711.83	6542.61	6716.91	6430.32	6372.74
60	5711.83	6625.77	6796.95	6511.66	6454.60
90	5711.83	6636.71	6807.14	6523.09	6466.28

In Fig. 5 we can see the normal distribution of the data of the test tube baked most optimally. It gives us information not only on the average value of the force that this sample can withstand, but also gives us the data on the maximum and minimum force measured during the testing as well as the data on the frequency of occurrence of this force. This was done with the testing of one hundred specimens baked for 60 min at 90 °C.
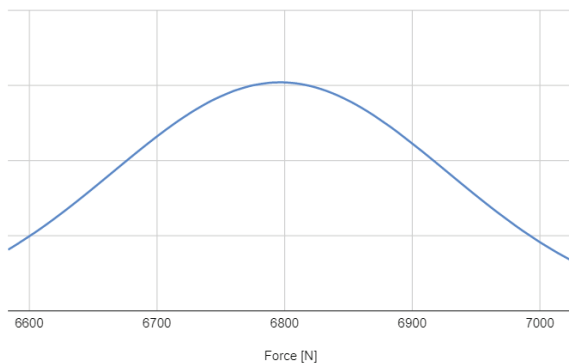
Fig. 5. *Normal distribution of the data of the test tube*

Fig. 6. *Baking temperature-time graph*

Allowing temperature to penetrate through the walls of a printed element to its internal layers, a better semi-crystalline structure can be obtained and the stiffness of the element will be higher, as shown in Fig. 6, but that will take a lot of time for some prints, so it is important to have a plan that will strike a perfect balance between the time spent and the level of obtained tensile strength.

3 CONCLUSIONS

With the aforementioned plan related to the filament strengthening method, one can save a lot of material while mass-producing some elements, but the problem is that a regular home oven would be inadequate for the sheer number of prints. Fixing that just by boiling prints in water instead of baking them in the oven would save a lot of time, as the printed element only needs to be heated to a specific temperature (that happens to match the water boiling temperature). The deformation that occurs at this tested temperature and the annealing time range was measured to be below 5 %, which is quite acceptable for most of the 3D printed elements, and just by simply fixing the scale of the element when creating the G code, that deformation would approach zero after the annealing [21]. This study concluded that the material optimisation of 3D printed elements was easily doable using the PLA annealing process explained in this paper. With this kind of optimisation, small scale manufacturers may save a lot of filament material in the long term, which is highly useful for the situations like the one that emerged this year with the Covid-19-related "filament shortage crisis" in Montenegro [22].

4 ACKNOWLEDGEMENTS

5 REFERENCES

[1] Gibson I., Rosen, D.W., Stucker B. (2015). *Additive Manufacturing Technologies*. Springer New York, **DOI:10.1007/978-1-4939-2113-3**.

[2] Mongeon, B. (2016). *3D Technology in Fine Art and Craft: Exploration of 3D Printing, Scanning, Sculpting and Milling*. Routledge Publishing, Oxfordshire, **DOI:10.4324/9781315730455**.

[3] Redwood, B., Schoffer, F., Garret, B. (2017). *The 3D Printing Handbook: Technologies, Design, and Applications*. 3D Hubs B.V., Amsterdam

[4] Tarfaoui, M., Nachtane, M, Goda, I., Qureshi, Y., Benyahia, H. (2020). 3D printing to support the shortage in personal

protective equipment caused by Covid-19 pandemic. *Materials*, vol. 13, no. 15, art. ID 3339, **DOI:10.3390/ma13153339**.

[5] Rendeki, S., Nagy, B., Bene, M., Pentek, A., Toth, L., Szanto, Z., Told, R., Maroti, P. (2020). An overview on personal protective equipment (PPE) fabricated with additive manufacturing technologies in the era of COVID-19 pandemic. *Polymers*, vol. 12, no. 11, art. ID 2703, **DOI:10.3390/polym12112703**.

[6] Djukanovic, M., Jovanovic, M., Pejovic, N., Lutovac, D. (2021). 3D Printing Solutions in the Fight Against Covid-19 Pandemic. *Lecture Notes in Networks and Systems*, vol. 233, p.310-322, **DOI:10.1007/978-3-030-75275-0_35**.

[7] Tino, R., Moore, R., Antoline, S. (2020). COVID-19 and the role of 3D printing in medicine. *3D Printing in Medicine*, vol. 6, art. ID 11, **DOI:10.1186/s41205-020-00064-7**.

[8] Garcia Godoy, L.R., Jones, A.E., Anderson, T.N., Fisher, C.L., Seeley, K.M.L., Beeson, E.A., Zane, H.K., Peterson, J.W., Sullivan, P.D. (2020). Facial protection for healthcare workers during pandemics: a scoping review. *BMJ Global Health*, vol. 5, no. 5, art. ID e002553, **DOI:10.1136/bmjgh-2020-002553**.

[9] RT Magazine (2020). Montenegro: Europe's Last Coronavirus-free Country. from *https://rtmagazine.com/disorders-diseases/infectious-diseases/other-infections/montenegro-coronavirus-free-europe/*, accessed on 2020-10-16.

[10] Durso, M. (2017). *Investigating Annealed Semi-Crystalline PLA Composites used in 3D Printing*. **DOI:10.13140/RG.2.2.14416.81920**.

[11] Blok, L.G., Longana, M.L., Yu, H., Woods, B.K.S. (2010). An investigation into 3D printing of fibre reinforced thermoplastic composites. *Additive Manufacturing*, vol. 22. p. 176-186, **DOI:10.1016/j.addma.2018.04.039**.

[12] Wang, X., Jiang, M., Zhou, Z., Gou, J., Hui, D. (2017). 3D printing of polymer matrix composites: A review and prospective. *Composites Part B: Engineering*, vol. 110, p. 442-458, **DOI:10.1016/j.compositesb.2016.11.034**.

[13] Shahrubudin, N., Lee, T.C., Ramlan, R. (2019). An Overview on 3D Printing Technology: Technological, Materials, and Applications. *Procedia Manufacturing*, vol. 35, p. 1286-1296, **DOI:10.1016/j.promfg.2019.06.089**.

[14] Kuo, C.-C., Chen, J.-Y., Chang, Y.-H. (2021). Optimization of process parameters for fabricating polylactic acid filaments using design of experiments approach. *Polymers*, vol. 13, no. 8, art. ID 1222, **DOI:10.3390/polym13081222**.

[15] Park, S., Rosen, D.W. (2016). Quantifying effects of material extrusion additive manufacturing process on mechanical properties of lattice structures using as-fabricated voxel modeling. *Additive Manufacturing*, vol. 12, part B. p. 265-273, **DOI:10.1016/j.addma.2016.05.006**.

[16] Auffray, L., Gouge, P.A., Hattali, L. (2021) Design of experimental analysis on tensile properties of PLA samples produced by fused filament fabrication. *The International Journal of Advanced Manufacturing Technology*, vol. 118, p. 4123-4137, **DOI:10.1007/s00170-021-08216-7**.

[17] Kočí, J. (2019). How to improve your 3D prints with annealing. Prusaprinters Blog, from *https://blog.prusaprinters.org/how-to-improve-your-3d-prints-with-annealing_31088/*, accessed on 2020-03-13.

[18] Kerekes, T.W., Lim, H., Joe, W.Y., Yun, G.J. (2019). Characterization of process-deformation/damage property relationship of fused deposition modeling (FDM) 3D-printed specimens. *Additive Manufacturing*, vol. 25, p. 532-544, **DOI:10.1016/j.addma.2018.11.008**.

[19] Bryła, J., Martowicz, A. (2021). Study on the Importance of a Slicer Selection for the 3D Printing Process Parameters via the Investigation of G-Code Readings. *Machines*, vol. 9, no. 163. **DOI:10.3390/machines9080163**.

[20] Chacón, J.M., Caminero, M.A., García-Plaza, E., Núñez, P.J. (2017). Additive manufacturing of PLA structures using fused deposition modeling: Effect of process parameters on mechanical properties and their optimal selection. *Materials & Design*, vol. 124, p. 143-157, **DOI:10.1016/j.matdes.2017.03.065**.

[21] Bhandari, S., Lopez-Anido, R.A., Gardner, D.J. (2019). Enhancing the interlayer tensile strength of 3D printed short carbon fiber reinforced PETG and PLA composites via annealing. *Additive Manufacturing*, vol. 30, art. ID 10922, **DOI:10.1016/j.addma.2019.100922**.

[22] Djukanović, M., Mavrić, A., Jovanović, J., Roganović, M., Bošković, V. (2021). Design of 3D printing thermo-sensored medical gear in detecting COVID-19 symptoms. *Applied Sciences*, vol. 11, no. 1, art. ID 419, **DOI:10.3390/app11010419**.

Adaptive Electromagnetic Vibration Absorber for a Multimode Structure

Khaled S. Mohamed[1] – Fatin Amri[2] – Mostafa Elboraey[1] – N.H. Diyana Nordin[2] – Asan G.A. Muthalif[1,*]

[1] Qatar University, College of Engineering, Qatar
[2] International Islamic University Malaysia, Department of Mechatronics Engineering, Malaysia

All structures experience vibrations due to external dynamic force excitations, such as earthquakes and wind loadings. At resonance, the impact of this natural dynamic force on structures may lead to structural failures. Hence, an absorber is mounted to absorb vibrations from the primary system. Unfortunately, passive tuned mass absorbers can only target a single frequency. Since structural buildings possess multiple modes, an adaptive or tune-able vibration absorber is needed to attenuate the vibration in a multi-degree of freedom (MDOF) system. In this work, an adaptive electromagnetic vibration absorber (AEMVA) is proposed to eliminate the effects of vibrations and is dynamically tuned using electromagnets. By varying the current supplied to the coil, the stiffness of the AEMVA can be adjusted, resulting in a varying absorber frequency. A mathematical description of the AEMVA on a three-story prototype model building is also presented. The three-story benchmark model was used to demonstrate the effectiveness of AEMVA in absorbing multiple vibration modes, both analytically and experimentally. It is shown that 68.81 %, 50.49 %, and 33.45 % of vibration amplitude reductions were achieved at the first, second, and third modes, respectively.
Keywords: adaptive vibration absorber, electromagnetic vibration absorber, multimode system, dynamic modelling, structural vibration control

Highlights
- *A dynamic system AEMVA with a variable natural frequency was proposed to absorb the vibration of a multi-degree of freedom system.*
- *The basic theory and design for AEMVA were derived.*
- *Experimental analysis was carried out using a benchmark model of a three-story building.*
- *Tuning of the dynamic system proved successful in reducing the amplitude of the vibrations.*

0 INTRODUCTION

Three decades ago, fewer skyscrapers existed. Due to limited spaces and resources, buildings are now often built with a higher number of levels. However, high-rise buildings are prone to vibrations, such as wind-induced vibrations, causing excessive deflections and massive failures. Since high-rise buildings possess multiple modes of natural frequency, a tuneable-dynamic vibration absorber should be opted to eliminate unwanted vibrations.

In suppressing structural vibrations, passive control devices utilizing liquid or solid masses are widely studied. Lumped masses were used for bridge piers with improved efficiency of 25 % [1], liquid column-based dampers were used for structural control with effective results [2], and new damping methods were introduced for closely spaced natural frequencies for an enhanced accuracy damping technique [3]. Liquid-based dampers were introduced for controlling seismic vibrations for short-period structures [4], while wind-induced vibrations were also analysed for control in flexible structures [5]. The required damping level is tuned by adjusting the mass

of the liquid or solid based on the external excitations. Some devices were studied and designed for vibration suppression through variations of stiffness. Shape memory helical springs [6] were studied and enhanced for super-elastic shape memory helical springs [7], which were enhanced further to temperature-adjusted shape memory helical springs [8], and alloy pounding controlled dampers [9]. Magnetorheological elastomers [10] were also studied, and an attenuation controller was tested [11] for the practicality of the application, which was then enhanced to make use of conical magnetorheological elastomer isolators [12]. Gyro effects had been studied for a cantilever beam vibration isolation [13], and the technology was utilized in designing an intelligent glove for the suppression of Parkinson's disease effects [14], all of which were proven beneficial in controlling vibrations. Apart from being heavy [15], these types of absorbers work well only in narrow frequency bands [16]. Also, the system parameters might deteriorate due to wear, environmental, and operational conditions [17].

Magnetorheological fluids were introduced as a viable solution for the development of controllable dampers and were extensively used in many

*Corr. Author's Address: Department of Mechanical and Industrial Engineering, College of Engineering, Qatar University, Doha, Qatar, drasan@qu.edu.qa

191

applications for damping. In addition to having nonlinear hysteretic forces [18], recent studies show a maximum vibration reduction of 35 % to 37.2 % when the absorber is mounted on the first floor of a three-story building which was tested for a magnetorheological damper for earthquake-induced vibrations [19] and was enhanced to include neural networks [20], which were later enhanced further to include an intelligent bi-state controller [21], which proved beneficial but left room for improvements. Therefore, it is challenging to create high-efficiency magnetorheological (MR) fluid dampers that take advantage of the fluid features.

To overcome these issues, a vibration absorber capable of tuning its natural frequency in a wide frequency band, especially in a structure with multiple degrees of freedom, should be implemented. The force behaviour should be modelled and fully controlled with an understandable non-complex model to achieve high efficiencies exceeding the methods previously mentioned and be straightforward with fabrication.

In this work, the stiffness of the absorber is varied using electromagnetic coils. Variations in the current level applied to the magnetic coils directly influence the value of the generated magnetic field [17] and [22]. As a result, the damper's stiffness changes accordingly, thus changing the absorber's frequency to match the multimode structure's frequency. This allows for a damper that is suitably controlled for a wide frequency band.

1 ADAPTIVE VIBRATION ABSORBER USING ELECTROMAGNETS

A three-story building prototype model is used in this work; the floors were made of aluminium, and side support beams were made of stainless steel. Fig. 1 shows the prototype and schematic diagram, respectively. Stainless steel supporting columns are used, and equivalent stiffness for each floor can be modelled using Eqs. (1) and (2):

$$k_c = \frac{12EI}{L^3},\qquad(1)$$

$$I = \frac{bd^3}{12},\qquad(2)$$

where k_c is the stiffness for each column, and since we have four columns for each floor connected in parallel, the effective stiffness for each floor is equal to $4k_c$. I is the moment of inertia, E is the modulus of rigidity for stainless steel, b is the width for each column, d is the thickness of each column, and L is the length of each column. The stiffness around each floor
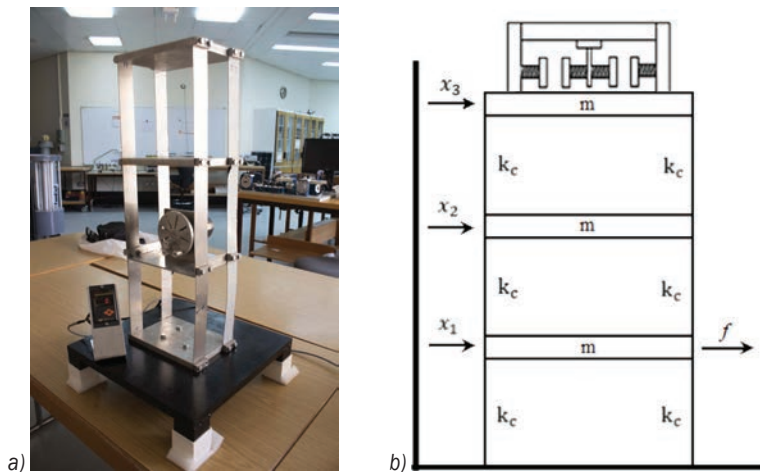
Fig. 1. *a) 3-story building model, b) schematic of the absorber/3-story building*

Table 1. *Properties of building model*

Floors (aluminium)		Columnal supports (Stainless steel)	
Length of each floor	200 mm	Length of each column	200 mm
Width of each floor	150 mm	Width of each column	40 mm
Thickness of each floor	15 mm	Thickness of each column	1 mm
Mass of each floor	1.50 kg	Modulus of elasticity	200 GPa
Density of aluminium	2.7×10^{-6} kg·mm^{-3}	Stiffness for each column	1 N/mm

Mohamed, K.S. – Amri, F. – Elboraey, M. – Nordin, N.H.D. – Muthalif, A.G.A.

is obtained using Eqs. (1) and (2), and the properties are given in Table 1.

The adaptive electromagnetic vibration absorber (AEMVA) mounted on top of the three-story building model studied in this work is shown in Fig. 1b. Four electromagnets and a prototype model of a three-story building Fig. 1b were used to study the efficiency of the AEMVA to absorb the vibration of the structure. The equation of motion for the structure can be represented in Eq. (3):

$$\mathbf{M}\ddot{x} + \mathbf{C}\dot{x} + \mathbf{K}x = \mathbf{f}, \tag{3}$$

where $\mathbf{M}$ is the mass matrix, $\mathbf{C}$ is the damping matrix, $\mathbf{K}$ is the stiffness matrix, and $\mathbf{f}$ is the force function. For this project, any damping coefficients are neglected, and hence Eq. (4) summarizes the coefficients for Eq. (3).

$$\begin{bmatrix} m_1 & 0 & 0 & 0 \\ 0 & m_2 & 0 & 0 \\ 0 & 0 & m_3 & 0 \\ 0 & 0 & 0 & m_a \end{bmatrix} \begin{bmatrix} \ddot{x}_1 \\ \ddot{x}_2 \\ \ddot{x}_3 \\ \ddot{x}_a \end{bmatrix} +$$

$$+ \begin{bmatrix} k_1+k_2 & -k_2 & 0 & 0 \\ -k_2 & k_2+k_3 & -k_3 & 0 \\ 0 & -k_3 & k_3+k_a & -k_a \\ 0 & 0 & -k_a & k_a \end{bmatrix} \begin{bmatrix} x_1 \\ x_2 \\ x_3 \\ x_a \end{bmatrix} = \begin{bmatrix} f_1 \\ 0 \\ 0 \\ 0 \end{bmatrix}, \tag{4}$$

where $\ddot{x}$ is the acceleration, and x is the horizontal displacement of the building. Subscripts 1, 2, and 3 represent the floor of the building, and subscript a refers to the absorber, making m_a the mass of the AEMVA absorber. In addition, m is the floor mass, and k denotes the stiffness. Each floor's mass and stiffness coefficients are as summarized in Table 1, while the absorber's mass m_a and stiffness coefficient k_a are to be examined in Section 3 for the proper tuning of the absorber.

2 ADAPTIVE ELECTROMAGNETIC VIBRATION ABSORBER MODELLING AND DESIGN

For the magnetic field at a point P with a distance D outside a ring of wire with radius R, the magnetic field from a small wire segment at the top of the ring can be modelled.

$$\mathbf{d\vec{B}} = \frac{\mu_0 I_{encl.}}{4\pi} \frac{\mathbf{d\vec{x}}}{D^2 + R^2} \frac{R}{\sqrt{D^2+R^2}}. \tag{5}$$

Use Fig. 2 and Eq. (5) after accounting for the opposite vertical field directions. $I_{encl.}$ is the current supplied $I_{supp.}$ multiplied by the number of coils used.

By integrating the magnetic field over all the small segments of the coil $d\vec{x}$, where the integration is the circumference of the circle, Eq. (6), the total field for a single loop at point P would arise [23].

$$\vec{\mathbf{B}}_{\text{single loop}} = \frac{\mu_0 I_{encl.}}{2} \frac{R^2}{\left(D^2+R^2\right)^{\frac{3}{2}}}. \tag{6}$$

Eq. (6) represents the magnetic field strength for a single wire turn. For a solenoid integrating over all the coil turns is required, Fig. 2 is used.
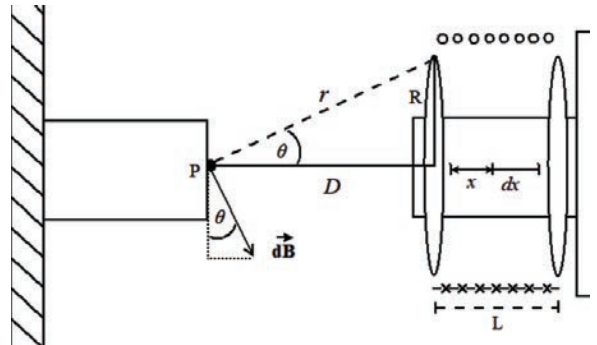
Fig. 2. *Mathematical model representation for the damper*

Rewriting Eq. (6) to include the previous findings gives Eqs. (7) and (8), where n is the number of coils per unit length of the solenoid.

$$I_{encl.} = I_{app.}\, n\, dx \tag{7}$$

$$\vec{\mathbf{B}}_{\text{total}} = \frac{\mu_0 I_{app.} n dx}{2} \frac{R^2}{\left(\left(D+x\right)^2 + R^2\right)^{3/2}}, \tag{8}$$

integrating across the limits of x which is the length over the solenoid we obtain Eq. (9):

$$\vec{\mathbf{B}}_{\text{Total}} = \frac{\mu_0 I_{app.} n}{2} \times \left[\frac{D+L}{\sqrt{\left(D+L\right)^2+R^2}} - \frac{D}{\sqrt{D^2+R^2}} \right]. \tag{9}$$

For the force between the two nearby aligned electromagnets, we can use the Magnetic-Charge model to model the force from one magnet to the other as in Eq. (10):

$$F_{repulsion} = \frac{\vec{\mathbf{B}}_{\text{Total}} A}{2\mu_0}. \tag{10}$$

Modelling the electromagnets as a spring so forces can be modelled using Fig. 2 and Eq. (11):

$$F_{repulsion} = k_a \times D, \tag{11}$$

where D is the distance between the two electromagnets.

This gives Eq. (12) for the semi-spring constants:

$$k_a = \frac{A}{2\mu_0 \cdot \Delta x} \frac{\mu_{Carbon\ steel\ core} I_{app.} n}{2} \times$$

$$\times \left[\frac{D+L}{\sqrt{(D+L)^2 + R^2}} - \frac{D}{\sqrt{D^2 + R^2}} \right]. \quad (12)$$

We also have two springs connected to the mass in the middle, which means they are connected in parallel, and the equivalent stiffness we are looking for is $2k_a$ which gives Eq. (14) for all three vibration modes as follows, making use of Eq. (13) for the

natural frequency using the mass and the stiffness, and hence our unit for the natural frequencies is in radians per second:

$$\omega_n = \sqrt{\frac{k_{equivalent}}{m}}. \quad (13)$$

The final equation used for the natural frequencies of the system is Eq. (14); the physical parameters and properties of electromagnets are summarized in Table 2, and an iron core can be seen in Fig. 3a and b, which shows the full assembled absorber. The design was meant to maximize the repulsion force between two electromagnets of opposite polarity opposing each other.

$$\omega_n = \sqrt{\frac{\frac{A}{\mu_0 \cdot \Delta x} \frac{\mu_{Carbon\ steel\ core} I_{app.} n}{2} \left[\frac{D+L}{\sqrt{(D+L)^2 + R^2}} - \frac{D}{\sqrt{D^2 + R^2}} \right]}{m_{absorber}}}. \quad (14)$$

Table 2. *Electromagnets properties*

Electromagnets (Carbon steel)			
Inner diameter	15 mm	Diameter of copper coil	5 mm
Outer diameter	30 mm	Number of coils	300
Length of core	24 mm	Mass of each core	150 g
Thickness of outer layer	4 mm	Range of current supplied	0 A to 3 A
Relative magnetic permeability	100		
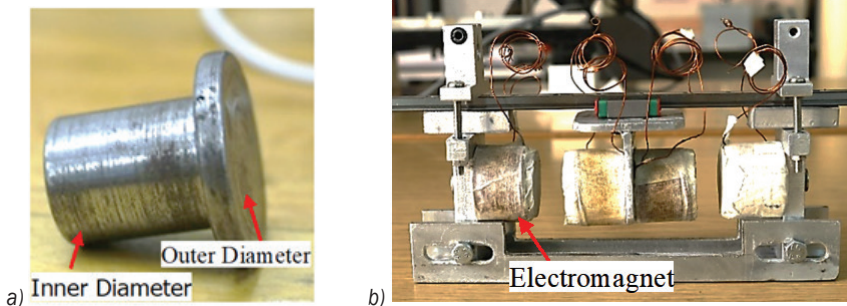
Fig. 3. *a) Electromagnetic core, and b) AEMVA model*

3 SIMULATION STUDIES
OF ELECTROMAGNETIC VIBRATION ABSORBER (AEMVA)

Simulation studies were conducted for the system's response with and without the absorber. The parameters in the simulation studies are listed in Tables 1 and 2. Using Eq. (4), the natural frequencies of the three-story building are shown in Table 3.

An excitation input was applied to the building and based on Eq. (4), the response of the first floor at three modal frequencies was observed. Without an absorber, the displacement of the first floor is displayed in Fig. 4. Mode shapes at each nodal frequency are also shown in Fig. 5. Likewise, Fig. 6 shows the first floor's responses at three natural frequencies when the absorber is tuned to absorb each frequency. Frequencies are given in Hz, and
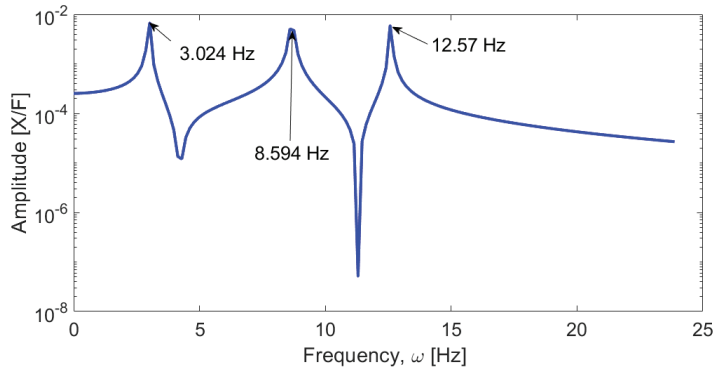
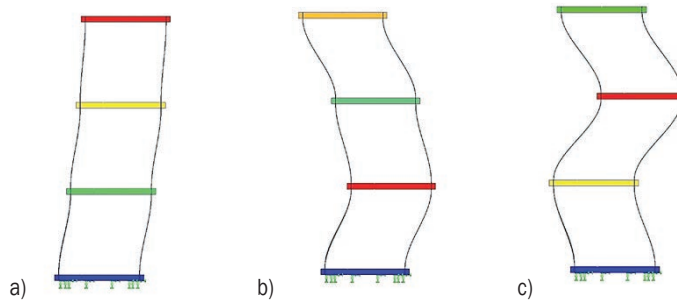**Fig. 4.** *Frequency response of the building model without absorber*

Fig. 5. *a) Mode shape of the first resonant frequency, b) mode shape of the second resonant frequency, and c) mode shape of the third resonant frequency*

amplitude is given in-floor displacement per unit force of excitation.

The simulation results show that with proper tuning of the electromagnetic stiffness, the AEMVA can effectively be used to reduce the vibration response of the structure.

4 EXPERIMENTAL SETUP

An experimental setup used to implement the AEMVA is shown in Fig 7. An accelerometer is attached to the third floor of the building model to measure the acceleration signal resulting from the vibration. This acceleration signal is used to construct the fast Fourier transform (FFT) diagrams and used to construct the amplitude-time signal for any time-domain analysis required.

An exciter consisting of a motor and an unbalance disk is mounted on the first floor of the building to exert the force needed to excite the building. The plate used for the first floor had a thickness of 5 mm to account for the weight of the exciter. A speed controller was used to adjust the motor's rotating frequency. The absorber was mounted atop the building, and power supplies used were connected to the electromagnets for the current variation as required. The polarity

for each electromagnet was adjusted so the two electromagnets facing each other repel.

A Dewesoft Sirius Modular data acquisition system and software were used to acquire and process the accelerometer signals. The whole setup was mounted on a heavy steel plate for proper structure grounding, as in Fig. 7.

5 EXPERIMENTAL RESULTS

The effect of attaching AEMVA to the structure at the three resonant frequencies after adjusting the magnetic field to provide the necessary stiffness is shown in Fig. 8. The frequency response function of the building model is shown in Fig. 9. The current supplied to each electromagnet for each mode is shown in Table 3.

Table 3. *Theoretical and experimental resonance and current combinations*

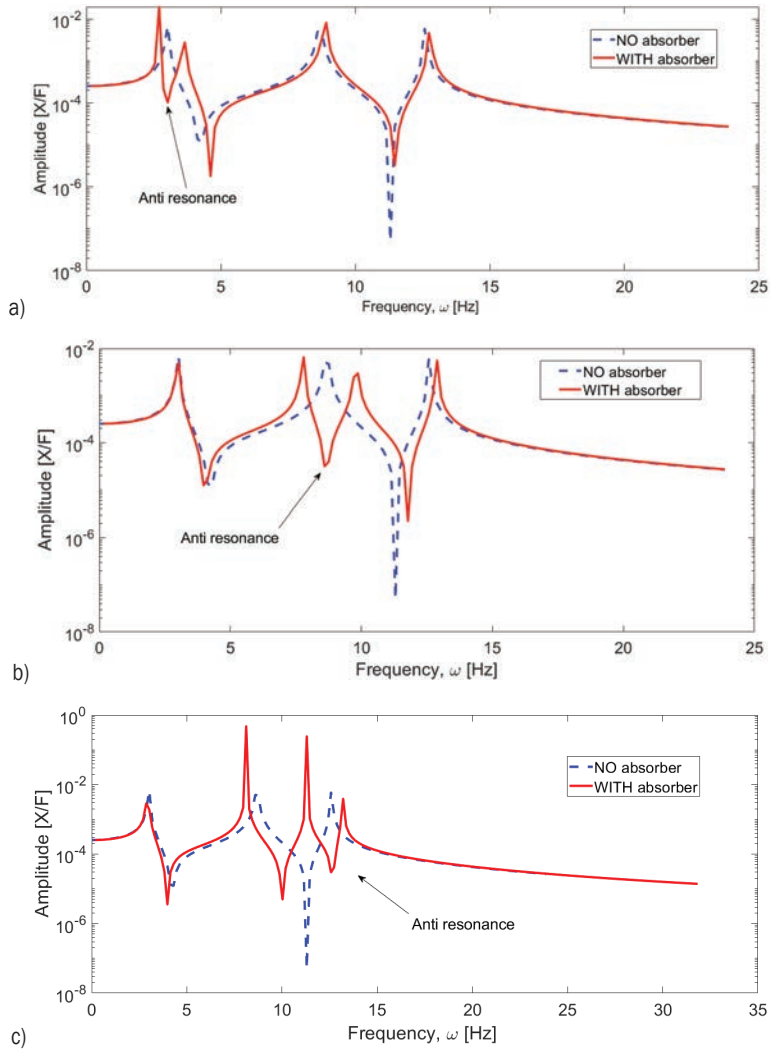| Modes	Theoretical resonant frequency ω_n [Hz]	Experimental resonant frequencies ω_n [Hz]	Current supplied [A]
First	3.024	2.42	1.80
Second	8.754	7.66	2.60
Third	12.570	12.10	3.00

Fig. 6. *a) Anti-resonance of the first mode, b) anti-resonance of the second mode, and c) anti-resonance of the third mode*
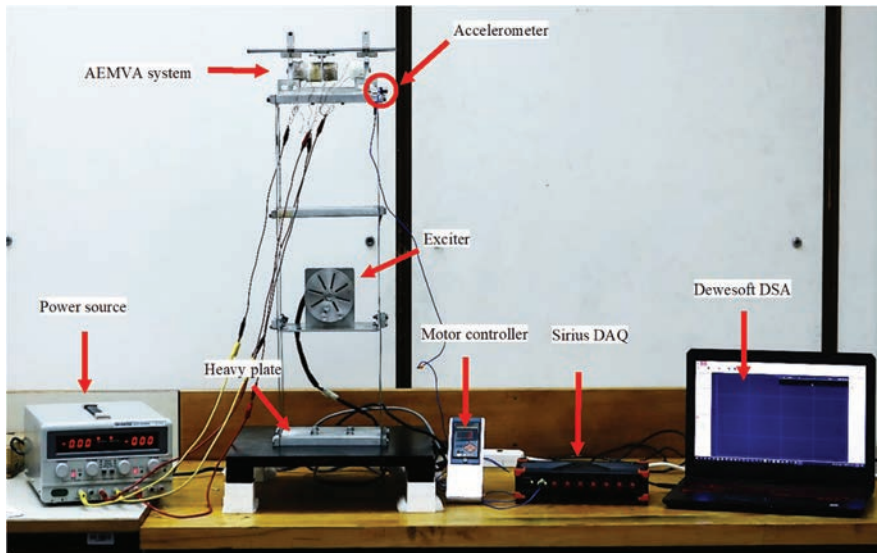
Fig. 7. *Experimental setup*
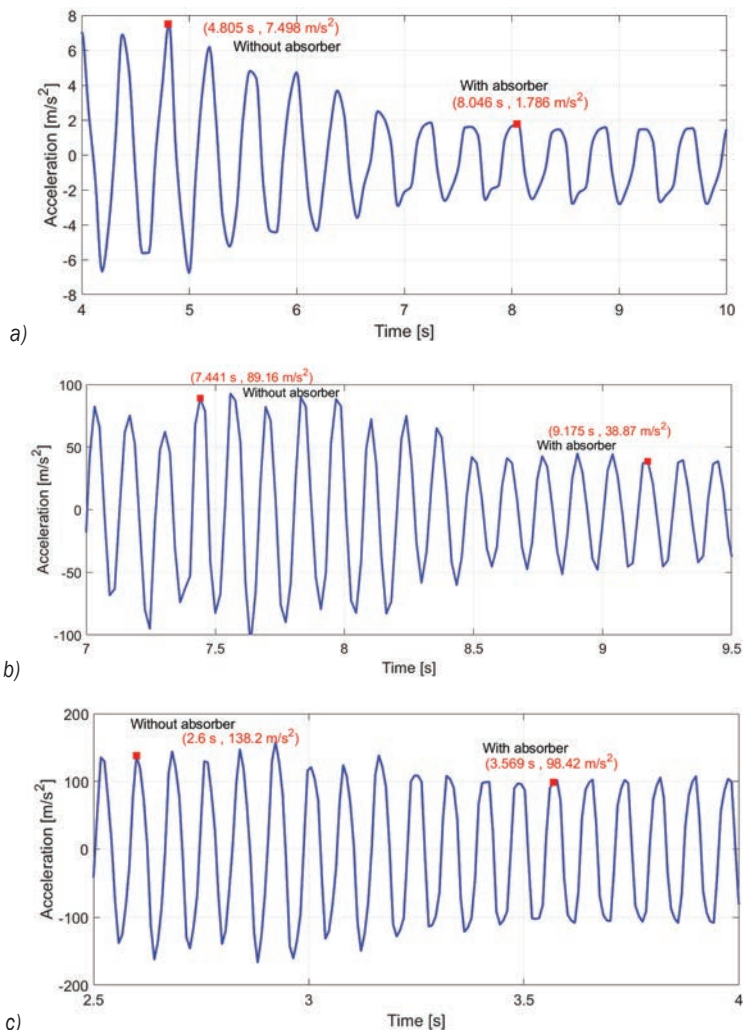
Fig. 8. *a) Performance of AEMVA at first mode with and without the absorber, b) Performance of AEMVA at second mode with and without the absorber, and c) Performance of AEMVA at third mode with and without the absorber*

Based on the summarized data in Table 4, Figs. 8 and 9, it is observed that the AEMVA successfully absorbs all three vibration modes. Three resonance frequencies at 2.42 Hz, 7.66 Hz, and 12.1 Hz had an amplitude attenuation of 68.81 %, 50.49 %, and 33.45 %, respectively. Notably, the third mode of frequency had a lower attenuation than the other two modes. This is due to the rapid vibration that resulted in the absorber colliding with the side electromagnets due to the small distance between them. The performance of the AEMVA at the third mode can be improved by increasing the current supplied to each electromagnet while increasing the distance between the electromagnets. This will result in a smoother oscillation without any collision but will cause excessive heating on electromagnets. The

general trend is that reducing the distance between the two electromagnets or increasing the current increases the stiffness coefficient. However, the distance cannot be minimal for any effective oscillation to occur; thus, experimenting with the current-distance combination can prove effective.

6 CONCLUSION

This research used an AEMVA to reduce the vibrations on a three-story building prototype model. Both simulation and experimental studies are presented in this work. By tuning the AEMVA, it is shown that the vibrations of the building floors were reduced due to the variations of the magnetic flux/stiffness. The tuning of AEMVA was achieved by changing
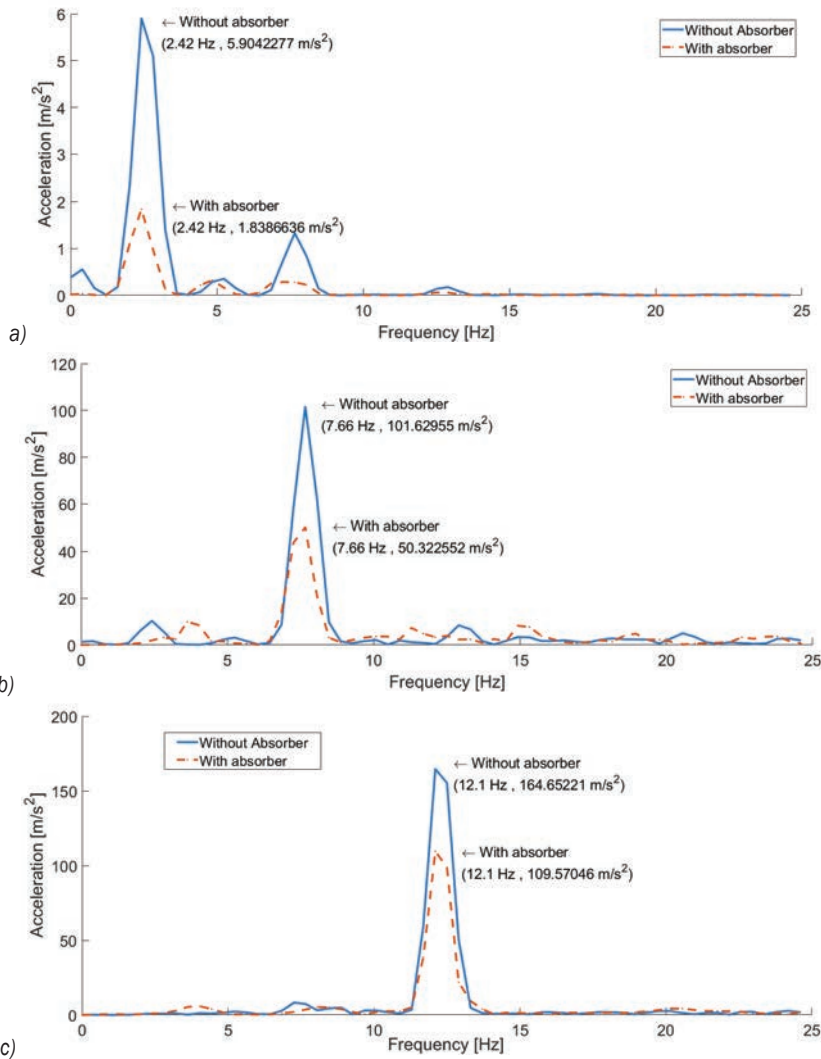
Fig. 9. *a) Frequency response function at first mode, b) frequency response function at second mode, and c) frequency response function at second mode*

Table 4. *AEMVA performance at the resonant frequency*

Modes	Resonant frequencies [Hz]	Vibration amplitude without AEMVA [m/s²]	Vibration amplitude with AEMVA [m/s²]	Attenuation amplitude [m/s²]	Attenuation [%]
First	2.42	5.90	1.84	4.06	68.81
Second	7.66	101.63	50.32	51.31	50.49
Third	12.10	164.65	109.57	55.08	33.45

the current supply to each electromagnet to match the resonance frequencies of the model. Both simulation and experimental results show that a single absorber can suppress the effect of vibration at a multi-modal structure.

One point of interest is the slight shift in frequencies between the theoretical and experimental results and the attenuation, which was almost 100 % for all modes in the theoretical results. The frequency

shift is explained by how the theoretical results were conducted without accounting for the weight of the absorber on top of the structure and the weight of the excitation motor, which decreases the natural frequencies of the model. The difference in amplitude attenuation comes from the already assumed negligent damping. The constant collision of the absorber and side electromagnets also causes a lower-than-expected percentage attenuation. This was mostly observed in

the third mode of vibration, where the absorber's mass had a higher displacing force due to the rapid structure vibration.

7 ACKNOWLEDGEMENTS

8 REFERENCES

[1] Hoang, T., Ducharme, K.T., Kim, Y., Okumus, P. (2016). Structural impact mitigation of bridge piers using tuned mass damper. *Engineering Structures*, vol. 112, p. 287-294, **DOI:10.1016/j.engstruct.2015.12.041**.

[2] Bhattacharyya, S., Ghosh, A.D. Basu, B. (2017). Nonlinear modeling and validation of air spring effects in a sealed tuned liquid column damper for structural control. *Journal of Sound and Vibration*, vol. 410, p. 269-286, **DOI:10.1016/j.jsv.2017.07.046**.

[3] Yuan, M., Sadhu, A., Liu, K. (2018). Condition assessment of structure with tuned mass damper using empirical wavelet transform. *Journal of Vibration and Control*, vol. 24, no. 20, p. 4850-4867, **DOI:10.1177/1077546317736433**.

[4] Pandey, D.K., Sharma, M.K., Mishra, S.K. (2019). A compliant tuned liquid damper for controlling seismic vibration of short period structures. *Mechanical Systems and Signal Processing*, vol. 132, p. 405-428, **DOI:10.1016/j.ymssp.2019.07.002**.

[5] Dai, J., Xu, Z.D., Gai, P.P. (2019). Tuned mass-damper-inerter control of wind-induced vibration of flexible structures based on inerter location. *Engineering Structures*, vol. 199, art. ID 109585, **DOI:10.1016/j.engstruct.2019.109585**.

[6] Lee, C.Y., Pai, C.A. (2016). Design and implementation of tunable multi-degree-of-freedom vibration absorber made of hybrid shape memory helical springs. *Journal of Intelligent Material Systems and Structures*, vol. 27, no. 8, p. 1047-1060, **DOI:10.1177/1045389X15581519**.

[7] Gao, N., Jeon, J.S., Hodgson, D.E., DesRoches, R. (2016). An innovative seismic bracing system based on a superelastic shape memory alloy ring. *Smart Materials and Structures*, vol. 25, no. 5, art. ID 055030, **DOI:10.1088/0964-1726/25/5/055030**.

[8] Huang, H., Chang, W.S. (2020). Re-tuning an off-tuned tuned mass damper by adjusting temperature of shape memory alloy: Exposed to wind action. *Structures*, vol. 25, p. 180-189, **DOI:10.1016/j.istruc.2020.02.025**.

[9] Ghasemi, M.R., Shabakhty, N., Enferadi, M.H. (2019). Vibration control of offshore jacket platforms through shape memory alloy pounding tuned mass damper (SMA-PTMD). *Ocean Engineering*, vol. 191, art. ID 106348, **DOI:10.1016/j.oceaneng.2019.106348**.

[10] Yang, J., Sun, S., Tian, T., Li, W., Du, H., Alici, G., Nakano, M. (2016). Development of a novel multi-layer MRE isolator for suppression of building vibrations under seismic events. *Mechanical Systems and Signal Processing*, vol. 70, p. 811-820, **DOI:10.1016/j.ymssp.2015.08.022**.

[11] Liao, G., Xu, Y., Wei, F., Ge, R., Wan, Q. (2017). Investigation on the phase-based fuzzy logic controller for magnetorheological elastomer vibration absorber. *Journal of Intelligent Material Systems and Structures*, vol. 28, no. 6, p. 728-739, **DOI:10.1177/1045389X16657417**.

[12] Wang, Q., Dong, X., Li, L., Ou, J. (2017). Study on an improved variable stiffness tuned mass damper based on conical magnetorheological elastomer isolators. *Smart Materials and Structures*, vol. 26, no. 10, art. ID 105028, **DOI:10.1088/1361-665X/aa81e8**.

[13] Ünker, F., Çuvalcı, O. (2019). Optimum tuning of a gyroscopic vibration absorber for vibration control of a vertical cantilever beam with tip mass. *International Journal of Acoustics & Vibration*, vol. 24, no. 2, p. 210-216, **DOI:10.20855/ijav.2019.24.21158**.

[14] Zulkefli, A.M., Muthalif, A.G.A., Nordin, N.H.D., Syam, T.M. (2019). Intelligent glove for suppression of resting tremor in Parkinson's disease. *Vibroengineering PROCEDIA*, vol. 29, p. 176-181, **DOI:10.21595/vp.2019.21078**.

[15] Davis, C.L., Lesieutre, G.A. (2000). An actively tuned solid-state vibration absorber using capacitive shunting of piezoelectric stiffness. *Journal of Sound and Vibration*, vol. 232, no. 3, p. 601-617, **DOI:10.1006/jsvi.1999.2755**.

[16] Elmali, H., Renzulli, M., Olgac, N. (2000). Experimental comparison of delayed resonator and PD controlled vibration absorbers using electromagnetic actuators. *Journal of Dynamic Systems, Measurement, and Control*, vol. 122, no. 3, p. 514-520, **DOI:10.1115/1.1286820**.

[17] McDaid, A.J. Mace, B.R. (2013). A self-tuning electromagnetic vibration absorber with adaptive shunt electronics. Smart Materials and Structures, vol. 22, no. 10, art. ID 105013, **DOI:10.1088/0964-1726/22/10/105013**.

[18] Truong, D.Q., Ahn, K.K. (2012). MR fluid damper and its application to force sensorless damping control system. *Smart Actuation and Sensing Systems - Recent Advances and Future Challenges*, **DOI:10.5772/51391**.

[19] Xu, Z.-D., Guo, Y.-Q. (2006). Fuzzy control method for earthquake mitigation structures with magnetorheological dampers. *Journal of Intelligent Material Systems and Structures*, vol. 17, no. 10, p. 871-881, **DOI:10.1177/1045389X06061044**.

[20] Xu, Z.-D., Shen, Y.-P., Guo, Y.-Q. (2003). Semi-active control of Structures Incorporated with magnetorheological dampers using neural networks. *Smart Materials and Structures*, vol. 12, no. 1, p. 80-87, **DOI:10.1088/0964-1726/12/1/309**.

[21] Xu, Z.-D., Shen, Y.-P. (2003). Intelligent bi-state control for the structure with magnetorheological dampers. *Journal of Intelligent Material Systems and Structures*, vol. 14, no. 1, p. 35-42, **DOI:10.1177/1045389X03014001004**.

[22] Gonzalez-Buelga, A., Clare, L., Neild, S., Burrow, S., Inman, D. (2015). An electromagnetic vibration absorber with harvesting and tuning capabilities. *Structural Control and Health Monitoring*, vol. 22, no. 11, p. 1359-1372, **DOI:10.1002/stc.1748**.

[23] Young, H.D., Freedman, R.A., Ford, A.L., Sears, F.W. (2014). 28.5 Magnetic Field of a Circular Current Loop. *Sears and Zemansky's University Physics: With Modern Physics*, p. 932-935, Pearson Education, San Francisco.

Statistical Modelling and Optimization of TIG Welding Process Parameters Using Taguchi's Method

S. Omprakasam[1,*] – K. Marimuthu[2] – R. Raghu[1] – T. Velmurugan[1]

[1]Sri Ramakrishna Engineering College, Department of Mechanical Engineering, India
[2]Coimbatore Institute of Technology, Department of Mechanical Engineering, India

This current research focuses on optimizing the welding process parameters and penetration of 5052 alloys using a TIG welding process based on the Taguchi methods. Process parameters such as current, voltage, and speed with three different levels were taken to form the L27 orthogonal array using the design of experiments. Analysis of variance, signal-to-noise ratio analysis, and regression analysis were performed. The regression analysis indicated that the developed model has greater adequacy in predicting the reinforcement form factor (RFF), penetration shape factor (PSF) and hardness of the weld specimens. In addition, the optimized parametric condition for the welded specimen was found to be current, voltage, and speed of 140 A, 18 V, and 300 mm/min, respectively.
Keyword: TIG welding; aluminium; AA5052; hardness; RFF; PSF; Taguchi

Highlights
- *The optimum conditions of current, voltage, and speed for attaining the maximum hardness of 145.3 HV while welding the AA5052 alloy have been determined.*
- *Among different parameters, current is found to have greater significance on RFF, PSF and hardness of the AA5052 alloy.*
- *The developed model is found to be adequate in correlating the process parameters with the RFF, PSF, and hardness of the welded specimens.*
- *Enhanced hardness is attained in the fusion zone of the welded AA5052 specimen.*

0 INTRODUCTION

Modern fabrication industries join metallic materials through melting the base materials with the addition of filler materials. Welding has been a high-quality and cost-effective method for producing strong joints in several applications. Many conventional joining processes are used in the fabrication sectors. Among them, the tungsten inert gas (TIG) welding process was one of the popular conventional welding processes, primarily employed in the automobile, oil, gas pipeline, and container manufacturing sectors [1]. This TIG welding process was most commonly used in the joining of aluminium alloys. In comparison to aluminium alloys, aluminium AA5052 alloy possesses better weldability and excellent corrosion resistance to seawater and salt spray, making it ideal for marine applications [2]. The TIG welding process was preferred over other process for joining 5xxx alloys due to its ease and low cost [3]. Dengkui et al. [4] revealed that applying different geometric shapes to a material changes its mechanical properties; they characterized the weld joints in terms of weld width, penetration depth, and reinforcement process profiles and found that the tensile strength was increased. Wan et al. [5] attempted to modify the weld geometry through multi-pass welding with swing-improved TIG for aluminium AA 2219 alloys. It was observed

that the joints with a tensile strength coefficient of 70 % and elongation over 4 % were acquired after weld geometry optimization. Aravind and Das [6] investigated welding aluminium 7075 alloy and found that the maximum welding strength achieved by optimizing the process parameters (100 A current, 60 mm/min welding speed, and 17 lit/min gas flow rate) was 130.27 MPa. Samiuddin et al. [7] investigated on the weldability of the Al-5083 alloy under the influence of different heat inputs (varied from 1 kJ/mm to 2 kJ/mm) in the TIG welding process. Tensile strength 18.26 % of datum strength was lost after welding from base material were compared. Joseph and Muthukumaran [8] investigated optimizing pulsed GTAW welding parameters for AISI 4135 powder metallurgy steel weld using a simulated and genetic algorithm and inferred that peak current of 80 A, base current of 35 A, welding speed 60 mm/min, and gas flow rate of 12 lit/min improved the tensile strength up to 685.31 MPa. Adalarasan and Santhanakumar [9] performed welding experiments on 6061 aluminium alloy based on Taguchi orthogonal L9 array and employed grey relational analysis to study the significance of the welding parameters. Input parameters including arc voltage (17 V to 24 V), current (160 A to 180 A), welding speed (90 mm/min to 110 mm/min), and gas flow rate (9 lit/h to 14 lit/h) were varied to determine the mechanical characteristics; it

was concluded that current has greater significance (47 %) over the mechanical properties followed by arc voltage (35 %). Kanakavalli et al. [10] investigated the effect of welding current, voltage, speed, and bevel angle in joining two dissimilar metals; it was observed that characteristics like tensile strength up to 405.62 MPa and hardness up to 150.4 HV was enhanced for the optimal parameter values of 150 A, 16 V, 0.94 m/min and 45°. Hazari et al. [11] studied the fracture behaviour of AA6082 and AA8011 butt-sweated joint deformation during tensile tests. As the intensity of current increased, the ultimate tensile strength was improved from 90.25 MPa to 170.25 MPa remarkably with a considerable increase in its yield strength. Kumar and Sundarrajan [12] approached Taguchi's technique to optimise pulsed TIG welding process parameters such as pulsed current (70 A to 80 A), base current (40 A to 50 A), welding speed (210 mm/min to 230 mm/min), and pulse frequency (2 Hz to 4 Hz) of AA 5456 aluminium alloy welds for improvement of 10 % to 15 % in mechanical properties. Shunmugasundaram et al. [13] performed friction stir welding on AA5052 with a Taguchi L9 orthogonal experimental array under the influence of tool rotational speed (650 rpm to 850 rpm), welding speed (20 mm/min to 40 mm/min), and tilt angle (1° to 2°). An optimized process parametric condition (tool rotational speed of 850 rpm, the welding speed of 20 mm/min, and the tilt angle of 2°) was found to obtain better mechanical properties in welded joints. ANOVA was performed to determine the percentage influence of the process parameters on the mechanical properties. Signal-to-noise (S/N) ratio analysis can be performed using the options such as smaller the better, nominal the better and larger the better , according to the desired response. The Taguchi method [14] to [17] allows the understanding of the influence of individual parameters on the materials' performance, i.e., microstructure and mechanical properties.

The present study aims to weld the AA5052 alloy through the TIG welding process parameters using the Taguchi method. Process parameters such as current, voltage, and speed were varied during the welding process to study their significance on enhancing the reinforcement form factor (RFF), penetration shape factor (PSF) and hardness. Analysis of variance (ANOVA), S/N ratio analysis, and regression analysis were also performed.

1 MATERIAL AND METHODS

AA5052 aluminium alloy was used in this experimental work as the parent material with plate thickness of 3.5 mm, length of 100 mm, and width of 100 mm. The parent material was welded with the TIG welding process using ER5356 filler material with a 2.4 mm diameter [18]. The chemical compositions of parent and filler material are listed in Table 1. The mechanical properties of the parent and filler material is given in Table 2. The TIG welding process focuses on the three essential parameters (welding current, voltage, and speed) which are generally considered for controlling weld quality and weldability characteristics [19]. Trials were carried out to select the upper and lower levels of the process parameters. A Taguchi L27 orthogonal array was selected, and the experiments were carried out accordingly. The TIG welding process parameters and their levels are shown in Table 3. The quality characteristics PSF, RFF and hardness of the parent material into the weld were evaluated for all the trials, and then ANOVA was carried out.

The applied criteria for the evaluation of PSF, RFF, and hardness are kept as larger-is-better. PSF defines the ratio of the width of the weld bead to the penetration height of weld. RFF is given by the ratio of weld bead width to reinforcement. An increase of RFF is obvious as the weld bead width decreases while reinforcement increases with heat input.

According to the ANOVA Tables 8 to 10, the input of the welding parameter and their interaction in influencing the characteristic of weld quality is evaluated [20]. The ANOVA also provides an indication of which welding parameters are statistically significant. The optimum welding parameter combination is estimated and proved. Welded specimens were taken, and the metallographic examination was carried out according to the ASTM E3 standard. A schematic illustration of weld bead is shown in Fig. 1. The macrograph of actual bead formation is shown in Fig. 2. The hardness of the welded specimens was measured as per the ASTM 384 standard [20] using a Vickers digital hardness testing machine [21].

Table 1. *Chemical composition of the base and filler material*

Elements	Si	Mn	Mg	Zn	Al
AA5052-H32	0.1	0.10	3.02	0.025	Bal.
ER 5356	0.052	0.11	3.33	0.069	Bal.

Table 2. *Mechanical properties of the base and filler material*

Material	Yield strength [MPa]	Tensile strength [MPa]	Hardness [HV]
AA5052-H32	160	230	61
ER 5356	198	295	-

Table 3. *Welding parameters*

Parameter	Unit	Factor Levels		
		1	2	3
Current	A	40	90	140
Voltage	V	10	14	18
Speed	mm/min	150	200	300
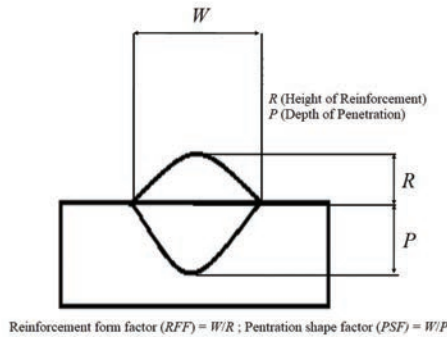
Fig. 1. *Schematic illustration of weld bead*

Fig. 2. *Macrograph of actual bead formation*

2 RESULTS AND DISCUSSION

In the following section, the statistical investigation of the RFF, PSF and hardness, signal-to-noise ratio analysis, analysis of variance, and regression analysis are discussed.

2.1 Statistical Analysis of RFF, PSF, and Hardness

RFF, PSF, and hardness obtained for the different experimental conditions are shown in Table 4. The maximum hardness of 145.3 HV 0.5 is a result of the RFF of 4.49 and PFF of 3.83 under current of 140 A, voltage of 18 V, and speed of 300 mm/min. The plots obtained for the corresponding RFF, PSF, and hardness are shown in Fig. 3. The main effect plot for RFF, PSF, and hardness is displayed for each level of individual parameter. From the RFF plot, it is observed that RFF becomes drastically increased when current is increased from 40 A to 140 A. The RFF is increased with increases in voltage slightly whereas there is only very minimal influence of speed in increasing the

RFF. The PSF plot showed that PSF is decreased when current is increased. PSF is decreased moderately with increases in voltage, whereas there is a only very minimal influence of speed in decreasing the PSF.

From the plot, it is inferred that hardness is increased drastically with increases in the current level, whereas a slight increase of hardness with respect to increases in voltage, and there is no significant increase with increase in speed. Overall, interaction plots show that a current of 140 A and voltage of 18 V have greater tendency to improve the hardness.

2.2 Surface Plot of RFF, PSF and Hardness

The surface plot for RFF, PSF, and hardness with respect to changes in the interaction of current and voltage is shown in Fig. 4. Surface plots with respect to current and voltage are only preferred for analysis since there is no significant influence of speed.

Table 4. *RFF, PSF and hardness obtained for the L27 orthogonal array*

S. No.	Current [A]	Voltage [V]	Welding speed [mm/min]	RFF	PSF	Hardness
1	40	10	150	2.08	5.7	103.2
2	40	10	200	2.16	5.8	104.5
3	40	10	300	2.1	5.65	108.5
4	40	14	150	2.15	5.62	106.3
5	40	14	200	2.27	5.42	109.5
6	40	14	300	2.39	5.45	111.4
7	40	18	150	2.2	5.82	114.5
8	40	18	200	2.31	5.89	115.2
9	40	18	300	2.26	5.92	116.7
10	90	10	150	2.37	6.13	118.3
11	90	10	200	2.45	6.11	120.4
12	90	10	300	3.16	6.09	122.4
13	90	14	150	3.11	5.82	124.5
14	90	14	200	3.25	5.68	123.8
15	90	14	300	3.26	5.47	126.9
16	90	18	150	3.55	5.59	128.5
17	90	18	200	3.62	5.35	130.5
18	90	18	300	3.59	5.45	132.4
19	140	10	150	4.06	4.87	134.6
20	140	10	200	4.12	4.61	136.5
21	140	10	300	4.15	4.72	137.4
22	140	14	150	4.12	4.66	139.2
23	140	14	200	4.01	4.14	140.3
24	140	14	300	4.39	4.28	141.3
25	140	18	150	4.45	4.25	142.6
26	140	18	200	4.6	4.12	143.2
27	140	18	300	4.49	3.83	145.3

a) Signal-to-noise: Larger is better

b) Signal-to-noise: Larger is better

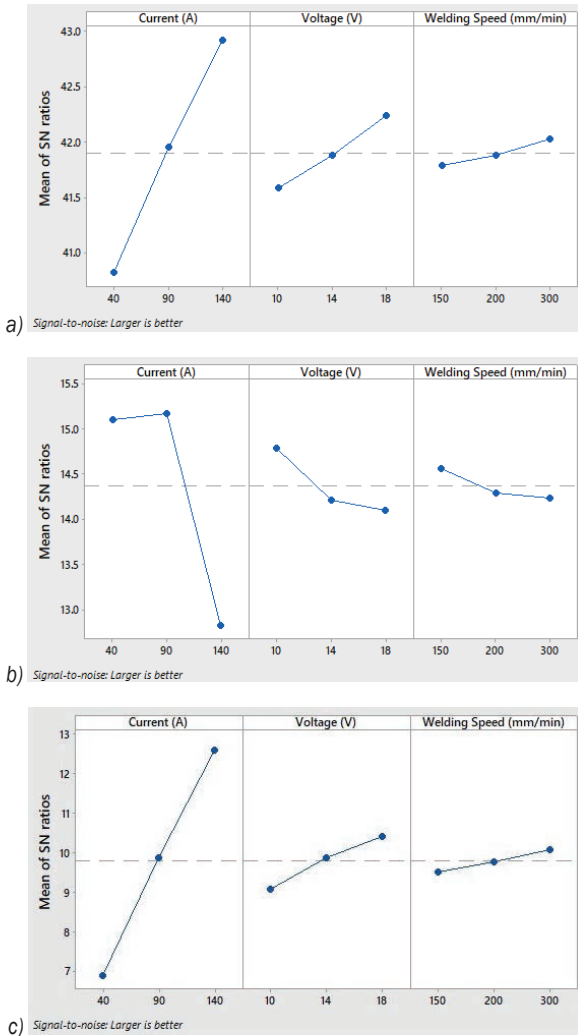c) Signal-to-noise: Larger is better

Fig. 3. *Main effect plot for a) RFF b) PSF and c) hardness*

The surface plot represents the three dimensional (3D) change of RFF, PSF, and hardness. It can be seen from Fig. 4a that the RFF increased drastically with the increase of the current and slightly with respect to changes in voltage. When the current is increased, the voltage is increased proportionally, which in turn deposits a higher amount of filler material for each unit of the weld length. With the high currents applied to each unit, the duration of the welding contributes to an extension of the width of the welding bead.

Fig. 4b shows the PSF decreased with increasing current and voltage. Figure 4c illustrates that the hardness of the fusion zone increased with increasing current and voltage. It is observed that hardness is influenced by high current (140 A) and high voltage (18 V). The increases in welding current and voltage, as well as other variables, were constant; an increase in hardness is evident. Notably, PSF graphs depict

the interaction between current and voltage. Here, the current and voltage increase tends to decrease the PSF.

a)

b)

c)
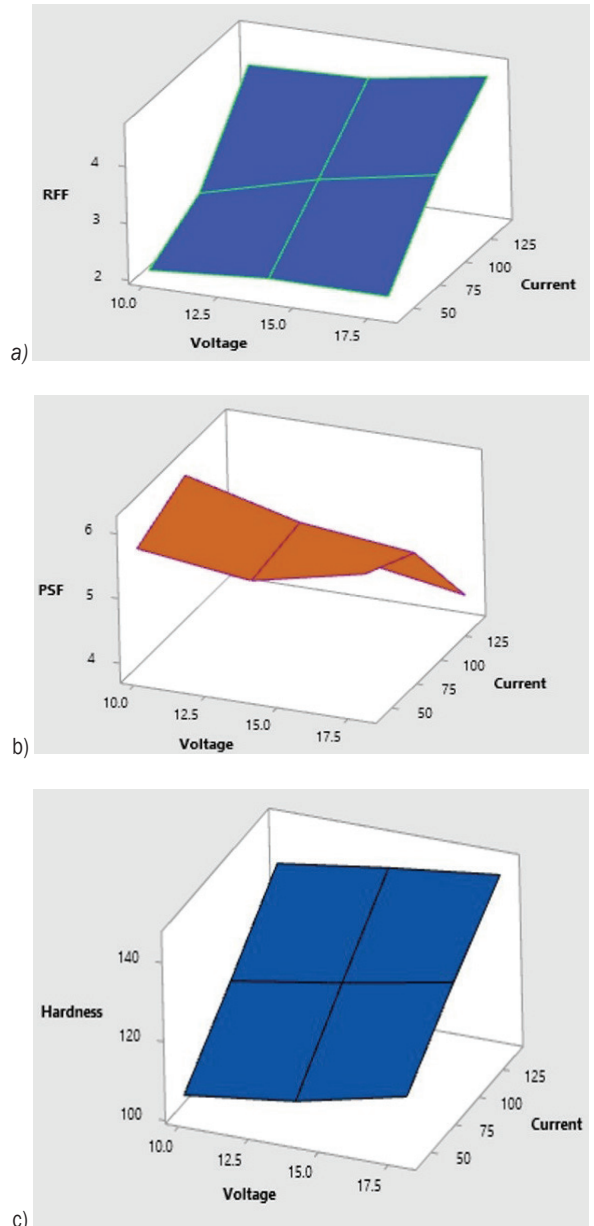
Fig. 4. *Surface plots for a) RFF, b) PSF, and c) hardness with respect to change in interaction of current and voltage*

2.3 Predicted Plot RFF, PSF and Hardness

The predicted plot for RFF, PSF, and hardness are shown in Fig. 5. Fig. 5a illustrates the predicted points are closed along with the residuals.

Fig. 5b shows that predicted points are scattered along with residuals, and Fig. 5c demonstrates that predicted points are correlated to residuals.
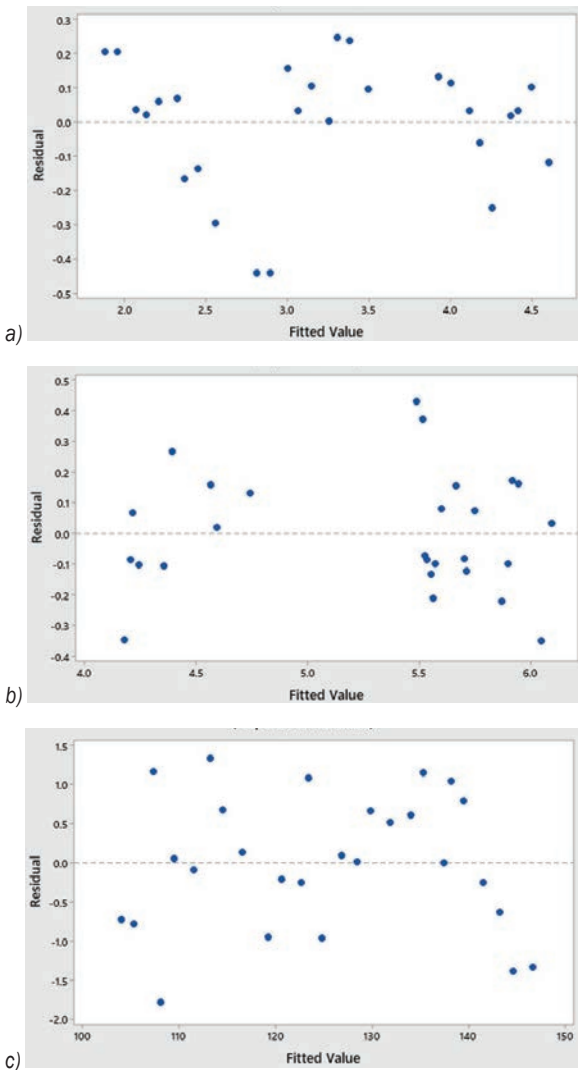
a)

b)

c)

Fig. 5. *Predicted plot for the a) RFF, b) PSF, and c) hardness*

2.4 Signal-to-Noise Ratio Analysis

The S/N ratio analysis is performed for "larger-is-better" option using Eq. (1), and a response is generated to estimate the influencing order of parameters on hardness. Tables 5 to 7 show the response table for S/N ratios of RFF, PSF, and hardness, respectively.

$$MSD = \frac{1}{n}\sum_{i=1}^{n}\frac{1}{y_i^2}, \qquad (1)$$

where *MSD* is the mean squared deviation, y_i the response of ith experiment value, and *n* replication number.

The delta value shows the variation in mean within levels, and the delta value is computed through subtracting the smallest from the largest value of the

signal-to-noise ratio. The delta value becomes higher, as there is greater variation of mean values. The factor with the highest delta value has more influence on the dilution and hardness. The delta value indicates the rank of the factors. It is observed from the delta value that current has major significance on RFF, PSF, and hardness, followed by voltage and speed.

Table 5. *Response table for S/N ratios of RFF (larger-is-better)*

Level	Current [A]	Voltage [V]	Speed [mm/min]
1	6.893	9.066	9.513
2	9.876	9.875	9.766
3	12.590	10.417	10.079
Delta	5.697	1.351	0.565
Rank	1	2	3

Table 6. *Response table for S/N ratios of PSF (larger-is-better)*

Level	Current [A]	Voltage [V]	Speed [mm/min]
1	15.11	14.79	14.57
2	15.17	14.21	14.29
3	12.82	14.10	14.24
Delta	2.35	0.69	0.33
Rank	1	2	3

Table 7. *Response table for S/N ratios of hardness (larger-is-better)*

Level	Current [A]	Voltage [V]	Speed [mm/min]
1	40.82	41.58	41.78
2	41.95	41.88	41.88
3	42.92	42.24	42.03
Delta	2.10	0.65	0.24
Rank	1	2	3

2.5 Analysis of Variance

The analysis of variance is performed for the significance level 5 % and confidence level 95% to evaluate the influence of various input process parameters on the RFF, PSF. and hardness, which is shown in Tables 8 to 10. The significance level indicates the confidence of repeatability of the experimental results. The percentage significance of the factors are determined and included in the last column. For RFF, current has the higher percentage of contribution (89.5 %) compared to voltage (5.13 %) and speed (0.77 %). For PSF, current also has the higher percentage of contribution (61.15 %) compared to voltage (5.27 %) and speed (1.13 %) and hardness; current also has greater influence (89.89%) compared to voltage (8.48 %) and speed (1.15 %).

Table 8. *Analysis of variance for RFF versus current, voltage, speed*

Source	Degree of freedom	Sequential Sum of square	Adjacent Sum of square	Adjacent mean square	F	% Contribution
Current	1	18.9523	18.9523	18.9523	455.77	89.5
Voltage	1	1.0854	1.0854	1.0854	26.10	5.13
Speed	1	0.1624	0.1624	0.1624	3.91	0.77
Error	23	0.9564	0.9564	0.0416		4.52
Total	26	21.1565				100

Table 9. *Analysis of variance for PSF versus current, voltage, speed*

Source	Degree of freedom	Sequential Sum of square	Adjacent Sum of square	Adjacent mean square	F	% Contribution
Current	1	7.7224	7.7224	7.7224	43.33	61.15
Voltage	1	0.6651	0.6651	0.6651	3.73	5.27
Speed	1	0.1422	0.1422	0.1422	0.80	1.13
Error	23	4.0995	4.0995	0.1782		32.46
Total	26	12.6293	7.7224	7.7224		100

Table 10. *Analysis of variance for PSF versus current, voltage, speed*

Source	Degree of freedom	Sequential Sum of square	Adjacent Sum of square	Adjacent mean square	F	% Contribution
Current	1	4068.02	4068.02	4068.02	4277.52	89.89
Voltage	1	383.64	383.64	383.64	403.40	8.48
Speed	1	52.02	52.02	52.02	54.70	1.15
Error	23	21.87	21.87	0.95		0.48
Total	26	4525.56	4068.02	4068.02		100

2.6 Regression Analysis with Confirmation Experiments

The regression equations are generated as per the influence of parameters indicated in the analysis of variance [22]. The regression equations for the RFF, PSF. and hardness are given in Eqs. (2) to (4), respectively.

$$RFF = 0.235 + 0.020522\ I + 0.0614\ U + 0.001238\ v_w, \qquad (2)$$

$$PSF = 7.356 - 0.01310\ I - 0.0481\ U - 0.00106\ v_w, \qquad (3)$$

$$Hardness = 77.05 + 0.30067\ I + 1.1542\ U + 0.02235\ v_w, \qquad (4)$$

where I is current parameter, U voltage parameter and v_w welding speed parameter.

These regression models relate the *RFF*, *PSF*, and *Hardness* of the welded specimens with the parameters such as current, voltage, and speed. In Eqs. (2) and (4), the parameter prefixed with the plus (+) sign indicates that increasing the level of that parameter increases *RFF* and *Hardness*. In Eq. (3), a minus (−) sign denotes that enhancing parameter level declines the responses. The sufficiency of the developed regression model has been confirmed by the confirmation experiments for *RFF*, *PSF*, and *Hardness*

of the welded specimens, shown in Tables 10 to 12. The new set of parametric conditions is incorporated in the developed model, and the determined *RFF*, *PSF*, and *Hardness* are checked with the experimental values for similar parametric conditions. The error [%] between model and experimental values has been computed, and it lies within the 5 % range. This, in turn, indicates that the developed regression model has greater adequacy in predicting the *RFF*, *PSF*, and *Hardness* of the welded specimens by connecting it with the process parameters.

Table 10. Regression analysis and confirmation experiments (*RFF*)

Current [A]	Voltage [V]	Speed [mm/min]	Experimental	Regression	Error [%]
90	10	150	2.52	2.61	3.5
120	14	200	3.86	3.80	1.5
150	18	300	4.61	4.78	3.6

Table 11. Regression analysis and confirmation experiments (*PSF*)

S. No.	Current [A]	Voltage [V]	Speed [mm/min]	Experi-mental	Regression	Error [%]
1	90	10	150	5.394	5.537	2.6
2	120	14	200	4.923	4.898	0.5
3	150	18	300	4.443	4.205	4.9

Table 12. *Regression analysis and confirmation experiments (Hardness)*

S. No.	Current [A]	Voltage [V]	Speed [mm/min]	Experimental	Regression	Error [%]
1	90	10	150	123.21	119.00	3.5
2	120	14	200	136.96	133.75	2.4
3	150	18	300	148.21	149.36	0.7

2.7.1 Microstructural Analysis

The microstructure of the AA5052 aluminium alloy weldment cross-section highlights the parent material (PM), fusion zone (FZ), and heat-affected zone (HAZ) were taken using an inverted metallurgical optical microscope. Fig. 6 shows an α-aluminium matrix in the PM. In Fig. 7, defects such as void, crack, and unbounded regions in and around the weld region for the weld are not observed [23] and [24]. In tungsten inert gas welds, grain development is evident on the weld site (fusion zone). This reveals elongated cellular dendritic grains with coarse Mg_2Si particles distributed in the α-aluminium matrix. The coarsening of grain reduces the strength of the fusion zone. The dendritic structure formed in the fusion zone depends on the cooling rate. As the heat input increased during the welding process, the cooling rate will be lower, which will result in the formation of coarser dendrites.
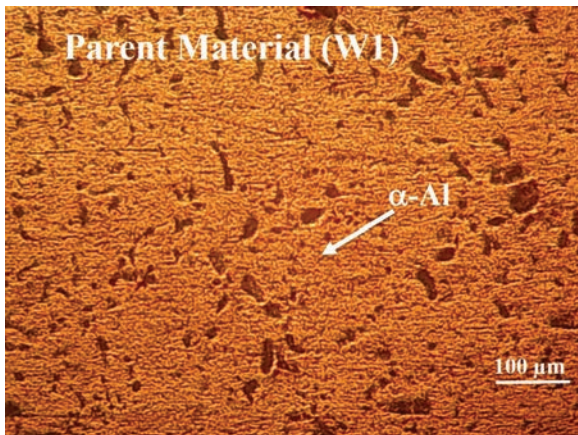

Fig. 6. *Parent materials*

Fig. 7. *Fusion zone of the different weldments a) 90 A, 10 V, 150 mm/min b) 120 A, 14 V, 200 mm/min, and c) 150 A, 18 V, 300 mm/min*

Fig. 8 shows the transition zone, i.e., fusion zone to the heat-affected zone for the three experimental conditions. The left portion of the microstructure indicates the dendritic formation in the fusion zone, and the right portion of the microstructure reveals the formation of equiaxed grains at the HAZ, which is commonly observed in the strain-hardened 5052-H32 alloy.
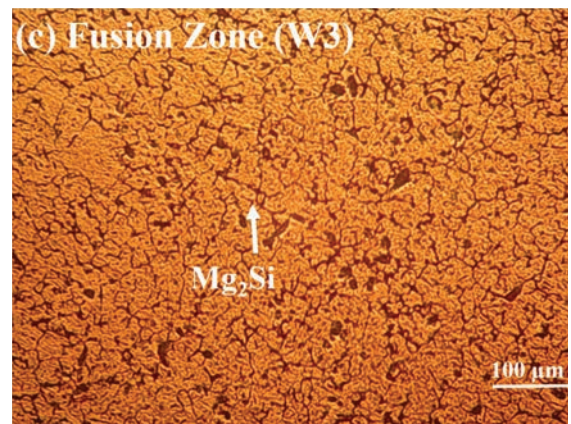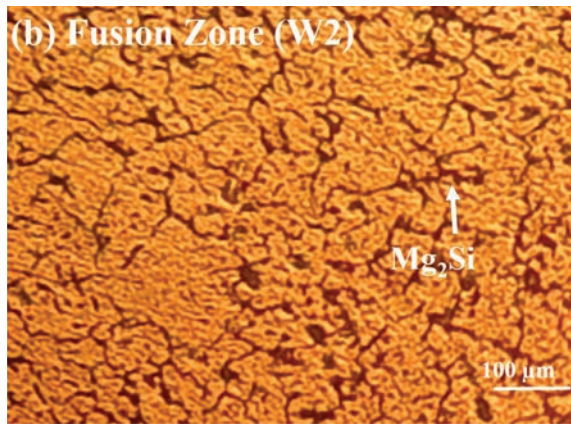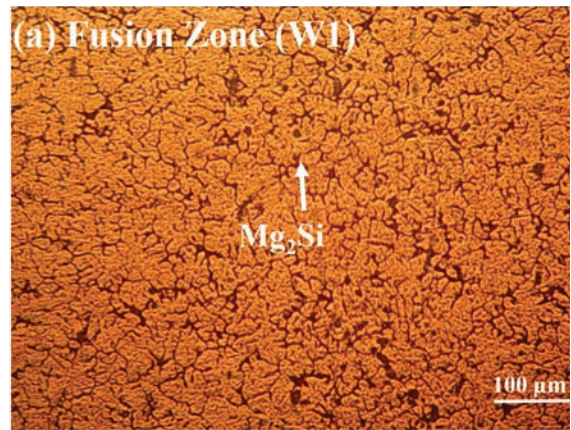
Fig. 9 shows the phase variation in the heat affect zone. This results from the high thermal conductivity of aluminium alloys, specifically at lower welding current, which leads to high thermal losses transverse in the welding directions. Fig. 10 presents the influence of the welding current (90 A, 120 A, and 150 A) on the phase variation (16.17µm, 9.53µm, and 7.54 µm) and grain size (102.014 µm, 116.429 µm,
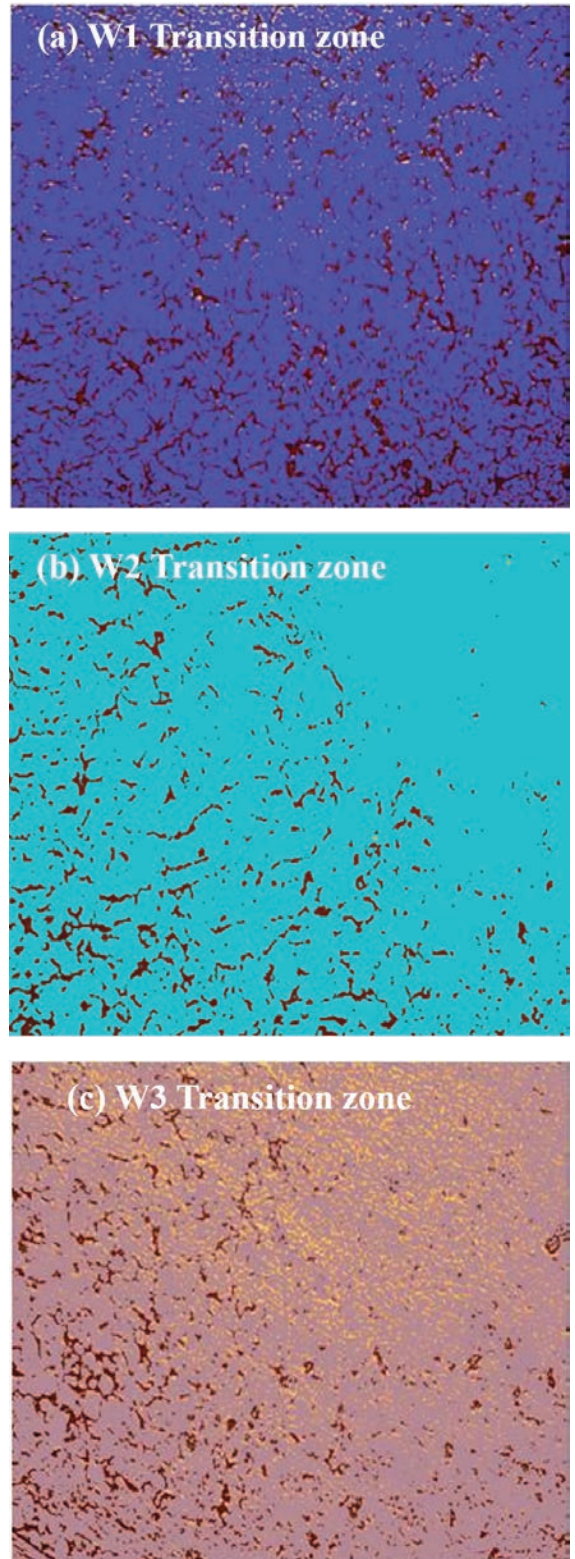
and 126.89 μm), respectively. As welding current increases, phase variation also decreases.
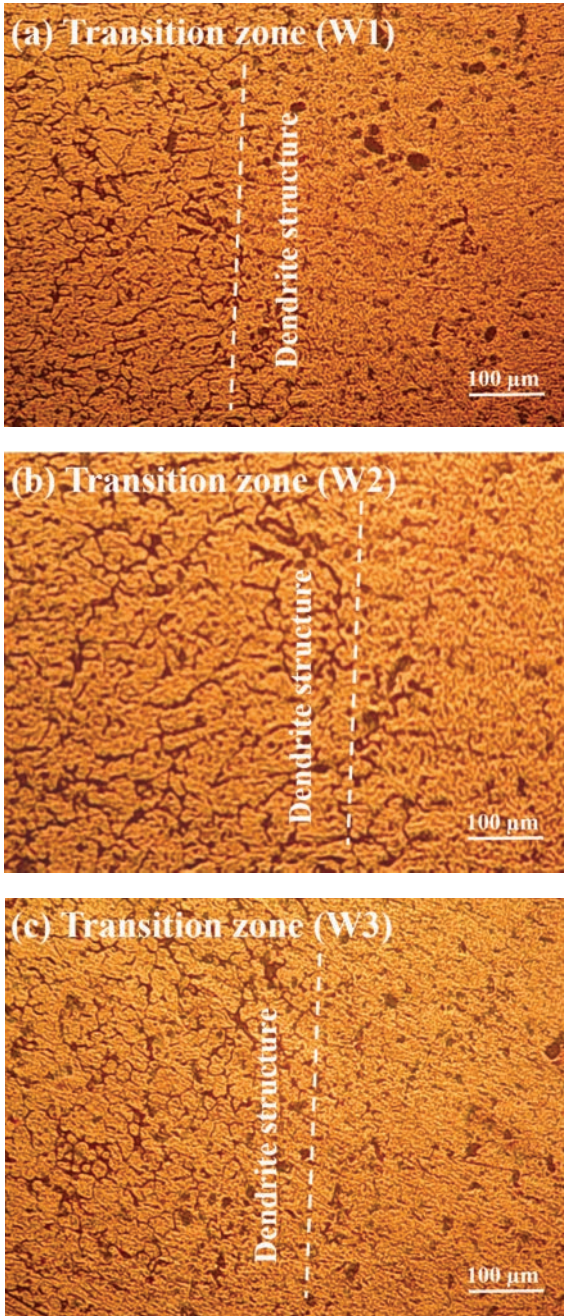
Fig. 8. *Transition zone of the different weldments a) 90 A, 10 V, 150 mm/min b) 120 A, 14 V, 200 mm/min and c) 150 A, 18 V, 300 mm/min*

2.7.2 Hardness Testing

The hardness profiles are studied in cross-section of weldments produced at confirmation experimental

Fig. 9. *Transition zone of the different weldments with partially phase variations a) 90 A, 10 V, 150 mm/min b) 120 A, 14 V, 200 mm/min, and c) 150 A, 18 V, 300 mm/min*
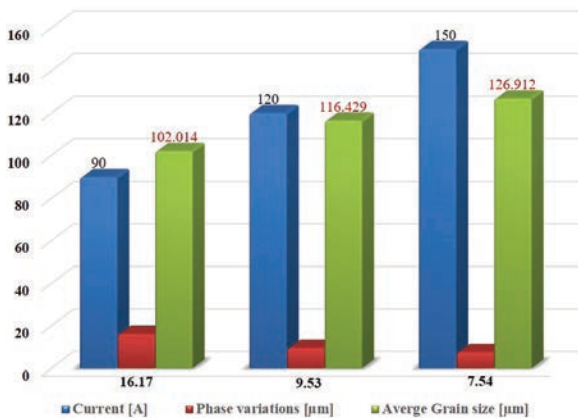
Fig.10. *Influence of welding current*

conditions, Fig. 11. Hardness is found lowest at the base material whereas the heat-affected zone is having relatively higher hardness than base metal. There is further increase in the hardness upon reaching the fusion zone. Overall, hardness gets increased from base metal towards the fusion zone. This trend across the zones is due to rapid cooling rate occurring in the HAZ and fusion zones. In addition, the higher hardness in the fusion zone owing to formation of Mg_2Si with a fine grain structure in weldment. Similar trend of microhardness across the different zones of the weldment is reported elsewhere [25].
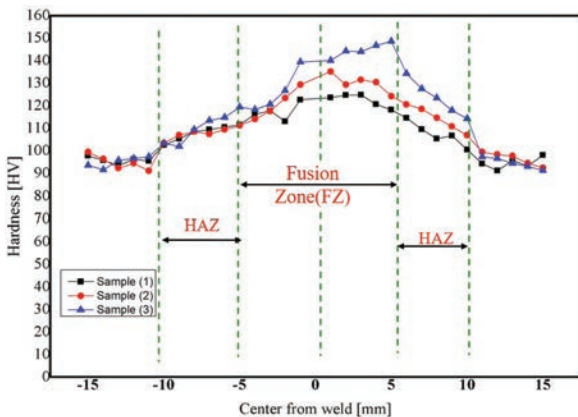

Fig. 11. *Hardness of the different zones welded for confirmation experiments*

3 CONCLUSION

- A study was conducted to determine appropriate welding process and produce a set of welding parameters for components used in marine applications, automobile structural applications, and chemical processing industries.

- AA5052 was successfully welded using tungsten inert gas welding process under L27 experimental array using Taguchi's method. Welding experiments revealed that, the maximum hardness of 145.3 HV 0.5 is resulted for the RFF of 4.49 and PFF of 3.83 under the current (140 A), voltage (18 V) and speed (300 mm/min).

- The RFF gets increased drastically when current is increased from 40 A to 140 A. PSF gets decreased moderately with increase in voltage whereas there is only very minimal influence of speed in decreasing the PSF. The hardness gets increased drastically with increase in current level whereas thre is slight increase of hardness with respect to increase in voltage and there is no significant increase with increase in speed. In overall, interaction plots evident that current of 140 A and voltage of 18 V has greater tendency to improve the hardness.

- S/N ratio and ANOVA showed that current has the major significance on RFF, PSF and hardness followed by voltage and speed. Regression analysis evident that developed model has greater adequacy in predicting the RFF, PSF and hardness of the welded specimens by connecting it with the process parameters.

- Defects such as void, crack, and unbounded regions in and around the weld region for the weld is not observed in the microstructure. The grain development is evident on the fusion zone. This reveal elongated cellular dendritic grains with coarse Mg_2Si particles distributed in the α-aluminium matrix.

- Hardness profile for the specimen welded at confirmation experimental conditions showed that hardness was found higher at fusion zone followed by heat-affected zone and base metal.

4 REFERENCES

[1] Balaram Naik, A., Chennakeshava Reddy, A. (2018). Optimization of tensile strength in TIG welding using Taguchi method and analysis of variance (ANOVA). *Thermal Science and Engineering Progress*, vol. 8, p. 327-339, **DOI:10.1016/j.tsep.2018.08.005**.

[2] Sathishkumar, D., Daniel Das, A. (2021). Investigations on effect of process parameters on GTAW of aluminium alloy welding using full factorial design technique. *Materials Today: Proceedings*, vol. 37, part 2, p. 621-626, **DOI:10.1016/j.matpr.2020.05.624**.

[3] Shanavas, S., Dhas, J.E.R., Murugan, N. (2018). Weldability of marine grade AA 5052 aluminium alloy by underwater friction stir welding. *The International Journal of Advanced*

Manufacturing Technology, vol. 95 p. 4535-4546, **DOI:10.1007/s00170-017-1492-6**.

[4] Denykui, Z., Wang, G., Wu, A., Zhao, Y., Li, Q., Liu, X., Meng, D., Song, J., Zhang, Z. (2018). Study on the inconsistency in mechanical properties of 2219 aluminium alloy TIG-welded joints. *Journal of Alloys and Compounds*, vol. 777, p. 1044-1053, **DOI:10.1016/j.jallcom.2018.10.182**.

[5] Wan, Z., Meng, D., Zhaom Y., Zhang, D., Wang, Q., Shan, J., Song, J., Wang, G., Wu, A. (2021). Improvement on the tensile properties of 2219-T8 aluminium alloy TIG welding joint with weld geometry optimization. *Journal of Manufacturing Processes*, vol. 67, p. 275-285, **DOI:10.1016/j.jmapro.2021.04.062**.

[6] Aravind, S., Das, A.D. (2020). An examination on GTAW samples of 7-series aluminium alloy using response surface methodology. *Materials Today*, vol. 37, no. 4, p. 1234-1248, **DOI:10.1016/j.matpr.2020.05.623**.

[7] Samiuddin, M., Li, J., Taimoor, M., Siddiqui, M., Siddiqui, S.U., Xiong, J. (2020). Investigation on the process parameters of TIG-welded aluminium alloy through mechanical and microstructure characterization. *Defence Technology*, vol. 17, no. 1, **DOI:10.1016/j.dt.2020.06.012**.

[8] Joseph, J., Muthukumaran, S. (2016) Optimization of pulsed current GTAW process parameters for sintered hot forged AISI 4135 P/M steel welds by simulated annealing and genetic algorithm. *Journal of Mechanical Science and Technology*, vol. 30, p. 145-155, **DOI:10.1007/s12206-015-1218-3**.

[9] Adalarasan, R., and Santhanakumar, M., (2015) Parameter design in fusion welding of AA 6061Aluminium alloy using desirability grey relational analysis (DGRA) method. *Journal of The Institution of Engineers (India): Series C*, vol. 96, p. 57-63. **DOI:10.1007%2Fs40032-014-0128-y**.

[10] Kanakavalli, P.B., Navaneeth Babu, B., Vishnu Sai, Ch.P.N. (2019). A hybrid methodology for optimizing MIG weling process parameters in joining of dissimilar metals. *Materials Today: Proceedings*, vol. 23, p. 507-512, **DOI:10.1016/j.matpr.2019.05.396**.

[11] Hazari, H.R., Balubai, M., Suresh Kumar, D., Ahsan Ul Haq, (2019). Experimental investigation of TIG welding on AA 6082 and AA 8011. *Materials Today: Proceedings*, vol. 19, p. 818-822, **DOI:10.1016/j.matpr.2019.08.137**.

[12] Kumar, A., Sundararajan, S. (2009). Optimization of pulsed TIG welding process parameters on mechanical properties of AA 5456 Aluminium alloy weldments. *Materials and Design*, vol. 30, no. 4, p. 1288 -1297, **DOI:10.1016/j.matdes.2008.06.055**.

[13] Shunmugasundaram, M., Praveen Kumar, A., Ponraj Sankar, L., Sivasankar, S. (2020). Optimization of process parameters of friction stir welded dissimilar AA6063 and AA5052 aluminum alloys by Taguchi technique. *Materials Today: Proceedings*, vol. 27, p. 871-876, **DOI:10.1016/j.matpr.2020.01.122**.

[14] Vora, J., Patel, V.K., Srinivasan, S., Chaudhari, R., Pimenov, D.Y., Giasin, K., Sharma, S. (2021). Optimization of activated tungsten inert gas welding process parameters using heat transfer search algorithm: With experimental validation using case studies. *Metals*, vol. 11, art. ID 981, **DOI:10.3390/met11060981**.

[15] Srirangan, A.K., Paulraj, S. (2016). Multi-response optimization of process parameters for TIG welding of Incoloy 800HT by Taguchi grey relational analysis. *Engineering Science and Technology*, vol. 19, no. 2, p. 811-817, **DOI:10.1016/j.jestch.2015.10.003**.

[16] Kasirajan, G., Sathish Rengarajan , Ashok kumar ,R., Raghav, G.R., Rao,V.S., and Nagarajan, K.J. (2020). Tensile and wear behaviour of friction stir welded AA5052 and AA6101-T6 aluminium alloys: effect of welding parameters, Metallurgical Research and Technology, vol. 117, no. 4, art. ID 405, **DOI:10.1051/metal/2020039**.

[17] Sathish, T., Tharmalingam, S., Mohanavel, V., Ashraff Ali, K., Karthick, S., Ravichandran, A., Rajkumar, M., Sivanraju (2021). Weldability Investigation and Optimization of Process Variables for TIG-Welded Aluminium Alloy (AA 8006). *Advances in Material Science and Engineering,* art. ID 2816338, **DOI:10.1155/2021/2816338**.

[18] Dhanaraj, A.P., Kumarasamy, S. (2021). Mechanical properties and metallurgical characterization of FSPed TIG and TIG welded AA5052-H32/AA5083-H111 dissimilar aluminium alloys. Metallurgical Research and Technology, vol. 118, art. ID 304, **DOI:10.1051/metal/2021005**.

[19] Safari, M., Mostaan, H. (2016). Experimental investigation of the effects of process parameters on the strength of eutectoid steel (AISI 1075) sheet resistance spot welds. Metallurgical Research and Technology, vol. 113, p. 305-318, **DOI:10.1051/metal/2016005**.

[20] Sudhakar,R., Sivasubramanian, R., Yoganandh, J. (2017), Effect of automated MIG welding process parameters on ASTM A 106 Grade B pipe weldments used in high-temperature applications. *Materials and Manufacturing Processes*, vol. 33, no. 7, p. 749-758, **DOI:10.1080/10426914.2017.1401719**.

[21] Skariya, P.D., Satheesh, M., Dhas, J.E.R. (2018). Optimizing parameters of TIG welding process using grey wolf optimization concerning 15CDV6 steel. *Evolutionary Intelligence*, vol. 11, p. 89-100, **DOI:10.1007/s12065-018-0161-5**.

[22] Radhika, N., Raghu, R. (2017). Investigation on mechanical properties and analysis of dry sliding wear behavior of Al LM13/AlN metal matrix composite based on Taguchi's technique. *Journal of Tribology*, vol. 139, no. 4, art. ID 041602, **DOI:10.1115/1.4035155**.

[23] Ebrahimzadeh, I., Sadeghi, B., Maddahi, H. (2019). Welding of thin sheet of Al5456 aluminium alloy by using GTA and GMA welding process. *Materials Research Express*, vol. 6, vol. 6, **DOI:10.1088/2053-1591/ab0d48**.

[24] Hagenlocher, C., Wellera, D., Weber, R., Graf, T. (2019), Reduction of the hot cracking susceptibility of laser beam welds in Al-Mg-Si alloys by increasing the number of grain boundaries. *Science and Technology of Welding and Joining*. vol. 24, no. 4, p. 313-319, **DOI:10.1080/13621718.2018.1534775**.

[25] Abioye,T.E., Zuhailawati,H., Aizad, S., Anasyida, A.S. (2019). Geometrical, microstructural and mechanical characterization of pulse laser welded thin sheet 5052-H32 aluminum alloy for aerospace applications. *Transactions of Nonferrous Metals Society of China*, vol. 29, no. 4, p. 667-679, **DOI:10.1016/S1003-6326(19)64977-0**.

Vsebina

Razširjeni povzetki (extended abstracts)

In Memoriam

Termomehanska analiza nepnevmatskega kolesa z upogljivimi naperami

Hongxun Fu – Xuemeng Liang – Yan Wang – Laiyun Ku – Zhen Xiao

Tehniška univerza v Shandongu, Šola za transport in avtomobilsko tehniko, Kitajska

V članku je predstavljen nov tip nepnevmatskega kolesa z upogljivimi naperami, zasnovan po metodi konfiguracije enot. Podrobno so preučene termomehanske lastnosti kolesa za določitev temperaturnega polja v stacionarnem stanju pri različnih delovnih pogojih.

V članku je uporabljena kombinirana metoda teoretičnih raziskav in eksperimentov. Na stroju za preizkušanje pnevmatik je bil opravljen preizkus prototipa kolesa in rezultati so bili primerjani z rezultati numerične analize. S tem je bila dokazana točnost numeričnega modela, na osnovi katerega je bila nato opravljena numerična analiza termomehanskih lastnosti kolesa.

Predstavljen je predlog metode konfiguracije enot za izgradnjo 3D-modela nepnevmatskega kolesa z upogljivimi naperami. Sledi analiza deformacij, energijskih izgub in prevoda toplote po metodi termomehanske sekvenčne sklopitve. Končno je določeno še temperaturno polje v stacionarnem stanju pri različnih delovnih pogojih.

Glavni rezultati in ugotovitve:

1. Visokotemperaturna področja na kolesu so koncentrirana v srednjem upogljivem delu naper, ki se ujema s področjem največjih napetostnih deformacij. Celotna temperatura postopoma upada od središča upogljive napere proti sosednjim delom. Glede na dejstvo, da je temperatura v središču upogljive napere previsoka, je čezmerno segrevanje naper mogoče zmanjšati z optimizacijo zgradbe enot. Članek podaja teoretične smernice za snovanje konstrukcije in optimizacijo nepnevmatskih koles.

2. Hitrost vožnje in vertikalna obremenitev vplivata na celotno in maksimalno temperaturo na kolesu. Obremenitev ima bistveno večji vpliv na temperaturne spremembe kot hitrost vožnje. Hitrost vožnje bi bilo tako mogoče povišati ob ustreznem zmanjšanju obremenitev, s tem pa bi razrešili problem visokotemperaturne odpovedi kolesa pri visokih hitrostih.

3. Rezultati študije kažejo, da je predstavljeno nepnevmatsko kolo z upogljivimi naperami primernejše za delovne pogoje z majhnimi obremenitvami in visokimi hitrostmi, zato se kolo bolje obnese na lahkih vozilih.

Zaradi omejitev pri preizkusih ni bilo mogoče pridobiti temperaturno odvisne krivulje napetosti-deformacije za material PU. Za poenostavitev analize je bilo privzeto, da temperatura ne vpliva na materialne lastnosti posameznih delov kolesa. V prihodnjih raziskavah bo preučen še vpliv temperature na lastnosti materiala PU in s tem na mehanske lastnosti kolesa za točnejše rezultate termomehanske analize.

Predstavljen je predlog metode za konfiguriranje novega kolesa, kakor tudi metoda za analizo termomehanskih lastnosti nepnevmatskih koles. Članek tako podaja teoretične osnove in metodološke smernice za preučevanje utrujenostnih lastnosti koles v pogojih termomehanske sklopitve.

Ključne besede: nepnevmatsko kolo, upogljiva napera, metoda konfiguracije enot, preizkus prototipa, numerična analiza, termomehanska sklopitev, temperaturno polje

---

Raziskava in optimizacija parametrov sistema mazanja z minimalno količino pri glajenju kaljenega jekla

An-Le Van[1] – Trung-Thanh Nguyen[2,*]

[1] Univerza Nguyen Tat Thanh, Tehniška fakulteta, Vietnam
[2] Tehniška univerza Le Quy Don, Fakulteta za strojništvo, Vietnam

Cilj dela je optimizacija parametrov delovanja sistema mazanja z minimalno količino, vključno s premerom pršilne šobe, kotom curka, količino maziva in tlakom stisnjenega zraka za izboljšanje cilindričnosti in okroglosti zglajene luknje. Kot omejitveni dejavnik procesa notranjega glajenja je bila opredeljena površinska hrapavost.

Mazanje z minimalno količino (MQL) je uspešna in učinkovita rešitev za zmanjševanje temperature in trenja pri različnih obdelovalnih operacijah. Izbira optimalnih delovnih parametrov MQL za zmanjšanje geometrijskih odstopanj (cilindričnost in okroglost) in površinske hrapavosti po glajenju pa še ni bila raziskana.

Predlagani so modeli umetnih nevronskih mrež za napovedovanje rezultatov glajenja z optimizacijo vhodov. Vrednost uteži za vsak odgovor je bila izračunana s sivo relacijsko analizo. Optimalne vrednosti parametrov sistema MQL in tehnološki cilji so bili izbrani s pomočjo evolucijskega algoritma z vibracijami in komunikacijo v roju delcev.

Nove znanstvene ugotovitve bodo pomembne pri izbiri optimalnih parametrov delovanja strojev za izboljšanje kakovosti lukenj po procesih glajenja z mazanjem z minimalno količino. Vrednosti cilindričnosti, okroglosti in površinske hrapavosti so se v primerjavi z začetnimi vrednostmi izboljšale za 53,14 %, 57,83 % in 72,97 %.

Vpliv parametrov sistema MQL na rabo energije in proizvodne stroške ni bil predstavljen. Celovita večciljna optimizacija bo predmet prihodnjih raziskav.

Optimizacijska metoda je uporabna tako za operacije glajenja kakor tudi za druge obdelovalne procese. Operaterji strojev bodo lahko s pridobljenim znanjem bolje razumeli fizikalne pojave pri razvitih operacijah glajenja ter izboljšali kakovost obdelave lukenj v različnih komponentah. Optimizacija cilindričnosti in okroglosti s površinsko hrapavostjo kot vnaprej opredeljenim omejitvenim dejavnikom je v primerjavi s simultano optimizacijo treh ciljev bolj realistična in zanesljivejša. Predlagane korelacije bo mogoče učinkovito uporabiti za napovedovanje rezultatov glajenja v industrijskih aplikacijah. S predlaganimi modeli ANN si je mogoče prihraniti veliko stroškov in truda z eksperimentiranjem. 3D-grafikoni, ki prikazujejo globalne odvisnosti pri rezultatih obdelave, lahko pomagajo operaterjem strojev pri izbiri optimalnih vrednosti delovanja MQL, krožnosti in cilindričnosti glede na zahtevano površinsko hrapavost za različne namene.

Ključne besede: notranje glajenje, cilindričnost, krožnost, hrapavost, ANN, VCPSO

*Naslov avtorja za dopisovanje: Tehniška univerza Le Quy Don, Fakulteta za strojništvo, 236 Hoang Quoc Viet, Ha Noi, Vietnam, trungthanhnguyen@lqdtu.edu.vn

Optimizacija faktorjev varjenja raznorodnih zlitin AA6061-t6 and AZ31B za trdoto spojev

Karutha Pandian Vasantha Kumar* – Muthusamy Balasubramanian

Univerza Anna, Univerzitetni tehniški kolidž, Oddelek za strojništvo, Indija

Aluminijeve in magnezijeve zlitine spadajo med neželezne materiale, ki so se dobro uveljavili v sodobnih industrijah, npr. v avtomobilski, letalski in pomorski. Aluminijeva zlitina AA6061 ima visoko razmerje med trdnostjo in maso, se dobro obdeluje in ima odlične protikorozijske lastnosti. Tudi magnezijeva zlitina AZ31B je razširjena v industriji zaradi majhne gostote in visoke trdnosti. Varjenje raznorodnih neželeznih kovin je zelo zahtevno, konvencionalni postopki pa so v tem primeru obremenjeni z različnimi pomanjkljivostmi in težavami. Varjenje z gnetenjem je novejši proces varjenja brez taljenja, ki se danes pogosto uporablja pri spajanju neželeznih materialov. Gre za postopek, pri katerem se rotirajoče neobrabno orodje s čepom vriva v material na stiku dveh obdelovancev. Zaradi trenja med orodjem in obdelovancem nastaja toplota, ki material ogreje in omehča. Orodje se premika vzdolž stika, z vrtenjem mehansko premeša zmehčan material in nastane spoj v trdnem stanju. Pri varjenju raznorodnih neželeznih materialov z gnetenjem se pojavljajo razne komplikacije, povezane z različnimi materialnimi lastnostmi. Odprava teh težav in izboljšanje kakovosti zvarnih spojev aluminijastih in magnezijevih zlitin zahteva optimizacijo procesnih faktorjev, ustrezno konstrukcijo orodja in odmike orodja.

Glavni cilj pričujoče raziskave je doseganje višje trdote spojev aluminijeve zlitine AA6061 in magnezijeve zlitine AZ31B s pravo konstrukcijo orodja, odmiki orodja in optimalnimi faktorji procesa. Varjenje plošč iz Al in Mg zlitin je bilo opravljeno z orodjem iz volframovega karbida z grezilom čepa cilindrične oblike. Rotirajoče orodje je bilo na napredujoči strani vstavljeno z odmikom 1 mm od linije spoja. Glavni faktorji procesa varjenja z gnetenjem so vrtilna hitrost, hitrost podajanja in nagibni kot orodja. Za zasnovo eksperimenta je bila uporabljena metoda odzivnih površin s centralnim sestavljenim načrtom, uporabljene pa so bile tri ravni procesnih faktorjev.

Opravljeni so bili eksperimenti z različnimi kombinacijami faktorjev varjenja z gnetenjem. Preizkušanci so bili pripravljeni po standardih za preiskave trdote po Vickersu. Trdota v območju zvara je bila izmerjena s sistemom za merjenje trdote po Vickersu. Iz rezultatov je bila izračunana regresijska enačba za določitev vpliva posameznih faktorjev na trdoto. Ustreznost regresijske enačbe je bila nato preverjena z analizo ANOVA in preverjanja so potrdila ustreznost modela. Hitrost podajanja in vrtilna hitrost za razliko od nagibnega kota orodja pomembno vplivata na trdoto zvarnih spojev raznorodnih Al/Mg zlitin. Trdota zvarnih spojev se povečuje z naraščanjem vrednosti RS in TTA in je višja pri nižjih hitrostih podajanja. Hitrost podajanja ima večji vpliv na trdoto zvarnega spoja kot vrtilna hitrost in nagibni kot orodja. Optimalni faktorji obdelave za visoko trdoto (92 HV) so bili določeni po načelu zaželenosti: vrtilna hitrost 1000 obr./min, hitrost podajanja 30 mm/min in nagibni kot orodja 2° pri vrednosti zaželenosti 0,98. Potrditveni preizkus je pokazal trdoto zvarnega spoja Al/Mg zlitin v višini 92,5 HV. Ta vrednost predstavlja 85 % vrednosti trdote aluminijeve zlitine in 110 % trdote magnezijeve zlitine. Analizirana je bila tudi mikrostruktura v območju zvarne leče in termomehansko vplivane cone.

Ključne besede: varjenje raznorodnih materialov z gnetenjem, aluminijeva zlitina AA6061, magnezijeva zlitina AZ31B, varjenje z gnetenjem, RMS, ANOVA

*Naslov avtorja za dopisovanje: Univerza Anna, Univerzitetni tehniški kolidž, Oddelek za strojništvo,
Ramanathapuram Campus, Ramanathapuram, Tamilnadu, Indija, kpvasanthkumar@gmail.com

Napovedovanje napak robotov za obdelavo velikih optičnih zrcal na osnovi globokega učenja

Zujin Jin[1] – Gang Cheng[1,2,*] – Shichang Xu[1] – Dunpeng Yuan[1]
[1] Kitajska rudarska in tehniška univerza, Šola za mehatroniko, Kitajska
[2] Shangdong Zhongheng Optoelectronic Technology Co., Kitajska

Sodobni optični sistemi z razvojem informacijske dobe hitro napredujejo v smeri velikih zaslonk, visoke točnosti, visoke ločljivosti in velikih moči. S tem se povečujejo tudi zahteve za robote, ki so namenjeni obdelavi velikih optičnih zrcal (LOMPR). LOMPR za učinkovito in točno obdelavo velikih in asferičnih optičnih zrcal so ključna tehnologija, ki omogoča hiter razvoj sodobne optike in naprednih optičnih sistemov. Obdelava optičnih zrcal vključuje štiri korake: grobo brušenje, oblikovanje z rezkanjem, fino brušenje in poliranje. Roboti LOMPR uporabljajo za vse štiri korake fiksno trajektorijo v obliki mrež, koncentričnih krogov ali spiral. Dinamične lastnosti in parametri regulacije LOMPR na določeni trajektoriji izkazujejo periodične spremembe. Obdelava optičnih zrcal zahteva več iteracij, proces izdelave velikih optičnih zrcal iz surovcev pa lahko traja od nekaj dni do več mesecev. Določanje dolgotrajnih periodičnih gibanj je lahko uporabno za statistično analizo nelinearnih napak ter napovedovanje usmeritve in velikosti napak kot osnovo za pravočasne protiukrepe. Napake trajektorije LOMPR je treba napovedati na osnovi predhodnih parametrov obdelave za kompenzacijo negotovosti modela ter izboljšanje natančnosti površin in učinkovitosti obdelave optičnih zrcal.

Postavljen je bil model za napovedovanje napak končne trajektorije LOMPR na osnovi nevronskih mrež z dolgim kratkoročnim spominom in Bayesovsko optimizacijo (BO-LSTM). Po Bayesovi metodi je bilo optimizirano število paketov, število skritih nevronov in hitrost učenja LSTM. Postavljeni modeli so bili nato uporabljeni za napovedovanje napak spiralne trajektorije LOMPR v smereh X in Y, rezultati napovedi pa so bili primerjani z rezultati nevronske mreže z vzvratnim postopkom učenja (BP).

Rezultati eksperimentov so pokazali, da se je čas učenja BO-LSTM v primerjavi z nevronsko mrežo BP skrajšal za 21,4 % oz. 15,2 % v smereh X in Y. Poleg tega so se vrednosti MSE, RMSE in MAE napake napovedi v smeri X zmanjšale na 9,4 %, 30,5 % oz. 31,8%, v smeri Y pa na 9,6 %, 30,8 % oz. 37,8 %. Potrjeno je, da je model za napovedovanje BO-LSTM izboljšal natančnost napovedi napake končne trajektorije LOMPR in učinkovitost napovedi, ki predstavlja raziskovalno osnovo za izboljševanje točnosti površin optičnih zrcal.

Poudarki v članku so:
1) Postavljen je bil model za napovedovanje napak končne trajektorije na osnovi nevronskih mrež z dolgim kratkoročnim spominom in Bayesovsko optimizacijo.
2) Modeli so bili uporabljeni za napovedovanje napak spiralne trajektorije robota za obdelavo velikih optičnih zrcal.
3) Po Bayesovi metodi je bilo optimizirano število paketov, število skritih nevronov in hitrost učenja LSTM.
4) Rezultati eksperimentov so pokazali, da model za napovedovanje napak končne trajektorije z dolgim kratkoročnim spominom in Bayesovsko optimizacijo ne izboljšuje le točnosti napovedi napake končne trajektorije robotov LOMPR, temveč tudi učinkovitost teh napovedi.

Model za napovedovanje BO-LSTM je izboljšal tako natančnost napovedi napake končne trajektorije LOMPR kakor tudi učinkovitost napovedi, ki bo zanesljiva teoretična osnova in podatkovna podpora za kompenzacijo napak končnih trajektorij z upoštevanjem motenj pri prihodnjih LOMPR. Predlagani model za napovedovanje napak BO-LSTM v pričujočem članku bo lahko uporaben za napovedovanje kinematične napake tudi pri drugih paralelnih in hibridnih robotih.

Ključne besede: Bayesova optimizacija, BO-LSTM, napovedovanje napak, obdelava optičnih zrcal, hibridni manipulator, hiperparametrika

*Naslov avtorja za dopisovanje: Kitajska rudarska in tehniška univerza, Šola za mehatroniko, Nanhu campus, No. 1 University Road, 221116, Xuzhou, Kitajska, chg@cumt.edu.cn

Optimizacija porabe filamenta PLA za 3D-tiskanje po metodi toplotne obdelave v domačem okolju

Milena Djukanović[1, *] – Milanko Damjanović[2] – Luka Radunović[2] – Mihailo Jovanović[3]

[1] Univerza Črne gore, Fakulteta za elektrotehniko, Črna gora
[2] Univerza Črne gore, Fakulteta za strojništvo, Črna gora
[3] Univerza Adriatik, Fakulteta za management, Črna gora

Skupnost uporabnikov 3D-tiska je takoj po začetku pandemije covida-19 ponudila svojo pomoč. Mnoga svetovno znana podjetja so brezplačno dala na razpolago 3D-modele za zaščitne maske, vizirje in druge pripomočke za medicinsko osebje, skupaj s priporočenimi parametri in odprtokodnimi datotekami za tisk. Njihova zamisel je bila, da lahko vsak posameznik pomaga svoji državi z zaščitno opremo za vse, ki jo potrebujejo. Veliko težavo pa je predstavljalo pomanjkanje filamentov za množično 3D-tiskanje. To težavo bi bilo mogoče drastično zmanjšati z optimizacijo porabe materiala pri tisku. Trdnost natisnjenih izdelkov je med drugim mogoče povečati s toplotno obdelavo, ki je predmet tega članka. Z naknadnim ojačenjem je mogoče omejiti porabo materiala z zmanjšanjem odstotka polnitve pri pripravi G kode. Za pričujočo raziskavo je bil izbran filament PLA, ki se najpogosteje uporablja za 3D-tisk. S preizkušanjem rezultatov žarjenja pri različnih temperaturah in časih toplotne obdelave je bil določen optimalen postopek za ojačenje natisnjenih izdelkov iz materiala PLA, kakor tudi rešitev za optimalno zmanjšanje mase zadevnih izdelkov. Z uporabo opisanega pristopa na globalni ravni bi bilo mogoče doseči pomembne rezultate.

Izbrani so bili časi toplotne obdelave 30 minut, 60 minut in 90 minut pri sobni temperaturi (brez toplotne obdelave) ter pri temperaturah 70 °C, 90 °C, 110 °C in 130 °C. Toplotno obdelani preizkušanci lahko v primerjavi z neobdelanimi preizkušanci (5711 N) vzdržijo za 20 % večje povprečne sile. Ko temperatura žarjenja preseže temperaturo steklastega prehoda, postane molekularna struktura dolgih polimernih verig vse bolj organizirana in element je bolj tog. Ko se temperatura dviguje proti tališču, se začne zaradi raztegovanja po vzdolžni osi zmanjševati presek preizkušanca. Ta je obremenjen z večjimi napetostmi in preizkušanec vzdrži nekoliko manjšo silo. Višje temperature toplotne obdelave povzročijo deformacijo materiala pri nateznem preizkusu in raztezek v višini približno 10 %. Temperature nad 130 °C niso bile obravnavane zaradi omenjenega problema. Deformacija materiala je velika težava pri žarjenju 3D-natisnjenih izdelkov z mehanskimi funkcijami, kot so npr. umetniški izdelki. Skrčenje prereza je nekoliko manjše od raztezka – približno 9 % pri omenjeni višji temperaturi toplotne obdelave. Ko preizkušanec doseže temperaturo tališča, se naglo poveča vodoravni raztezek. Opisana metoda za ojačenje filamenta PLA omogoča velik prihranek materiala pri množični proizvodnji nekaterih elementov, težava pa je v tem, da so običajne gospodinjske pečice premajhne za večje število izdelkov. S prevrevanjem izdelkov v vodi namesto s segrevanjem v pečici je mogoče prihraniti veliko časa, saj se mora natisnjeni element segreti samo na določeno temperaturo (do vrelišča vode). Deformacija v preizkušanem območju temperatur in časov toplotne obdelave je manjša od 5 %, kar je sprejemljivo za večino 3D-natisnjenih elementov. S preprosto prilagoditvijo skale elementa pri ustvarjanju G kode se lahko vpliv te deformacije po žarjenju približa vrednosti nič.

Ključne besede: covid-19, 3D-tisk, optimizacija porabe materiala, žarjenje, material PLA, ojačenje PLA

---

*Naslov avtorja za dopisovanje: Univerza Črne gore, Fakulteta za elektrotehniko, 81000 Podgorica, Črna gora, milenadj@ucg.ac.me

Adaptivni elektromagnetni blažilnik vibracij za večmodalne konstrukcije

Khaled S. Mohamed[1] – Fatin Amri[2] – Mostafa Elboraey[1] – N.H. Diyana Nordin[2] – Asan G.A. Muthalif[1,*]

[1] Univerza v Katarju, Tehniški kolidž, Oddelek za strojništvo in industrijski inženiring, Katar
[2] Mednarodna islamska univerza v Maleziji, Oddelek za mehatroniko, Malezija

Vse konstrukcije so izpostavljene vibracijam zaradi zunanjih dinamičnih sil, ki jih med drugim povzročajo potresi in vetrne obremenitve. Če nastopi resonanca, lahko dinamične sile konstrukcijo tudi porušijo, s katastrofalnimi posledicami za varnost ljudi. Rešitev za odpravo te grožnje so blažilniki vibracij, ki omogočajo nadzor nad vibracijami konstrukcij. Za konstrukcije z več prostostnimi stopnjami je značilno, da imajo več lastnih oblik, toda masni blažilniki lahko običajno dušijo samo eno frekvenco. Za nadzor nad vibracijami sistemov z več prostostnimi stopnjami je zato potreben prilagodljiv oz. nastavljiv blažilnik vibracij. Za pasivne in aktivne blažilnike so značilne pomanjkljivosti kot so teža, hitro slabšanje nekaterih parametrov, nelinearne histerezne sile in nizek odstotek zmanjšanja amplitude vibracij. V članku je zato predstavljen predlog nastavljivega masnega blažilnika za različne frekvence vibracij, ki odpravlja nekatere obstoječe težave in zagotavlja največje odstotno zmanjšanje amplitude vibracij.

Predlagani adaptivni elektromagnetni blažilnik vibracij (AEMVA) odpravlja vpliv vibracij in ga je mogoče dinamično uravnavati z elektromagneti. Tok, ki se dovaja tuljavam elektromagnetov, vpliva na magnetne lastnosti blažilnika in s tem na odrivne sile, ki so potrebne za uravnavanje AEMVA. S prilagajanjem togosti se lahko nastavlja lastna frekvenca sistema za usklajevanje frekvenc konstrukcije in blažilnika. Uspešnost AEMVA pri blaženju več lastnih oblik je bila dokazana analitično in eksperimentalno na primerjalnem modelu trinadstropne zgradbe.

Ustvarjen je bil matematični opis AEMVA za prototip trinadstropne zgradbe, ki modelira parametre sistema. Oblikovan je bil tudi teoretični model za primerjavo z rezultati eksperimentov.

Izkazalo se je, da se je amplituda vibracij prve, druge in tretje lastne oblike zmanjšala za 68,81 %, 50,49 % oz. 33,45 %. Rezultati simulacij in eksperimentov dokazujejo, da lahko en sam blažilnik duši vpliv različnih vibracij na večmodalno konstrukcijo.

Med eksperimentalno analizo so bile ugotovljene nekatere omejitve, ki bodo odpravljene v prihodnjih raziskavah. Te so povezane z velikostjo eksperimenta in z lastnimi frekvencami, ki naj bi jih blažilnik absorbiral. Največji uporabljeni tok pri prototipu je znašal 3 A, z napajanjem elektromagnetov z večjimi tokovi pa bi bilo mogoče nadzorovati tudi višje lastne frekvence. Zaradi razpoložljivosti so bila uporabljena elektromagnetna jedra iz ogljikovega jekla, z uporabo materiala z večjo magnetno permeabilnostjo, kot je npr. mehko železo, pa bi bilo mogoče doseči enako jakost magnetnega polja z manjšim električnim tokom. Omejevanje tokov je pomembno zaradi pregrevanja elektromagnetov. Delo se bo nadaljevalo z izpopolnjevanjem predlaganega blažilnika v smeri odprave omejitev in razvoja zasnove pametnega regulatorja za samodejno prilagajanje lastne frekvence blažilnika dani lastni obliki nihanj.

Ključne besede: adaptivni blažilnik vibracij, elektromagnetni blažilnik vibracij, večmodalni sistem, dinamično modeliranje, nadzor nad vibracijami konstrukcij, analiza v frekvenčni domeni, mehanski model vibracij

*Naslov avtorja za dopisovanje: Univerza v Katarju, Tehniški kolidž, Oddelek za strojništvo in industrijski inženiring, Doha, Katar, drasan@qu.edu.qa

Statistično modeliranje in optimizacija parametrov varjenja po postopku TIG z metodo Taguchi

S. Omprakasam[1,*] – K. Marimuthu[2] – R. Raghu[1] – T. Velmurugan[1]

[1] Tehniški kolidž Sri Ramakrishna, Oddelek za strojništvo, Indija
[2] Inštitut za tehnologijo v Coimbatoru, Oddelek za strojništvo, Indija

V predstavljeni študiji je bil po metodi Taguchi preučen vpliv parametrov varjenja zlitine AA5052 po postopku TIG na lastnosti zvara.

Preizkušanci iz aluminijeve zlitine AA5052 so bili varjeni z dodajnim materialom ER5356. Eksperimenti so bili zasnovani z ortogonalnim poljem Taguchi L27 ter spreminjanjem parametrov toka, napetosti in hitrosti in odgovori faktorjem oblike prevaritve (PSF), faktorjem oblike ojačitve (RFF) in trdoto osnovnega materiala. Trend odvisnosti odgovorov od parametrov je predstavljen z grafi glavnih učinkov in odzivnih površin. Za določitev vpliva parametrov je bila uporabljena analiza razmerja med signalom in šumom (S/N), medtem ko so bili prispevki posameznih parametrov ocenjeni z analizo variance (ANOVA). Ustreznost razvitega modela je bila preverjena z regresijsko analizo in eksperimentalno.

Uporabljena je bila tehnika zasnove eksperimentov po metodi Taguchi za določitev vpliva parametrov in njihovih optimalnih vrednosti za proces varjenja.
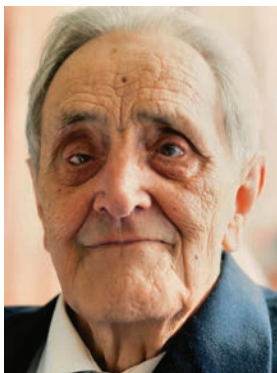
Rezultati:
- Eksperimenti so pokazali, da je bila maksimalna trdota v višini 145,3 HV dosežena pri vrednostih RFF = 4,49 in PFF = 3,83 ter pri toku 140 A, napetosti 18 V in hitrosti 300 mm/min.
- Vrednost RFF se močno poviša, ko se tok poveča s 40 A na 140 A. PSF se zmerno zmanjšuje s porastom napetosti, medtem ko je vpliv hitrosti na zmanjšanje PSF minimalen. Trdota se močno poveča s povišanjem toka in rahlo poveča s povišanjem napetosti, medtem ko povišanje hitrosti ne vpliva pomembno na trdoto. Iz diagramov interakcij je razvidno izboljšanje trdote pri vrednosti toka 140 A in napetosti 18 V.
- Razmerje med signalom in šumom ter analiza variance sta pokazala, da ima tok največji vpliv na vrednosti RFF, PSF in trdote, sledita pa mu napetost in hitrost. Iz regresijske analize sledi, da je razviti model primeren za napovedovanje RFF, PSF in trdote zvarov v odvisnosti od procesnih parametrov.
- V mikrostrukturi niso bile ugotovljene napake, kot so praznine, razpoke ter območja nepopolne spojitve. V talilni coni je razviden razvoj zrn s podaljšanimi celičnimi dendritnimi oblikami in z grobimi delci Mg_2Si v osnovi iz α-aluminija.
- Opravljeni so bili potrditveni preizkusi in iz profila trdote preizkušancev sledi, da je trdota največja v talilni coni, temu pa sledita toplotno vplivana cona in osnovni material.

Prispevek članka:
- Določene so bile optimalne vrednosti toka, napetosti in hitrosti pri varjenju zlitine AA5052 za maksimalno trdoto 145,3 HV.
- Med vsemi obravnavanimi parametri ima tok največji vpliv na vrednosti RFF, PSF in trdote pri varjenju zlitine AA5052.
- Razviti model dobro popisuje odvisnosti parametrov procesa ter vrednosti RFF, PSF in trdote varjencev.
- V talilni coni varjenih preizkušancev AA5052 je bila ugotovljena povišana trdota.

Ključne besede: TIG varjenje, aluminij, AA5052, trdota, RFF, PSF, Taguchi

*Naslov avtorja za dopisovanje: Tehniški kolidž Sri Ramakrishna, Oddelek za strojništvo, Coimbatore-641022, Tamil Nadu, Indija, somprakasam@gmail.com

Prof. dr. Jože Hlebanja
(1926 – 2022)

12. januarja letošnjega leta je hladen zimski veter s seboj ponesel zadnjo sapo klenega moža, ki je s svojim intelektom ter delovnim zanosom soustvarjal in idealom pravičnega napredka utiral pot razvoju družbe ter se nesebično razdajal generacijam študentov in mladim strokovnjakom v gospodarstvu.

Zaslužni prof. dr. Jože Hlebanja se je rodil 31. marca 1926 na Srednjem vrhu pri Kranjski gori. Nižjo srednjo šolo je obiskoval na Jesenicah in se leta 1941 vpisal na srednjo tehniško šolo v Ljubljani. Od leta 1943 je bil aktiven v OF. Januarja 1944 je odšel v partizane, kjer je bil še istega leta ujet in zaprt v zaporu na Begunjah, kasneje pa v koncentracijskem taborišču Mauthausen. Po osvoboditvi iz taborišča se je zaposlil v Železarni Jesenice in leta 1946 maturiral na tehniški srednji šoli. Jeseni leta 1946 se je vpisal na Strojni oddelek Tehniške fakultete v Ljubljani, Univerze v Ljubljani. Že naslednje leto je postal pomožni asistent za mehaniko in trdnost ter leta 1952 diplomiral. Že med študijem je intenzivno sodeloval na Katedri za transportne naprave pri konstruiranju žerjavov. Po diplomi je postal redni asistent na področju Transportne naprave in dvigala. Po treh letih dela na fakulteti se je kot samostojni projektant za žerjave in transportne naprave zaposlil v Metalni Maribor. V tem času je opravil strokovne specializacije v tujini in sicer pri firmah Girak (žičnice) in SGP (konstrukcija dvigal) na Dunaju ter Pohling (projektiranje kompleksnih transportnih naprav) v Kölnu. Leta 1959 se je vrnil na Tehniško fakulteto, kjer je bil izvoljen za docenta. Leta 1967 je zagovarjal doktorsko disertacijo s področja posebnih ozobij s konkavno-konveksnim prilagajanjem zobnih bokov. Leta 1968 je bil izvoljen v naziv izrednega profesorja in leta 1976 v naziv rednega profesorja.

Prof. dr. Jože Hlebanja je predstavljal generacijo povojnih konstrukterjev, ki so ključno pripomogli k industrializaciji takratne države. Kot konstrukter je opravil pionirsko delo na področju žičnic. Bil je projektant največjih žičnic na področju nekdanje Jugoslavije. Razvil je domači tip smučarskih vlečnic v Kranjski gori in na Pohorju. Raziskoval je vklapljanje kabin na vlečne vrvi pri krožnih žičnicah in razvil sistem, ki ga je prevzelo tudi avstrijsko podjetje Girak. Projektiral je več ladjedelniških in pristaniških žerjavov, med drugim tudi markantni 45-tonski žerjav v ladjedelnici 3. maj na Reki.

Največji znanstveni doprinos je prof. dr. Jože Hlebanja dosegel pri razvoju zobnikov s posebno obliko ozobja. Obdelal je možnost uporabe matematično definiranih krivulj za oblikovanje zobnih bokov. Nova oblika zobnih bokov ima izboljšano bočno in korensko trdnost ter boljše tribološke lastnosti v primerjavi s konvencionalnim evolventnim ozobjem. Objavil je približno sedemdeset znanstvenih in strokovnih člankov in je soavtor osmih patentov, od tega sta dva mednarodna.

V bivši državi je bil soustanovitelj Jugoslovanskega društva za strojne elemente in konstruiranje. V študij strojništva na matični fakulteti je uvedel tri nove usmeritve: *konstruiranje*, *tehnološko strojništvo* in *energetsko strojništvo*. V študijski proces je vpeljal predmeta Tribologija in Metodika konstruiranja, ki sta bila popolna novost na področju strojništva v bivši državi. V nadaljevanju pedagoškega dela je uvedel še predmeta Lesarki stroji in Kmetijski stroji. Bil je mentor več kot 100 diplomantom, magistrom in doktorjem znanosti. Napisal je več visokošolskih učbenikov s področja strojnih elementov in metodike konstruiranja.

Na matični fakulteti je vodil Laboratorij za konstrukcijo strojev. Deloval v različnih komisijah, bil je tudi predstojnik Katedre za konstruiranje in delovne stroje, med letoma 1974 in 1976 je bil prodekan Fakultete za strojništvo Univerze v Ljubljani. Bil je član različnih domačih in tujih stanovskih združenj s področja strojništva. Nenazadnje je njegova zapuščina na področju konstruiranja tudi pet laboratorijev Fakultete za strojništvo, ki celovito pokrivajo področja konstruiranja strojev in naprav. Upokojil se je leta 1991 in bil leta 1996 imenovan za zaslužnega profesorja Univerze v Ljubljani. Tudi po upokojitvi ni zanemaril raziskovalnega dela na področju zobnikov s posebno obliko ozobja.

Za svoje delo je bil odlikovan z redom dela z zlatim vencem. Leta 1976 je prejel nagrado sklada Borisa Kidriča, leta 1989 pa zlato plaketo Univerze v Ljubljani. Prejel je tudi avstrijsko državno priznanje (Grosse Ehrenzeichen) za zasluge pri delu v mednarodnem koncentracijskem taboriščnem odboru Mauthausen in zlato plaketo Zveza združenj borcev za vrednote NOB Slovenije.

Prof. dr. Mihael Sekavčnik,
dekan Fakultete za strojništvo Univerze v Ljubljani

Guide for Authors

All manuscripts must be in English. Pages should be numbered sequentially. The manuscript should be composed in accordance with the Article Template given above. The suggested length of contributions is 10 to 20 pages. Longer contributions will only be accepted if authors provide justification in a cover letter. For full instructions see the Information for Authors section on the journal's website: http://en.sv-jme.eu .

SUBMISSION:

Submission to SV-JME is made with the implicit understanding that neither the manuscript nor the essence of its content has been published previously either in whole or in part and that it is not being considered for publication elsewhere. All the listed authors should have agreed on the content and the corresponding (submitting) author is responsible for having ensured that this agreement has been reached. The acceptance of an article is based entirely on its scientific merit, as judged by peer review. Scientific articles comprising simulations only will not be accepted for publication; simulations must be accompanied by experimental results carried out to confirm or deny the accuracy of the simulation. Every manuscript submitted to the SV-JME undergoes a peer-review process.

The authors are kindly invited to submit the paper through our web site: http://ojs.sv-jme.eu. The Author is able to track the submission through the editorial process - as well as participate in the copyediting and proofreading of submissions accepted for publication - by logging in, and using the username and password provided.

SUBMISSION CONTENT:

The typical submission material consists of:
- A **manuscript** (A PDF file, with title, all authors with affiliations, abstract, keywords, highlights, inserted figures and tables and references),
- Supplementary files:
  - a **manuscript** in a WORD file format
  - a **cover letter** (please see instructions for composing the cover letter)
  - a ZIP file containing **figures** in high resolution in one of the graphical formats (please see instructions for preparing the figure files)
  - possible **appendices** (optional), cover materials, video materials, etc.

Incomplete or improperly prepared submissions will be rejected with explanatory comments provided. In this case we will kindly ask the authors to carefully read the Information for Authors and to resubmit their manuscripts taking into consideration our comments.

COVER LETTER INSTRUCTIONS:

Please add a **cover letter** stating the following information about the submitted paper:
1. Paper **title**, list of **authors** and their **affiliations**. **One** corresponding author should be provided.
2. **Type of paper**: original scientific paper (1.01), review scientific paper (1.02) or short scientific paper (1.03).
3. A **declaration** that neither the manuscript nor the essence of its content has been published in whole or in part previously and that it is not being considered for publication elsewhere.
4. State the **value of the paper** or its practical, theoretical and scientific implications. What is new in the paper with respect to the state-of-the-art in the published papers? Do not repeat the content of your abstract for this purpose.
5. We kindly ask you to suggest at least two **reviewers** for your paper and give us their names, their full affiliation and contact information, and their scientific research interest. The suggested reviewers should have at least two relevant references (with an impact factor) to the scientific field concerned; they should not be from the same country as the authors and should have no close connection with the authors.

FORMAT OF THE MANUSCRIPT:

The manuscript should be composed in accordance with the Article Template. The manuscript should be written in the following format:
- A **Title** that adequately describes the content of the manuscript.
- A list of **Authors** and their **affiliations**.
- An **Abstract** that should not exceed 250 words. The Abstract should state the principal objectives and the scope of the investigation, as well as the methodology employed. It should summarize the results and state the principal conclusions.
- 4 to 6 significant **key words** should follow the abstract to aid indexing.
- 4 to 6 **highlights;** a short collection of bullet points that convey the core findings and provide readers with a quick textual overview of the article. These four to six bullet points should describe the essence of the research (e.g. results or conclusions) and high-light what is distinctive about it.
- An **Introduction** that should provide a review of recent literature and sufficient back-ground information to allow the results of the article to be understood and evaluated.
- A **Methods** section detailing the theoretical or experimental methods used.
- An **Experimental section** that should provide details of the experimental set-up and the methods used to obtain the results.
- A **Results** section that should clearly and concisely present the data, using figures and tables where appropriate.
- A **Discussion** section that should describe the relationships and generalizations shown by the results and discuss the significance of the results, making comparisons with pre-viously published work. (It may be appropriate to combine the Results and Discussion sections into a single section to improve clarity.)
- A **Conclusions** section that should present one or more conclusions drawn from the results and subsequent discussion and should not duplicate the Abstract.
- **Acknowledgement** (optional) of collaboration or preparation assistance may be includ-ed. Please note the source of funding for the research.
- **Nomenclature** (optional). Papers with many symbols should have a nomenclature that defines all symbols with units, inserted above the references. If one is used, it must con-tain all the symbols used in the manuscript and the definitions should not be repeated in the text. In all cases, identify the symbols used if they are not widely recognized in the profession. Define acronyms in the text, not in the nomenclature.
- **References** must be cited consecutively in the text using square brackets [1] and col-lected together in a reference list at the end of the manuscript.
- **Appendix(-icies)** if any.

SPECIAL NOTES

Units: The SI system of units for nomenclature, symbols and abbreviations should be followed closely. Symbols for physical quantities in the text should be written in italics (e.g.

v, T, n, etc.). Symbols for units that consist of letters should be in plain text (e.g. ms^{-1}, K, min, mm, etc.). Please also see: http://physics.nist.gov/cuu/pdf/sp811.pdf .

Abbreviations should be spelt out in full on first appearance followed by the abbreviation in parentheses, e.g. variable time geometry (VTG). The meaning of symbols and units belonging to symbols should be explained in each case or cited in a **nomenclature** section at the end of the manuscript before the References.

Figures (figures, graphs, illustrations digital images, photographs) must be cited in consecutive numerical order in the text and referred to in both the text and the captions as Fig. 1, Fig. 2, etc. Figures should be prepared without borders and on white grounding and should be sent separately in their original formats. If a figure is composed of several parts, please mark each part with a), b), c), etc. and provide an explanation for each part in Figure caption. The caption should be self-explanatory. Letters and numbers should be readable (Arial or Times New Roman, min 6 pt with equal sizes and fonts in all figures). Graphics (submitted as supplementary files) may be exported in resolution good enough for printing (min. 300 dpi) in any common format, e.g. TIFF, BMP or JPG, PDF and should be named Fig1.jpg, Fig2.tif, etc. However, graphs and line drawings should be prepared as vector images, e.g. CDR, AI. Multi-curve graphs should have individual curves marked with a symbol or otherwise provide distinguishing differences using, for example, different thicknesses or dashing.

Tables should carry separate titles and must be numbered in consecutive numerical order in the text and referred to in both the text and the captions as Table 1, Table 2, etc. In addition to the physical quantities, such as t (in italics), the units [s] (normal text) should be added in square brackets. Tables should not duplicate data found elsewhere in the manuscript. Tables should be prepared using a table editor and not inserted as a graphic.

REFERENCES:

A reference list must be included using the following information as a guide. Only cited text references are to be included. Each reference is to be referred to in the text by a number enclosed in a square bracket (i.e. [3] or [2] to [4] for more references; do not combine more than 3 references, explain each). No reference to the author is necessary.

References must be numbered and ordered according to where they are first mentioned in the paper, not alphabetically. All references must be complete and accurate. Please add DOI code when available. Examples follow.

Journal Papers:
Surname 1, Initials, Surname 2, Initials (year). Title. *Journal*, volume, number, pages, DOI code.
[1] Hackenschmidt, R., Alber-Laukant, B., Rieg, F. (2010). Simulating nonlinear materials under centrifugal forces by using intelligent cross-linked simulations. *Strojniški vest-nik - Journal of Mechanical Engineering,* vol. 57, no. 7-8, p. 531-538, DOI:10.5545/sv-jme.2011.013.
Journal titles should not be abbreviated. Note that journal title is set in italics.

Books:
Surname 1, Initials, Surname 2, Initials (year). Title. Publisher, place of publication.
[2] Groover, M.P. (2007). *Fundamentals of Modern Manufacturing*. John Wiley & Sons, Hoboken.
Note that the title of the book is italicized.

Chapters in Books:
Surname 1, Initials, Surname 2, Initials (year). Chapter title. Editor(s) of book, book title. Publisher, place of publication, pages.
[3] Carbone, G., Ceccarelli, M. (2005). Legged robotic systems. Kordić, V., Lazinica, A., Merdan, M. (Eds.), Cutting Edge Robotics. Pro literatur Verlag, Mammendorf, p. 553-576.

Proceedings Papers:
Surname 1, Initials, Surname 2, Initials (year). Paper title. Proceedings title, pages.
[4] Štefanić, N., Martinčević-Mikić, S., Tošanović, N. (2009). Applied lean system in process industry. *MOTSP Conference Proceedings*, p. 422-427.

Standards:
Standard-Code (year). Title. Organisation. Place.
[5] ISO/DIS 16000-6.2:2002. *Indoor Air – Part 6: Determination of Volatile Organic Com-pounds in Indoor and Chamber Air by Active Sampling on TENAX TA Sorbent, Thermal Desorption and Gas Chromatography using MSD/FID*. International Organization for Standardization. Geneva.

WWW pages:
Surname, Initials or Company name. Title, from http://address, date of access.
[6] Rockwell Automation. Arena, from *http://www.arenasimulation.com,* accessed on 2009-09-07.

EXTENDED ABSTRACT:

When the paper is accepted for publishing, the authors will be requested to send an **extended abstract** (approx. one A4 page or 3500 to 4000 characters or approx. 600 words). The instruction for composing the extended abstract are published on-line: http://www.sv-jme.eu/information-for-authors/ .

COPYRIGHT:

Authors submitting a manuscript do so on the understanding that the work has not been published before, is not being considered for publication elsewhere and has been read and approved by all authors. The submission of the manuscript by the authors means that the authors automatically agree to publish the paper uder CC-BY 4.0 Int. or CC-BY-NC 4.0 Int. when the manuscript is accepted for publication. All accepted manuscripts must be accompanied by a Copyright Agreement, which should be sent to the editor. The work should be original work by the authors and not be published elsewhere in any language without the written consent of the publisher. The proof will be sent to the author showing the final layout of the article. Proof correction must be minimal and executed quickly. Thus it is essential that manuscripts are accurate when submitted. Authors can track the status of their accepted articles on https://en.sv-jme.eu/.

PUBLICATION FEE:

Authors will be asked to pay a publication fee for each article prior to the article appearing in the journal. However, this fee only needs to be paid after the article has been accepted for publishing. The fee is 380 EUR (for articles with maximum of 6 pages), 470 EUR (for articles with maximum of 10 pages), plus 50 EUR for each additional page. The additional cost for a color page is 90.00 EUR (only for a journal hard copy; optional upon author's request). These fees do not include tax.

Contents

Papers